DISSERTATION

ANALYSIS OF FLEXURAL EVOLUTION OF THE LITHOSPHERE OVER THE PAST 4.6 MA AROUND ROSS ISLAND, WEST ANTARCTICA

Submitted by

Sumant Jha

Department of Geosciences

In partial fulfillment of the requirements

For the Degree of Doctor of Philosophy

Colorado State University

Fort Collins, Colorado

Fall 2019

Doctoral Committee:

Advisor: Dennis L. Harry

Derek L. Schutt
Richard C. Aster
Gregory C. Amberg

Copyright by Sumant Jha 2019

All Rights Reserved

ABSTRACT

ANALYSIS OF FLEXURAL EVOLUTION OF THE LITHOSPHERE OVER THE PAST 4.6 MA AROUND ROSS ISLAND, WEST ANTARCTICA

Ross Island is in the southern Victoria Land Basin along the western margin of the West Antarctic Rift System. Episodic volcanism since ca. 4.6 Ma produced a discontinuous sedimentary moat around the island coeval with ongoing extension. The moat is a composite of four smaller flexural sub-basins created during four distinct phases of volcanism on Ross Island. In this research we determine the flexural rigidity of lithosphere under Ross Island, to understand the load partitioning between surface (relief) and subsurface (e.g. the density anomaly in crust/mantle) and to test the hypothesis that the strength of the lithosphere around the island varied with time over last 4.6 Ma.

An interactive toolbox called Toolbox for Analysis of Flexural Isostasy (TAFI) was developed in MATLAB to model the flexure around Ross Island. TAFI supports two-dimensional (2-D) and three-dimensional (3-D) modeling of flexural subsidence and uplift of the lithosphere in response to vertical tectonic loading. Flexural deformation is approximated as bending of a thin elastic plate overlying an inviscid fluid asthenosphere. The associated gravity anomaly is calculated by summing the anomalies produced by flexure of each density interface within the lithosphere, using Parker's algorithm. TAFI includes MATLAB functions provided as m-files (also called script files) to calculate the Green's functions for flexure of an elastic plate subjected to point or line loads, and functions to calculate the analytical solution for harmonic loads. Numerical solutions for flexure due to non-impulsive two-dimensional (2-D) or three-dimensional

(3-D) loads are computed by convolving the appropriate Green's function with a spatially discretized load function read from a user-supplied file. TAFI uses MATLAB's intrinsic functions for all computations and does not require any other specialized toolbox, functions, or libraries except those distributed with TAFI. The modeling functions within TAFI can be called from the MATLAB command line, from within user-written programs, or from a graphical user interface (GUI) provided with TAFI. The GUI facilitates interactive flexural modeling and easy comparison of the model to gravity observations and to data constraining flexural subsidence and uplift.

Flexural subsidence within each of the four flexural sub-basins around Ross Island is modeled by using a continuous elastic plate in TAFI. Models of subsidence are constrained by thickness of strata that accumulated in each sub-basin during the time interval in which the associated volcanic center was active. Flexure models were created along profiles trending radially away from volcanic centers. The load due to each volcanic center is represented as a point load at the location of volcano. These models yield best-fit flexural rigidities ranging from 6-36 x 10^{18} N-m, with the lowest values on the south and southwest sides of the island and associated with the youngest volcanoes. This systematic variation in flexural rigidity may be attributed to progressive weakening of the plate with time, or to spatial variations in plate strength. A second group of models constrained by the thickness of the entire stratigraphic interval filling the moat since volcanism began on Ross Island yield a flexural rigidity up to twenty times greater than models that consider only strata deposited within each sub-basin when the associated volcano was active. The second group of models overestimates the strength of the lithosphere due to the inclusion of strata deposited during periods in which regional extension rather than local flexure was the dominant control on subsidence in each sub-basin. In addition to plate flexure, the models indicate a small buoyant load with a magnitude of 7-10 x 10^{16} N beneath Ross Island, equivalent to a

volume of 1.4 – 6.9 x 10^{13} m^3 assuming a density contrast range of 3010 – 3160 kg/m^3, is needed to maintain isostatic equilibrium with a moderately low-density upper mantle.

3-D flexural models are constructed to determine whether variations in the shape of the flexural moat around Ross Island are a result of variations in the strength of the lithosphere with space or with time. These models were constrained by the width and depth of flexure sub-basins around associated loading centers derived from the thickness of entire stratigraphic interval filling the moat since volcanism began on Ross Island. The models with constant flexural rigidity through time are unable to fit the width and depth of flexural subsidence in all parts of flexural moats around Ross Island. Models with time-varying flexural rigidities resulted in an improved fit for different parts of the moat with flexural rigidities varying between 3.0 x 10^{19} N-m to 2.6 x 10^{19} N-m, which is not a resolvable difference.

ACKNOWLEDGMENTS

I am pleased to acknowledge the help and support I received from numerous people during my doctoral studies at Colorado State University (CSU). First, I would like to thank my advisor Dr. Dennis L. Harry for his enthusiasm and support during my research at CSU. He helped me learn topics ranging from geodynamics to life. I cannot thank him enough for being my advisor, my mentor and at times someone who I can talk to about anything that was on my mind.

I would also like to thank my committee members, Dr. Aster and Dr. Schutt for their teachings and advice during my graduate student life at CSU. I am thankful to Dr. Amberg for agreeing be a member of my Ph.D. committee and helping me see the importance of explaining a research in simple words.

I benefited a lot from having discussions with Chris Wenman, Derek Witt, and Jace Kroger during my doctoral studies. Sharon, Patti, and Jill at the Department of Geoscience office were always helpful and informative in any procedural question and helping me navigate the paper works. They went out of their way to make my life easier at CSU. Carl Davis, Robin McGee, Randy Major and others at the Warner College of Natural Resources also helped me a lot to navigate business office and IT issues. Thank you so much for your help!

Finally, how can I forget the Resource for Disabled Students (RDS) department at the Colorado State University. The RDS and Dede Kliewer helped me navigate the program and advocated for me whenever needed. If not for them, I will not be defending this Ph.D. They are a champion for disabled students at Colorado State University.

DEDICATION

~ To my parents and my friends ~

TABLE OF CONTENTS

CHAPTER 1
General background of Ross Island geologic and tectonic settings and flexure theory

1.1 Introduction

Ross Island is a large volcanic complex in west Antarctica, which is dominated by the active Mt. Erebus volcano. The island is located near the seaward edge of the Ross Ice Shelf. Mt. Erebus is surrounded by Mt. Terror on its east, Mt. Bird on its north and Hut Point Peninsula (HPP) eruptive centers to its south. These four volcanoes collectively form Ross Island and have been erupting since ca. 4.6 million years (Kyle, 1990), creating a combined vertical load on the lithosphere to the order of 10^{17} N (Stern et al., 1991; Chapter 3). This loading of the lithosphere resulted in the formation of a ~1.8 km deep flexural moat around the island (Stern et al., 1991) that is evident in stratal relationships imaged in regional seismic reflection data.

Seismic reflection data and cores obtained from seismic surveys and drilling around Ross Island in the Victoria Land Basin (VLB), in Ross Sea and on the northern Ross Ice Shelf show that the middle Miocene and younger sedimentary strata in the region surrounding the moat are comprised of volcaniclastic, glaciomarine and marine sediments and sedimentary rocks (Krissek et al., 2007; Naish et al., 2007; Wilson et al., 2007). Sedimentary units visible on seismic reflection data show several distinct episodes of flexural subsidence within the moat that have been correlated to eruptive events on Ross Island (Horgan et al., 2005; Fielding et al, 2008; Wenman et al., in review).

In this dissertation, I focus on understanding the flexural evolution of the lithosphere around Ross Island and present several two-dimensional (2-D) and three-dimensional (3-D) models of subsidence that are associated with volcanic episodes on the island. These models are used to determine the flexural rigidity of lithosphere under Ross Island, to understand the load

partitioning between the surface (relief) and subsurface (e.g. density anomaly in crust/mantle) and test the hypothesis that the strength of the lithosphere around the island varied with time over last 4.6 Ma.

Chapters 2-4 of this dissertation are written as standalone documents describing a) the MATLAB program TAFI (Toolbox for Analysis of Flexural Isostasy; Jha et al., 2017), that was developed and used in this research to conduct the flexural modeling (Chapter 2); b) 2-D flexural models that focus on constraining the strength of the lithosphere in the region and how the vertical load on the lithosphere is partitioned between surface relief and buried density anomalies (Chapter 3); and c) three-dimensional flexural models designed to distinguish between spatial and temporal variations in the strength of the lithosphere (Chapter 4). This chapter presents the general geological setting of the study area and the theory behind the flexural bending of the lithosphere.

1.2 Geologic and tectonic setting of the Ross Island region

Ross Island is located in the Ross Sea near the southern end of the West Antarctic rift system (WARS). The WARS is a low-lying region underlying most of the Pacific West Antarctic tectonic and geomorphic domain (Behrendt, 1999). This rift is bound by the Transantarctic Mountains and Marie Byrd Land on its western and eastern sides, respectively (Figure 1.1). The WARS includes the Ross Sea which is a 1200 km wide embayment where N-S striking sedimentary basins and basement highs provide a record of extension and crustal thinning during the Late Cretaceous and Paleogene periods (Behrendt, 1999; Behrendt et al., 1991; Cooper et al., 1987; Cooper et al., 1991; Davey & Brancolini, 1995; Decesari et al., 2007; Hinz & Block, 1983; Siddoway, 2007). Rifting began in the Late Cretaceous Period and became progressively more focused toward the flanks of the rift during the Paleogene Period (Hinz & Block, 1983;

Cooper et al., 1991; Davey & Brancolini, 1995; Siddoway et al., 2004; Decesari et al., 2007; Siddoway, 2007; Wilson & Luyendyk, 2009). Extension stopped within the central Ross Sea by late Oligocene and became focused on the VLB region on the western flank of the rift (Figure 1.1), and in the Bentley Subglacial Trough adjacent to Marie Byrd Land on the eastern flank (Chaput et al., 2014; Lloyd et al., 2015). Extension in the VLB has continued, possibly intermittently, since Oligocene time at least into the Quaternary Period (Cooper and Davey, 1985; Davey et al., 2006; Fielding, 2018; Fielding et al., 2008; Paulsen et al., 2014).

Extension on the western flank of the rift was accompanied by emplacement of the Cenozoic McMurdo Volcanic Group (Armstrong, 1978; Kyle, 1990; Kyle & Cole, 1974). The McMurdo Volcanic Group consist of igneous rocks extending discontinuously from Cape Adare at the north end of Victoria Land to Mt. Discovery to the south of Ross Island (Figure 1.1). The McMurdo Volcanic group is subdivided into the Hallett, Melbourne and Erebus Volcanic Provinces based on geographic location (Kyle, 1990; Kyle & Cole, 1974). The Hallett province includes volcanic piles along the north-eastern coast of northern Victoria Land. Melbourne Volcanic Province comprises of volcanoes between Mt. Melbourne to The Pleiades. The Erebus Volcanic Province consists of Mt. Erebus, Mt. Terror, Mt. Bird, and HPP eruptive center which constitute the Ross Island. The volcanic province also includes Mt. Discovery, Mt. Morning, Black Island, White Island, Minna Bluff and Brown Peninsula to the south of Ross Island (Wright and Kyle, 1990a, b; DiRoberto et al., 2010) (Figure 1 . 2). The composition and morphology of these volcanoes include large basaltic shields, large composite central volcanoes of basanitic to phonolitic composition and smaller volcanoes comprised of coalesced basaltic and silicic cones (Kyle, 1981; Aitken et al., 2012). The cause of magmatism in western Antarctica in general and Ross Island is subject to debate. Various models that have been proposed include the presence of

magmatic plumes or fossil plumes beneath Ross Island (Behrendt et al., 1991; Storey et al., 1999; Rocholl et al., 1995), melting of asthenosphere having near normal temperature and composition due to decompression beneath the WARS (Rocchi et al., 2002), and decompression melting of compositionally abnormal asthenosphere that was subject to subduction-related fluid metasomatism in the Mesozoic (Finn et al., 2005).

1.3 Regional drilling programs, seismic surveys and stratigraphic mapping

1.3.1 Drilling programs

In the past few decades, there have been several drilling projects for evaluating the tectonic history of the Ross Sea and the glacial history of the Antarctic Ice sheet. These drilling programs focused on recovering paleoclimatic data from the early Cenozoic Era and Cretaceous Period (Cape Roberts Project - CRP) (Webb and Wilson, 1995), Cenozoic Era (CIROS project) (Barrett, 1982) and middle and late Cenozoic Era (Antarctic Drilling Project - ANDRILL) (Harwood et al., 2002). These data in conjunction with the seismic reflection and refraction data in this region constrain the sedimentary basin evolution in the Ross Sea.

The Cape Roberts Project (CRP) was a multinational project between the Antarctic programs of Australia, Germany, Italy, New Zealand, UK, and the USA. The aim of the CRP project was to obtain continuous core through 1300 m of strata from 30 Ma in age back to as much as 100 Ma in age beneath the western McMurdo Sound, Antarctica. Three drill holes CRP-1, CRP-2 and CRP-3 were drilled during this project, in order to study the tectonic and climatic history of the region (Webb and Wilson, 1995).

The Cenozoic Investigations of the western Ross Sea (CIROS) project was conducted in the western McMurdo Sound in the Ross Sea to investigate the Cenozoic glacial and tectonic history of the region. The strata beneath the floor of McMurdo Sound was cored to record the

major glacial advances and retreats and to find out when they began. Two cores were obtained, CIROS-1 and CIROS-2. The CIROS-1 drill hole penetrated 702.14 m below the seafloor and CIROS-2 penetrated through 166.47 m of sediments into basement gneiss. The cores from these drill holes show alternating sequences of volcanic sediments, diamictites, diatomites and mudstones extending back to Late Eocene age (Brancolini et al., 1995; Barrett, 1982).

In the last decade, a multinational coring initiative called the Antarctic Drilling Project (ANDRILL) was formed with objectives of recovering stratigraphic core records for interpreting Antarctica's Cenozoic climate. This project aimed to resolve the glacial and tectonic history over the past 50 million years and to understand the history of ice volume variation and associated physical changes in the region (Harwood et al., 2002). The first two ANDRILL projects, the McMurdo Ice Shelf (MIS) and the southern McMurdo Sound (SMS) sites, were drilled during the 2006-07 and 2007-08 Antarctic field seasons down to depths of 1285 m and 1138.54 m respectively. The samples recovered by the MIS Project are from ~13 Ma to the present. The samples recovered by the SMS Project are from ~20 Ma to the present.

1.3.2 Seismic surveys

Several seismic reflection surveys have been carried out in the McMurdo Sound and the Ross Sea regions since the 1980s, which were aimed at resolving the tectonic and stratigraphic history of these regions, and in some cases providing two-dimensional subsurface imagery to support stratigraphic drilling projects (Fielding et al., 2008). Seismic surveys around Ross Island correlated with the borehole data have led to the identification of volcaniclastic members within sedimentary strata around Ross Island (Fielding et al., 2008). Periods of flexural infilling are represented by distinctive unconformity bounded wedge-shaped stratigraphic sequences. The geometrical shape and thickness of the cumulative sequences have been modeled as a flexural

response to loads located on or beneath Ross Island (Horgan et al., 2005). This suggests that smaller scale stratigraphic units identified on seismic sections within the flexural moat cumulative sequence can be linked to specific volcanic loading events on Ross Island (Wilson et al., 2003).

1.3.3 Stratigraphic mapping

Several basin-wide unconformities have been identified on seismic reflection and refraction data in the VLB by Fielding and co-workers (Fielding et al., 2008; Fielding, 2018). The corresponding seismic reflectors for these unconformities have been named R_a through R_k, from deepest to shallowest. Strata between R_a to R_e unconformity represent Oligocene early and main rift phases in the region. The main rift phase was followed by a late Oligocene through middle Miocene passive thermal subsidence phase (between unconformities R_e and R_g). Strata overlying R_g represents a middle Miocene and younger Terror Rift phase of subsidence. Wenman et al. (in review) identified three local unconformities in the Ross Island flexural moat (named RMU1, RMU2, and RMU3) along with R_g to R_k regional unconformities identified initially by Fielding and co-workers. Based on the correlation of these regional unconformities to boreholes, Wenman et al identified four periods of flexural subsidence associated with volcanic loading on Ross Island. The stratigraphic interval lying between R_i to RMU1 and RMU1 to RMU2 contain strata deposited during flexural subsidence associated with volcanism on Mt. Bird between ~ 4.6 to 3.0 Ma and 3.0 to ~2.5 Ma, respectively. The interval between horizons RMU2 and R_k correspond to a period when subsidence was dominated by flexure due to volcanism at Mt. Terror (2.5 to ~ 1.8 Ma). Subsidence between R_k and RMU3 horizons was dominated by volcanism at HPP and incipient volcanism at Mt. Erebus between ~1.8 to 0.5 Ma. The final stratigraphic interval, from horizon RMU3 to the seafloor, is dominated by flexural subsidence on the west side of Ross Island due to Mt. Erebus volcanism. Isopach maps generated by Wenman et al. (in review) based on the

correlation of strata to flexural subsidence due to volcanism on Ross Island are used in this research to analyze the formation of Ross Island flexural moat.

1.4 Modelling theory

Almost all rocks at relatively low temperature and pressures behave elastically when the applied stress is not large enough to cause plastic deformation. There are several such examples of lithosphere flexing under surface loads, e.g. the Hawaiian Islands (Walcott, 1970; Watts and Cochran, 1974) and the Canary Islands (Collier and Watts, 2001).

The differential equation relating the vertical flexure of an elastic plate overlying an inviscid substratum is

$$D\nabla^4 w(x,y) + \Delta\rho g w(x,y) = q_a(x,y) \tag{1.1}$$

$$D\left(\frac{d^2}{dr^2} + \frac{1}{r^2}\frac{d}{dr}\right)^2 w(r) + \Delta\rho g w(r) = q_a(\mathrm{r}) \tag{1.2}$$

where, w is the vertical deflection of the plate, ∇^4 is the fourth derivative gradient operator, q_a is the vertical load applied to the plate, $\Delta\rho$ is the density contrast between the mantle underlying the plate and the material filling the basin, x, y and $\boldsymbol{r}$ are cartesian and radial coordinate positions (respectively), g is gravitational acceleration, and D is the flexural rigidity of the lithosphere (Hertz, 1884; Nadai, 1964).

Two commonly used boundary conditions for Equation 1.1 and flexural responses to loading are shown in Figure 1.3. The flexural response for an unbroken (continuous) plate under a 2D line load can be estimated using the following equation (boundary conditions $w(\infty)=0$, $w'(0)=0$):

$$w = \frac{Q_0\alpha^3}{8D} e^{-x/\alpha}\left(cos\frac{x}{\alpha} + sin\frac{x}{\alpha}\right) \tag{1.3}$$

where, Q_0 = load magnitude and α = flexural parameter. α can be related to D as

$$\alpha = \left[\frac{4D}{(\rho_m - \rho_{infill})g}\right]^{1/4} \quad (1.4)$$

Flexural rigidity (D), which is the resistance offered by the plate while undergoing flexure, can be related to the elastic thickness of the plate (T_e) by:

$$D = \frac{ET_e^3}{12(1-v^2)} \quad (1.5)$$

where E is Young's modulus and v is Poisson's ratio.

Equation 1.3 is suitable for plates that are continuous (Figure 1.3a). In volcanic and subduction zones, like Aleutian and Chile trenches, a better boundary condition is for a fractured or broken plate (Figure 1.3b), with the edge of the plate located at the point of loading (Caldwell et al., 1976; Levitt and Sandwell, 1995; Watts, 2001; Bry and White, 2007; Conteras-Reyes and Osses, 2010). In such a case, the boundary condition is zero external torque at the point of loading, which yields boundary conditions $w(\infty) = 0$, $w''(0) = 0$:

$$w = \frac{Q_0\alpha^3}{8D} e^{-x/\alpha}\left(\frac{\cos x}{\alpha}\right) \quad (1.6)$$

In case of an infinite plate with a point load, for e.g., isolated seamounts and near-circular sedimentary basins or a hot spot (Brotchie and Silvester, 1969; Turcotte, 1979), the flexural deflection (w) can be given as:

$$w(r) = \frac{Q_0\alpha^2}{2\pi D} kei\frac{r}{\alpha} \quad (1.7)$$

where, *kei* is zeroth order kelvin function.

To model the flexural subsidence of lithosphere around Ross Island a new MATLAB based toolbox called Toolbox for Analysis of Flexural Isostasy – TAFI (Chapter 2; Jha et al., 2017) was developed. Subsequently, flexural subsidence around Ross Island was modeled using TAFI with infinite plate loaded with superimposed point loads representing the volcanic loads on and around Ross Island (Chapter 3 and 4). A series of point load models for flexural subsidence to the north

of Mt. Bird and Mt. Terror, south of HPP and west of Mt. Erebus is presented in Chapter 3. I discuss the implications of these models vis-à-vis the development of flexural moat around Ross Island over last 4. 6 Ma and distribution of load between the surface and sub-surface in this chapter. In chapter 4, I present a 3-D flexure model which analyzes the variation of flexural strength of the lithosphere over last 4.6 Ma around Ross Island.

1.5 Figures in chapter 1

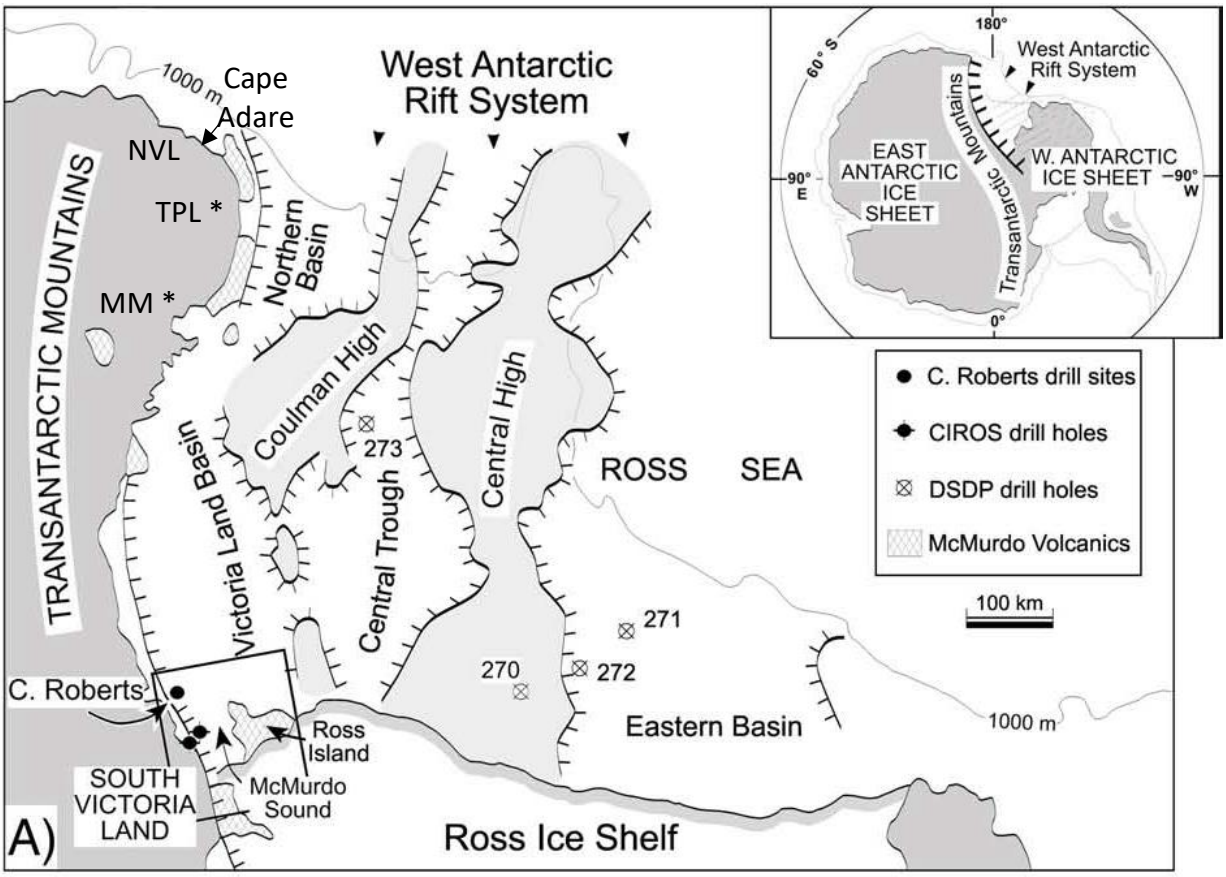

Figure 1.1. Map of Ross Sea region of WARS delineating major basins and geology of adjacent East Antarctica and the Transantarctic Mountains. Inset shows the Antarctic location map and the West Antarctic Rift System (Henrys et al., 2007, Fielding et al., 2008). NVL – Northern Victoria Land, TPL – The Pleiades, MM – Mt. Melbourne.

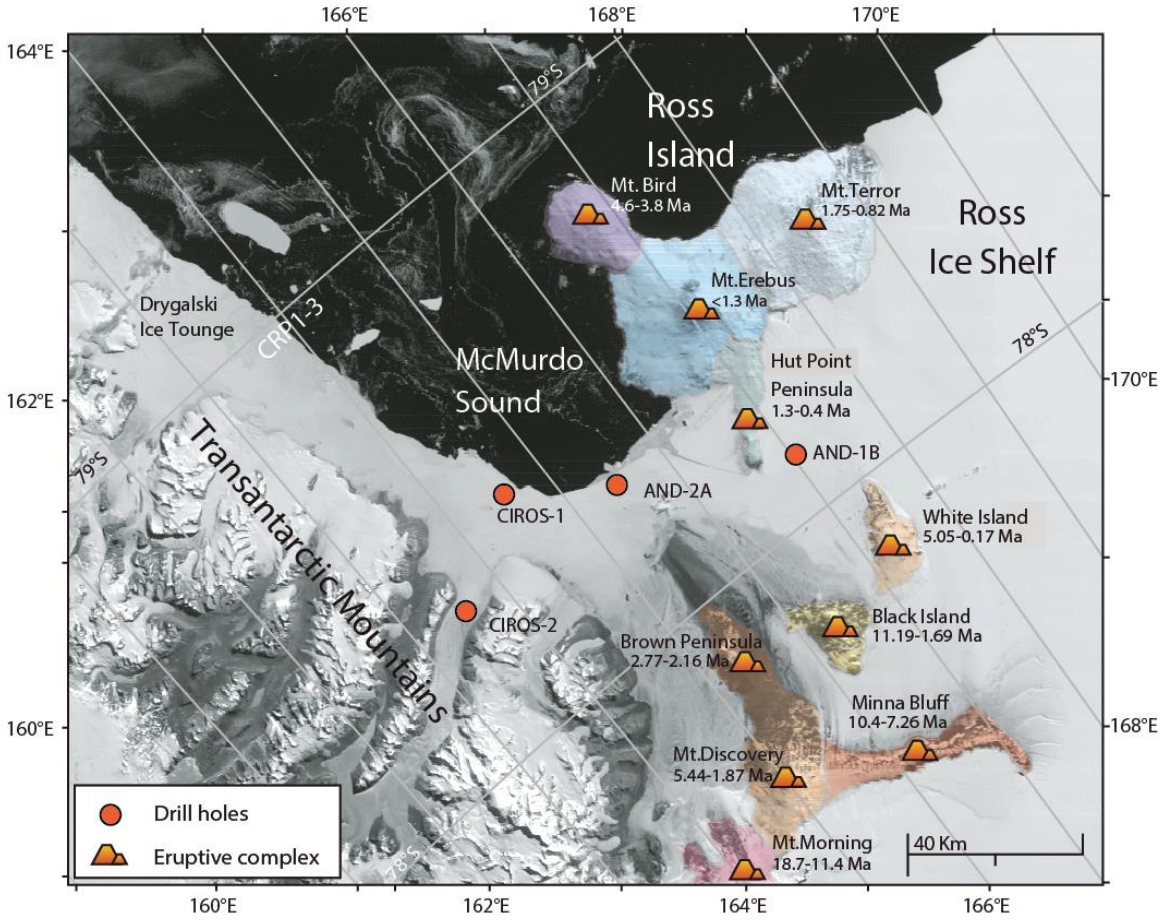

Figure 1.2. Location of main geographical features and drill holes of Erebus Volcanic Province. The Erebus volcanic province (shaded areas) includes Mt. Bird, Mt. Terror, Mt. Erebus, HPP, White Island, Black Island, Minna Bluff, Mt. Discovery, Mt. Morning and Brown Peninsula. The map shows volcanic centers with their corresponding time span of activity and drill holes from ANDRILL and CIROS project around Ross Island (modified from Di Roberto et al., 2010).

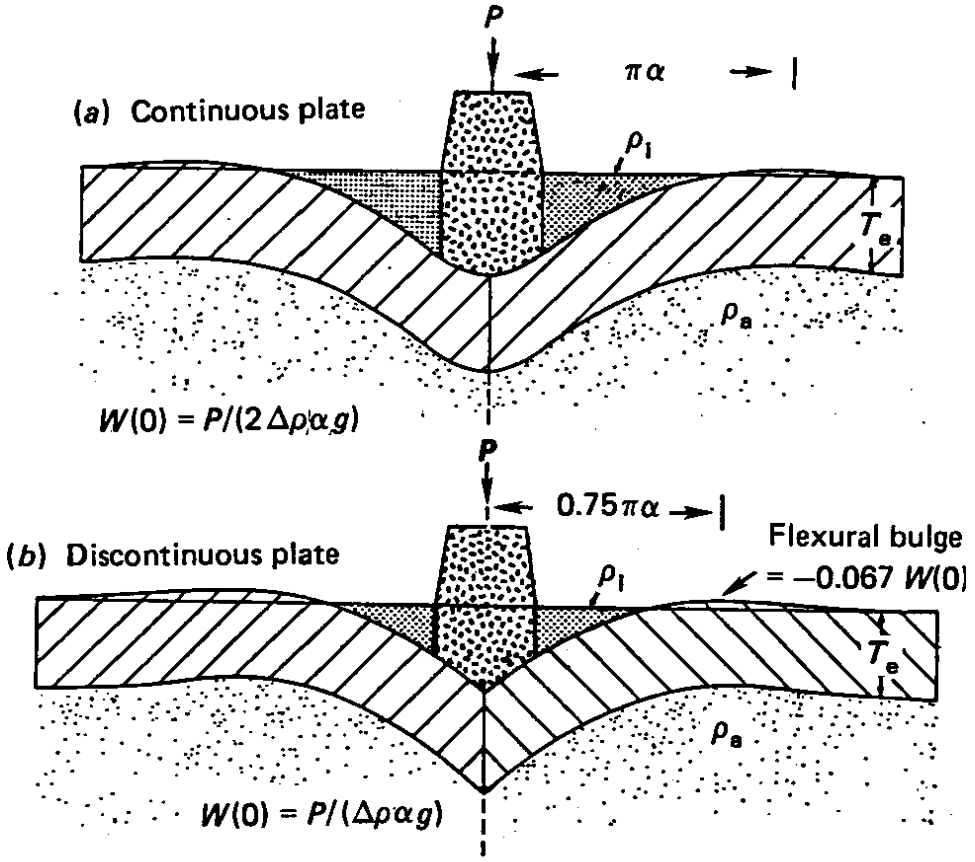

Figure 1.3. Schematic model for flexure of a) continuous elastic plate and b) discontinuous (broken) elastic plate under a 2-D volcanic load. ρ_a and ρ_i represent the densities of asthenosphere and infilling material on top of the plate. α is the flexural parameter (source: Stern et al., 1991).

REFERENCES IN CHAPTER 1

Aitken, A.R.A., Wilson, G.S., Jordan, T., Tinto, K., & Blakemore, H., (2012). Flexural controls on late Neogene basin evolution in southern McMurdo Sound, Antarctica. *Global and Planetary Change, 80*, 99.

Armstrong, R.L. (1978). K-Ar dating: Late Cenozoic McMurdo Volcanic Group and dry valley glacial history, Victoria Land, Antarctica. *New Zealand Journal of Geology and Geophysics, 21(6),* 685-698.

Barrett, P.J., (1982). Proposal for Cenozoic investigations in the western Ross Sea (CIROS). *New Zealand Antarctic Research, 2*, 32-39.

Behrendt, J.C., Duerbaum, H.J., Damaske, D., Saltus, R.W., Bosum, W., & Cooper, A.K., (1991). Extensive volcanism and related tectonism beneath the western Ross Sea continental shelf, Antarctica, Interpretation of an aeromagnetic survey. In M. R.A. Thomson, J.A.C. Thomson, and J. Thomson, (Eds.), *Geological evolution of Antarctica: New York*, Cambridge University Press, p. 299–304.

Behrendt, J.C., (1999). Crustal and lithospheric structure of the West Antarctic Rift System from geophysical investigations – a review. *Global and Planetary Change, 23*, 25- 44.

Brancolini, G., Busetti, M., Marchetti, A., De Santis, L., Zanolla, C., Cooper, A.K., Cochrane, G.R., Zayatz, I., Belayev, V., Knyazev, M., Vinnikovskaya, O., Davey, F.J., & Hinz, K., (1995b). Descriptive text for the Seismic Stratigraphic Atlas of the Ross Sea, Antarctica *in* A.K. Cooper, P.F. Barker, & G. Brancolini, (Eds.), *Geology and seismic stratigraphy of the Antarctic margin. Antarctic Research Series, 68*, 271–286.

Brotchie, J.F., & Silvester, R., (1969). On crustal flexure. *Journal of Geophysical Research, 74*, 5240 – 5252.

Bry, M., & White, N., (2007). Reappraising elastic thickness variation at oceanic trenches. *Journal of Geophysical Research, 112*, B08414.

Caldwell, J.G., Haxby, W.F., Karig, D.E., & Turcotte, D.L., (1976). On the applicability of a universal elastic trench profile. *Earth and Planetary Science Letters, 31*, 239-246.

Chaput, J., Aster, R.C., Huerta, A., Sun, X., Lloyd, A., Wiens, D., Nyblade, A., Anandakrishnan, S., Winberry, J.P., & Wilson, T. (2014). The crustal thickness of West Antarctica. *Journal of Geophysical Research, 119*, 378-395.

Collier, J. S. & Watts, A. B. (2001). Lithospheric response to volcanic loading by the Canary Islands: constraints from seismic reflection data in their flexural moat. *Geophysical Journal International, 147(3)*, 660–676.

Contreras-Reyes, E. & Osses, A., (2010). Lithospheric flexure modeling seaward of the Chile trench: implications for oceanic plate weakening in the Trench Outer Rise region. *Geophysical Journal International, 182(1)*, 97–112

Cooper, A.K., & Davey, F.J., (1985). Episodic rifting of Phanerozoic rocks in Victoria Land Basin, western Ross Sea, Antarctica. *Science, 229*, 1085-1087.

Cooper, A. K., Davey, F.J., & Cochrane, G.R. (1987). Structure of extensionally rifted crust beneath the western Ross Sea and Iselin Bank, Antarctica, from sonobuoy seismic data. In A.K. Cooper & F.J. Davey (Eds.). *The Antarctic Continental Margin; Geology and Geophysics of the Western Ross Sea (pp. 93-118)*. Circum-Pacific Council for Energy and Mineral Resources, Houston, TX.

Cooper, A.K., Davey, F.J., & Hinz, K. (1991). Crustal extension and origin of sedimentary basins beneath the Ross Sea and the Ross Ice Shelf, Antarctica. *Geological Evolution of Antarctica, 5*, 285-291.

Davey, F.J. & Brancolini, G. (1995). The Late Mesozoic and Cenozoic Structural Setting of the Ross Sea Region. In A. K. Cooper, P. F. Barker, G. Brancolini (Eds.). *Geology and Seismic Stratigraphy of the Antarctic Margin*. https://doi.org/10.1029/AR068p0167.

Davey, F.J., Cande, S.C., & Stock, J.M. (2006). Extension in the western Ross Sea region-links between Adare Basin and Victoria Land Basin. Geophysical Research Letters, 33.

Decesari, R.C., Sorlien, C.C., Luyendyk, B.P., Wilson, D.S., Bartek, L., Diebold, J., & Hopkins, S.E. (2007). Regional seismic stratigraphic correlations of the Ross Sea: Implications for the tectonic history of the West Antarctic Rift System. *USGS Open File Report 2007-1047*, Short Research Paper 052, 4 p.

Di Roberto A., Pompilio M., & Wilch T.I., (2010). Late Miocene submarine volcanism in ANDRILL AND-1B drill core, Ross Embayment, Antarctica. *Geosphere, 6*, 524- 536.

Fielding, C.R. (2018). Stratigraphic architecture of Cenozoic succession in the McMurdo Sound region, Antarctica: An archive of polar paleoenvironmental change in failed rift setting. Sedimentology, 65, 1-61.

Fielding, C.R., Whittaker, J., Henrys, S.A., Wilson, T.J., & Naish, T.R., (2008). Seismic facies and stratigraphy of the Cenozoic succession in McMurdo Sound, Antarctica: implications for tectonic, climatic and glacial history. *Paleogeography, Paleoclimatology, Paleoecology, 260*, 8-29.

Finn, C.A., Muller, R.D., & Panter, K.S., (2005). A Cenozoic diffuse alkaline magmatic province (DAMP) in the southwest Pacific without rift or plume origin. *Geochemistry, Geophysics, Geosystem, 6*, Q02005.

Harwood, D.M., Lacy, L.L., & Levy, R.H., (2002). Future Antarctic Margin Drilling: developing a science plan for McMurdo Sound. ANDRILL SMO Contribution 1. University of Nebraska-Lincoln, Lincoln, NE, p. 301.

Hertz, H., (1884). On the equilibrium of floating elastic plates. *Wiedemann's Annals, 22*, 449–455.

Hinz, K. & Block, M. (1983). Results of Geophysical Investigations in the Weddell Sea and in the Ross Sea, Antarctica. *World Petroleum Congress*.

Horgan, H., Naish, T., Bannister, S., Balfour, N., & Wilson, G. (2005). Seismic stratigraphy of the Ross Island flexural moat under the McMurdo-Ross Ice Shelf, Antarctica, and a prognosis for stratigraphic drilling. *Global Planetary Change, 45*, 83-97.

Jha, S., Harry, D.L., & Schutt, D.L. (2017). Toolbox for Analysis of Flexural Isostasy (TAFI)—A MATLAB toolbox for modeling flexural deformation of the lithosphere. *Geosphere, 13(5)*, 1555–1565. https://doi.org/10.1130/GES01421.1.

Krissek, L., Browne, G., Carter, L., Cowan, E., Dunbar, G., McKay, R., et al. (2007). Sedimentology and Stratigraphy of the AND-1B Core, ANDRILL McMurdo Ice Shelf Project, Antarctica. *ANDRILL Research and Publications, Paper 22*, 185-222.

Kyle, P.R., (1981). Glacial history of the McMurdo Sound area as indicated by the distribution and nature of McMurdo Volcanic Group rocks. In L. D., McGinnis, (Ed.), *Dry Valley Drilling Project: Antarctic Research Series, 33*, 403-412.

Kyle, P.R., (1990). McMurdo volcanic group, western Ross Embayment. In W.E., Le Masurier & J. W. Thomson, (Eds.), *Volcanoes of the Antarctic Plate and Southern Oceans: Antarctic Research Series, 48*, 19–25.

Kyle, P.R., & Cole, J.W. (1974). Structural Control of Volcanism in the McMurdo Volcanic Group, Antarctica. *Bulletin of Volcanology, 38 (1)*, 16-35.

Levitt, D.A. & Sandwell, D.T., (1995). Lithospheric bending at subduction zones based on depth soundings and satellite gravity. *Journal of Geophysical Research, 100*, 379-400

Lloyd, A.J., Weins, D.A., Nyblade, A.A., Anandakrishnan, A., Aster, R.C., Huerta, A.D., et al. (2015). A seismic transect across West Antarctica: Evidence for mantle thermal anomalies beneath the Bentley Subglacial Trench and the Marie Byrd Land Dome. *Journal of Geophysical Research, 120*, 8349-8460

Nadai, A. (1963). *Theory of flow and fracture of solids*. New York, McGraw-Hill, 705 pp.

Naish, T.R., Powell, R.D., Levy, R., Henrys, S., Krissek, L., Niessen, F., Pompilio, M., Scherer, R., Wilson, G., & the ANDRILL-MIS Science Team, (2007). Synthesis of the initial scientific results of the MIS Project (AND- 1B Core), Victoria Land Basin, Antarctica. *Terra Antarctica, 14*, 317–327.

Paulsen, T., Wilson, T.J., Demosthenous, C., Millan, C., Jarrard, R., & Laufer, A.L. (2014). Kinematics of the Neogene Terror Rift: Constraints from calcite twinning strains in the ANDRILL McMurdo Ice Shelf (AND-1B) core, Victoria Land Basin, Antarctica. *Geosphere, 10*, 828-841.

Rocchi, S., Armienti, P., D'Orazio, M., Tonarini, S., Wijbrans, J.R., & Di Vincenzo, G., (2002). Cenozoic magmatism in the western Ross Embayment: Role of mantle plume versus plate dynamics in the development of the West Antarctic Rift System. *Journal of. Geophysical Research, 107*, 2195.

Rocholl, A., Stein, M., Molzahn, M., Hart, S.R. & Wörner, G. (1995). Geochemical evolution of rift magmas by progressive tapping of a stratified mantle source beneath the Ross Sea Rift, Northern Victoria Land, Antarctica. *Earth and Planetary Science Letters, 131*, 207–224, 1995.

Siddoway, C.S., Suzanne, L.B., Fitzgerald, P.G., Fanning, C.M., & Luyendyk, B.P. (2004). Ross Sea mylonites and the timing of intracontinental extension within the West Antarctic rift system. *Geology, 32 (1),* 57-60.

Siddoway, C.S. (2007). Tectonics of the West Antarctic rift system: new light on the history and dynamics of distributed intracontinental extension. In A.K. Cooper, P. J., Barrett, H. Stagg, B. Storey, E. Stump, W. Wise (Eds.), *Antarctica: a Keystone in a Changing World – Proceedings of the 10th International Symposium on Antarctic Earth Sciences (pp. 91-114)*. Washington, DC: The National Academies Press.

Stern, T.A., Davey, F.J., & Delisle, G., 1991, Lithospheric flexure induced by the load of Ross Archipelago, southern Victoria Land, Antarctica. In M.R.A. Thomson, J.A. Crame, & J.W. Thomson, (Eds.), *Geological evolution of Antarctica: Proceedings of the fifth international symposium on Antarctic earth sciences*. Cambridge, United Kingdom, Cambridge University Press, 323–328.

Storey, B.C., Leat, P.T., Weaver, S.D., Pankhurst, R.J., Bradshaw, J.D., & Kelley, S., (1999). Mantle plumes and Antarctica-New Zealand rifting: Evidence from Mid Cretaceous mafic dykes. *Journal of the Geological Society of London, 156*, 659 – 671.

Turcotte, D. L., (1979). Flexure. *Advances in Geophysics, 21*, 51-86.

Walcott, R.I., (1970). Flexural rigidity, thickness and viscosity of the lithosphere. *Journal of Geophysical Research, 75*, 3941-3954.

Watts, A.B., & Cochran, J.R., (1974). Gravity anomalies and flexure of the lithosphere along the Hawaiian-Emperor Seamount chain. *Royal Astronomical Society Geophysical Journal, 38*, 119-141.

Webb, P.N., & Wilson, G.S., (Eds.), (1995). The Cape Roberts Project—Antarctic stratigraphic drilling. *Proceedings of the U.S. Planning Workshop, Report-Byrd Polar Research Center, 10*,

Wenman, C.P., Harry, D.L., & Jha, S. (in review). Tectonic and Stratigraphic Evolution of the Victoria Land Basin and Ross Island. *Geochemistry, Geophysics, Geosystems.*

Wilson, D.S., & Luyendyk, B.P. (2009). West Antarctic paleotopography estimated at the Eocene-Oligocene climate transition. *Geophysical Research Letters, 36*, L16302.

Wilson, G.S., Levy, R.H., Browne, G., Cody, R., Dunbar, N., Florindo, F., & ANDRILL-MIS Science Team (2007). Preliminary Integrated Chronostratigraphy of the AND-1B Core, ANDRILL McMurdo Ice Shelf Project, Antarctica. *ANDRILL Research and Publications, Paper 46,* 297-316.

Wilson, G.S., Naish, T., Jordon, T., Damaske, D., Ali, M., Horgan, H., Balfour, N., Watts, A., Bannister, S., & the ANDRILL Site Survey Team, (2003). Using flexural modeling and geophysical data to define Neogene stratigraphic drilling targets in moat basins beneath the McMurdo Ice Shelf. *Geophysical Research Abstracts, 5*, 05682.

Wright, A.C., & Kyle, P.R., (1990a). A.15 Mount Bird. In W.E. Le Masurier, & J.W. Thomson (Eds.), *Volcanoes of the Antarctica Plate and Southern Oceans. Antarctic Research Series, 48*, 97–98.

Wright, A.C., & Kyle, P.R., (1990b). A.16 Mount Terror. In W.E. Le Masurier, & J.W. Thomson (Eds.), *Volcanoes of the Antarctica Plate and Southern Oceans. Antarctic Research Series, 48*, 99–102.

CHAPTER 2
Toolbox for Analysis of Flexural Isostasy (TAFI) – A MATLAB® toolbox for modeling flexural deformation of the lithosphere[1]

2.1 Introduction

In this paper, we present the Toolbox for Analysis of Flexural Isostasy (TAFI). TAFI is a suite of MATLAB tools that supports forward modeling of flexural subsidence and uplift of the lithosphere in response to tectonic loading. TAFI also calculates the gravity anomaly due to flexure of the lithosphere and allows for easy comparison of modeled deflection and gravity curves with observations to facilitate a rapid interactive search for the best fitting flexural model.

Vertical tectonic loads emplaced on the lithosphere may be in the form of static surface loads, such as topography, static subsurface loads due to lateral variations in lithosphere or asthenosphere density, or dynamic subsurface loads created by tractions at the base of the lithosphere imposed by flow in the underlying mantle. These tectonic loads result in vertical deformation, typically involving subsidence in the vicinity of the load (assuming the load represents an addition of weight to the lithosphere) and uplift in surrounding areas (the peripheral "bulge") (Figure 2.1). The magnitude and wavelength of the flexural deflection depend on the magnitude of the load and the strength of the lithosphere, with greater strength resulting in more broadly distributed (larger wavelength) deformation. Flexure results in variations in the regional gravity field due to deformation of density interfaces within the lithosphere. Density interfaces may include the crust-mantle boundary, the interface between the sedimentary basin fill and underlying rocks, the seafloor in marine areas, and other significant intra-crustal interfaces specified by the user. The relationships between flexural deformation and the gravity field

[1]Jha, S., Harry, D.L., & Schutt, D.L. (2017). Toolbox for Analysis of Flexural Isostasy (TAFI)—A MATLAB toolbox for modeling flexural deformation of the lithosphere. *Geosphere*, *13(5)*, 1555–1565. https://doi.org/10.1130/GES01421.1.

are dependent upon the partitioning of the load between the surface (topography) and subsurface (buried density anomalies) components (Karner and Watts, 1983; Forsyth, 1985; Macario et al., 1995; McKenzie, 2003).

The flexural behavior of the Earth's lithosphere can be approximated with a model in which the lithosphere is treated as a thin elastic plate overlying an inviscid fluid asthenosphere (Watts, 2001). Analytical solutions describing the flexural bending of homogeneous infinite and semi-infinite thin elastic plates subjected to point, line or harmonic loads have been widely used in the flexural isostatic analysis (Hertz, 1884; Nadai, 1963; Walcott, 1970). These elastic plate models have been shown to match the long-wavelength (> 25 km) bathymetric features and the gravity field near most major oceanic tectonic features, including ocean trenches, ridges, island chains, transform faults, and hotspot swells (Turcotte, 1979; Watts et al., 1980; Bodine et al., 1981; Dahlen, 1981). On continents, elastic plate models have also been applied to analyze isostasy in continental rifts, mountain belts, and sedimentary basins (e.g. Karner and Watts, 1983; Watts et al., 1982; Chase and Wallace, 1988; Forsyth, 1985; McNutt et al., 1988; Flemings and Jordan, 1989; Wessel and Karner, 1989; Stern and Brink, 1989; Ten Brink et al., 1997). Elastic plate models have also been used to assess glacial isostatic rebound (e.g. Stern et al., 2005), and to analyze isostasy on scales spanning continents and ocean basins (Banks et al., 1977; Watts and Burov, 2003; McKenzie and Bowin, 2003; Watts, 1978; McNutt and Menard, 1982; Lowry and Smith, 1994; Djomani et al., 1995; McKenzie and Fairhead, 1997; Petit and Ebinger, 2000; Flück et al., 2003; Crosby and McKenzie, 2009).

TAFI provides an easy-to-use interactive tool to model isostatic deformation of the lithosphere as flexural bending of an elastic plate. TAFI consists of a suite of MATLAB scripts

and functions, coded as m-files, which facilitate rapid interactive forward modeling of flexural deformation of a thin elastic lithosphere overlying an inviscid asthenosphere. Only intrinsic MATLAB functions are used, providing portability across operating systems without the need for special libraries or packages other than MATLAB itself. TAFI computes analytical Green's functions that represent the flexural response of a thin elastic plate subjected to vertical impulsive (line or point) loads. The flexural response for non-impulsive loads can be obtained by convolving the Green's Functions with discretized functions representing loads that are distributed either in a radially symmetric pattern (simulating, for example, a seamount), along linear profiles (simulating loading by a thrust belt or seamount chain), or arbitrarily on an x-y plane (topography).

The Green's function for a point load represents a two-dimensional (2-D) radial cross-section in the r-z plane across a radially symmetric flexural basin, normalized by the magnitude of the load. In TAFI, these are referred to as axisymmetric plate models, with the basin shape described along with a profile measured radially away from the point load. The point load Green's function can be convolved with a spatially distributed load to compute the flexural response for axisymmetric loads of finite radius, and for loads that are distributed arbitrarily in the horizontal (x and y) directions. In the first instance, the user supplies a load discretized as a function of radial distance, with TAFI returning a flexural profile across a similarly axisymmetric basin. In the second instance, the user supplies a load discretized on an x-y grid. In this case, TAFI returns a grid representing the three-dimensional (x, y, and depth) shape of the basin. Accordingly, TAFI refers to such models as 3-D plate models.

The Green's function for a line load is a 2-D flexural profile (in the x-z plane) across a basin of infinite length, normalized by the magnitude of the load. In TAFI these are referred to as 2-D plate models, with the basin shape described along with a profile measured perpendicular to

the trend of the line load. TAFI computes the flexural deformation for spatially distributed 2-D loads (loads with finite width and infinite along-strike extent) by convolving the line load Green's function with a load discretized along a profile trending perpendicular to strike (the x-direction). Greens functions for both infinite (unbroken) plates and semi-infinite (broken) plates are provided. For 2-D models, TAFI also provides an analytical solution for harmonic loads, in which the load magnitude varies sinusoidally in the x-z plane and is of infinite extent in the y-direction.

TAFI computes the gravity field resulting from the flexed plate using Parker's method (Parker, 1973). This allows the user to specify a layered density structure for the lithosphere, with the gravitational attraction of each flexed layer summed to compute the total gravity anomaly. Examples of density interfaces that contribute strongly to the gravity anomaly are the crust-mantle boundary, the interface between the sedimentary basin fill and underlying crust, and in marine environments, the seafloor.

The MATLAB geodynamic modeling functions provided in TAFI to calculate plate flexure and the corresponding gravity anomaly are similar to those available in other software packages (e.g., Lithflex1 and Lithflex2, http://csdms.colorado.edu; Flex2D, www.ux.uis.no/~nestor/work/programs.html; MECAIR, http://aconcagua.geol.usu.edu/~arlowry/code_release.html; gFlex, https://github.com/awickert/gFlex and MATLAB routines by Fredrik Simons, http://geoweb.princeton.edu/people/simons/software.html). The primary feature that distinguishes TAFI from these other software packages is TAFI's easy to use graphical user interface (GUI), which facilitates interactive flexural modeling through easy modification of model parameters and instantaneous visual comparison of model results to data. The GUI provides a powerful instructional tool, allowing users to interactively explore how changes in plate boundary conditions, plate strength, load position and magnitude, and superposition of loads affect flexural

deformation. TAFI's GUI is designed to serve as a template to which additional isostatic analysis tools, such as solutions for different plate rheologies (e.g., viscous, viscoelastic, or visco-plastic), may be added by users familiar with MATLAB coding.

2.2 Methods

2.2.1 Calculating flexural deformation

TAFI models the lithosphere and asthenosphere system as a thin elastic plate of constant flexural rigidity overlying an inviscid substrate. Flexure is the result of a vertical load (pressure) applied to the plate. Horizontal forces are neglected, as these have a relatively small effect on the elastic flexural profile under reasonable geological conditions (Caldwell et al., 1976; Turcotte, 1979). The equations describing the vertical deflection of the plate in 2-D Cartesian and radial coordinates are:

$$D\nabla^4 w(x,y) + \Delta\rho g w(x,y) = q_a(x,y) \tag{2.1}$$

$$D\left(\frac{d^2}{d\boldsymbol{r}^2} + \frac{1}{r^2}\frac{d}{d\boldsymbol{r}}\right)^2 w(\boldsymbol{r}) + \Delta\rho g w(\boldsymbol{r}) = q_a(\boldsymbol{r}) \tag{2.2}$$

where w is the vertical deflection of the plate, ∇^4 is the fourth derivative gradient operator, q_a is the vertical load applied to the plate, $\Delta\rho$ is the density contrast between the mantle underlying the plate and the material filling the basin (usually either water or sedimentary rocks), x, y, and $\boldsymbol{r}$ are Cartesian and radial coordinate positions (respectively), g is gravitational acceleration, and D is the flexural rigidity of the lithosphere (Hertz, 1884; Nadai, 1963). D depends on the thickness of the elastic plate (T_e), the plate's Young's modulus (E) and Poisson's ratio (v):

$$D = \frac{ET_e^3}{12(1-v^2)} \tag{2.3}$$

Analytical solutions of Equations 2.1 and 2.2 for a line load and infinite (continuous) plate geometry, a line load and semi-infinite (broken) plate geometry, and a point load and infinite plate geometry are:

$$w(x) = Q_0 \frac{\alpha^3}{8D} e^{-x/\alpha} \left(cos \frac{x}{\alpha} + sin \frac{x}{\alpha} \right)$$ infinite plate, line load (2.4)

$$w(x) = Q_0 \frac{\alpha^3}{4D} e^{-x/\alpha} cos \frac{x}{\alpha}$$ semi-infinite plate, line load (2.5)

$$w(r) = Q_0 \frac{\alpha^2}{2\pi D} kei \frac{r}{\alpha}$$ infinite plate, point load (2.6)

where α is the flexural parameter, which depends on the flexural rigidity and density structure of the plate (Table 2.1), Q_0 is the load magnitude, and *kei* is the zeroth-order Kelvin function (Hertz, 1884; Nadai, 1963). For the special case of $Q_0 = 1$, Equations 2.4-2.6 are impulse responses (Green's Functions), which can be convolved with load functions to obtain the flexural deformation of the plate under geologically realistic spatially distributed (non-impulsive) loads. For a distributed two-dimensional sinusoidal surface (topographic) load on an infinite plate, the solution to Equation 2.1 is:

$$w(x) = \frac{Q_0}{(\rho_m - \rho_c)g + D\left(\frac{2\pi}{\lambda}\right)^4} sin 2\pi \frac{x}{\lambda} \quad (2.7)$$

where ρ_m is the density of mantle, ρ_c is the density of the rocks forming the topography and filling the basin (usually the crystalline upper crust), and λ is the wavelength of the load (Turcotte, 1979).

The maximum deflection of the plate (w_{max}), amplitude of the peripheral uplift (w_b), distance from the load to the crest of the peripheral uplift (x_b), and the point of zero deflection (x_0) between the basin and peripheral uplift are attributes commonly used to compare flexural models to observations (Figure 2.1). These attributes, which describe the shape and width of the basin, depend on the flexural parameter, α, and are obtained in closed form for the line load models (Table 2.1). For the point load and harmonic load models, these values are determined by searching the calculated deflection curve for the minimum, maximum and zero value (nearest to the load for the point load model, or nearest the model origin for the harmonic load model).

2.2.2 Calculating the gravity anomaly

Flexure of density interfaces within the lithosphere produces a gravity anomaly that is dependent upon the density contrast across the interface, the mean depth of the interface, and the shape of the flexural deformation. The gravity anomaly produced by flexure of a single density interface is calculated using Parker's method (Parker, 1973):

$$\mathcal{F}(\Delta g) = -2\pi G \Delta\rho \exp(-|\boldsymbol{k}|z_0) \sum_{n=1}^{\infty} \frac{|k|^{n-1}}{n!} \mathcal{F}[h^n(\boldsymbol{r})] \quad (2.8)$$

Here, $\mathcal{F}(\Delta g)$ is the Fourier transform of the gravity anomaly, $\boldsymbol{r}$ is the position vector, $\boldsymbol{k}$ is the wavenumber, G is the Universal Gravitational Constant, $\Delta\rho$ is the density contrast across the interface, $\mathcal{F}(h)$ is the Fourier transform of the de-trended flexural relief (h) on the interface (prescribed by the plate flexure), and z_0 is the mean depth of the interface. Inverse Fourier transforming $\mathcal{F}(\Delta g)$ provides the gravity field produced by topography on the buried interface. The gravitational effect of multiple density interfaces within the lithosphere is obtained by summing the effect of each interface.

2.3 Program design and computational approach

TAFI is structured hierarchically, with an upper-level script that provides a graphical user interface (GUI) to lower-level functions that perform the geodynamic calculations, visualization and Input/Output operations (Figure 2.2, Table 2.2). The appearance of the GUI is defined in the file "TAFI.fig" (Figure 2.3). This is a MATLAB encoded file that defines the elements available from within the GUI. TAFI.fig also associates the GUI elements with actions and variables used in TAFI for modeling and visualization. The actions invoked by user interaction with the GUI elements are prescribed in the elements' respective callback functions, which are coded in the file "TAFI.m". The callback functions call TAFI lower-level functions that perform computations,

data Input/Output, or visualization tasks and pass variable values obtained from the GUI elements (for example, the flexural rigidity) to these functions.

The geodynamic and gravity modeling functions are MATLAB implementations of Equations 2.4-2.7 and Equation 2.8, respectively. These functions can also be called from the command line, allowing access from outside of the GUI or from within user-written programs (Table 2.3). The MATLAB implementation of Equations 2.4-2.6 to obtain Green's Functions (by setting $Q_0 = 1$) for the flexural response of an elastic plate to impulse (line or point) loads is straightforward, as is the implementation of Equation 2.7 to describe harmonic loading. Flexure due to non-unit impulse loads is obtained by scaling the Green's Function by a user-specified load magnitude. For distributed 2-D loads, the flexural response is calculated by convolving the user-supplied discretized load function with the semi-infinite or continuous plate Green's Functions for line loads (Equations 2.4-2.5). For 3-D distributed loads, the flexural response is calculated by convolving the user-specified load matrix with point load Green's function (Equation 2.6). MATLAB's intrinsic convolution functions require that the load and Green's functions be discretized at similar uniform intervals. For 2-D models, the load is resampled to the Green's function interval (specified by the user) prior to convolving. For 3-D loads, the Green's function is calculated at the grid spacing used in the user-supplied load function, and no re-sampling is required.

To compute the gravity anomaly, TAFI requires the Fourier Transform of the deflection in the wavenumber domain (Equation 2.8). Estimation of the gravity field in the wavenumber domain via the series summation in Equation 2.8 is then straightforward. The gravity field in the wavenumber domain is then inverse Fourier transformed to yield the gravity field as a function of position. Four terms of the series in Equation 2.8 are used, as empirical testing showed this is

sufficient to reproduce the calculated gravity anomaly to within 10^{-9} mGal in realistic modeling scenarios.

2.4 Flexure and gravity modeling using TAFI

TAFI's installation, directory structure, use and properties of GUI elements, default behaviors, input/output file formats and other operating instructions are described in Supplemental File 1. Here, we briefly describe TAFI's functionality. All operations described below can be done outside of TAFI's GUI by invoking TAFI's functions from the command line as described in the Supplemental File. The GUI is designed to allow the user to vary model parameters and observe the results immediately using sliders, edit boxes, and drop-down menus, thus facilitating the interactive fitting of flexural models to data.

Flexure and gravity modeling in TAFI require passing model parameters as arguments to TAFI's geodynamic modeling functions, which return calculated deflection and gravity fields. The model parameters are specified in the function invocation when using TAFI from the MATLAB command line. When using the TAFI GUI, the model parameters are specified with sliders, edit boxes, and dropdown menus (Figure 2.3). The flexure and gravity curves are displayed in the GUI plot window and are updated interactively when the model parameters are changed.

To build a flexure model in TAFI, the user must specify the plate type, load geometry, flexural rigidity, load magnitude, load position, and density contrast between the mantle and basin fill. The functional form of the flexural response of the elastic plate for 2-D and 3-D flexure models are prescribed by the plate geometry (infinite or semi-infinite plate) and the load geometry (selecting from the line, point, 2-D harmonic, 2-D distributed, axisymmetric distributed, or 3-D distributed load geometries; Table 2.4). The remaining model parameters are defined by the user and passed to TAFI's geodynamic functions. In the case of distributed loads (2-D or 3-D), load

magnitudes are provided by the user as a MATLAB column-vector (2-D) or matrix (3-D). For sinusoidal loads, the load wavelength (λ) instead of the load magnitude is passed to the corresponding geodynamic function. In the GUI, the user can vary these variables with sliders and edit boxes and see the change in the computed flexural curve displayed in real-time. Using the TAFI GUI, the user can also interactively change the load position and scale the magnitude of distributed loads. TAFI uses default values for g (9.8 m/s^2), Earth's radius (R, 6370 km), E (8.5 x 10^{10} N/m^2) and Poisson's ratio (0.25). These values can be modified by users as described in Supplemental file.

The elastic plate is required to have at least two density interfaces, one at the top of the plate and another at the base of the plate. These density interfaces represent the boundaries between the basin fill and underlying crust, and between the crust and mantle (Figure 2.1). The mantle and infill densities are required to calculate the flexural parameter (α) (Table 2.1), which is used to compute the flexural deflection of the lithosphere for non-harmonic loads (Equations 2.4-2.6). The density contrasts between these layers and the depth of interfaces are also used to calculate the gravity anomaly associated with flexure of the lithosphere (Equation 2.8). When using the TAFI GUI, the density interfaces are defined by specifying the basin fill, crust and mantle densities. When invoking TAFI from the MATLAB command line, the interfaces are defined by specifying the density contrasts between the layers and their depths. Additional density interfaces, representing lithological boundaries within the lithosphere, can be specified when accessing TAFI from the command line. These additional density interfaces are used to compute the gravity anomaly but are not used in the flexural deformation calculation.

2.5 Using TAFI – Aleutian Trench 2-D case study

TAFI can be used to explore plate flexural behavior without loading data. However, the primary purpose of TAFI is to facilitate forward modeling to determine the flexural parameters that best fit the observed vertical deflection and gravity data. To demonstrate the TAFI workflow, we model the flexural deformation of the lithosphere along with a 2-D profile crossing the Aleutian trench (Figure 2.4). The Aleutian trench extends ~2900 km from the Gulf of Alaska to the Kamchatka peninsula and is the plate boundary where the Pacific plate is being subducted under the North American plate. A number of studies have shown that the seafloor bathymetry near the Aleutian Trench can be fitted with a 2-D semi-infinite elastic plate model subjected to a line load (Caldwell et al., 1976; Levitt and Sandwell, 1995; Watts, 2001; Bry and White, 2007).

We chose a profile that crosses the trench about 45 km to the west of the "Aleutian 8" profile of Levitt and Sandwell (1995) (Figure 2.4). Bathymetric and Free Air gravity data along this profile were downloaded from the U.S. National Geophysical Data Center (NGDC). The data were prepared for use in TAFI by removing the mean and regional tilt to correct for elevation changes not associated with flexure (primarily, changes in seafloor depth due to plate age). The corrected flexural and gravity profiles were saved in text (.txt) formats (format described in Appendix A1).

Launching TAFI from the GUI will show the default infinite plate model. Dropdown menus are used to change the plate geometry and load shape from the default settings to semi-infinite and 2-D line load respectively. Following Levitt and Sandwell (1995), the TAFI model is then modified to change the infill, crust, and mantle densities and the depths to their associated interfaces to 1000 kg/m^3, 2750 kg/m^3, 3200 kg/m^3, 7000 m and 12000 m respectively. TAFI's plot window displays both the initial and modified flexure and gravity curves.

To constrain the flexure and gravity modeling of Aleutian trench by curve fitting in TAFI, the Aleutian bathymetry and gravity data (saved earlier) are imported into TAFI (Figure 2.5) (data import process and file format are described in the supplemental file). Curve fitting involves adjusting the modeled flexure and gravity curves to fit the imported data. This is done by revising the flexural rigidity, load magnitude, and load position through their respective sliders and edit boxes in TAFI's GUI. The model curves are updated each time a parameter value is changed, with the new model curves added to the existing plot. The curve fitting process is terminated when the modeled curves fit the data reasonably well (Figure 2.6). The final flexural model parameters and attributes for best-fitting Aleutian trench TAFI model (Figure 2.6) is found to lie within the range of values estimated by Levitt and Sandwell (1995) and Bry and White (2007) (Table 2.5).

2.6 Code verification

The flexural responses for 2-D and 3-D line and point loads (Equations 2.4-2.6) and 2-D sinusoidal loads (Equation 2.7) were verified by comparing the results obtained from TAFI with solutions computed in Microsoft Excel, and by comparing the zero-crossing, maximum deflection, and flexural bulge position and amplitude with analytical solutions where available (Table 2.1). Gravity solutions for the line, point, and harmonic loads were verified by comparing TAFI solutions with gravity models calculated from the flexural admittance function (Watts, 2001). TAFI's solutions for distributed 3-D loads were verified by computing 3-D models with i) a point load located in the center of the load grid, and ii) a line load crossing the load grid. Radial deflection and gravity profiles extending away from the point load and striking perpendicular to the line load were verified to match with TAFI's comparable axisymmetric point load and 2-D line load solutions, respectively (Figure 2.7).

2.7 Summary

The Toolbox for Analysis of Flexural Isostasy (TAFI) consists of MATLAB functions that compute the flexural response of an infinite or semi-infinite thin elastic plate overlying an inviscid substrate and subjected to the line, point and 2-D periodic loads. TAFI also provides functions to convolve the flexural Green's Functions with non-impulsive loads, allowing computation of deflection under spatially distributed 2-D, or 3-D loads and provides functions to compute the Bouguer or Free Air gravity fields associated with plate flexure. The geodynamic functions in TAFI can be called from the MATLAB user interface or within user-written MATLAB code or accessed through TAFI's graphical user interface (GUI). The GUI facilitates interactive flexural modeling and comparison of the model to gravity observations and data constraining flexural subsidence and uplift. TAFI uses only MATLAB intrinsic functions and functions distributed as m-files with TAFI and does not require additional Toolboxes or libraries.

2.8 Acknowledgments

We would like to thank geophysics graduate and undergraduate students of the Department of Geosciences, Warner College of Natural Resources, Colorado State University who reviewed the toolbox and provided constructive comments. We thank Dr. Andrew Wickert, the University of Minnesota, whose reviews made this paper better. We also thank the science Editor of Geosphere, Dr. Raymond M. Russo for his helpful suggestions. This material is based upon work supported by the National Science Foundation under Grants No. 1043700 and Grant No. 1358664, and under Cooperative Agreement No. 0342484 through subawards administered and issued by the ANDRILL Science Management Office at the University of Nebraska-Lincoln, as part of the ANDRILL U.S. Science Support Program.

2.9 Figures for chapter 2

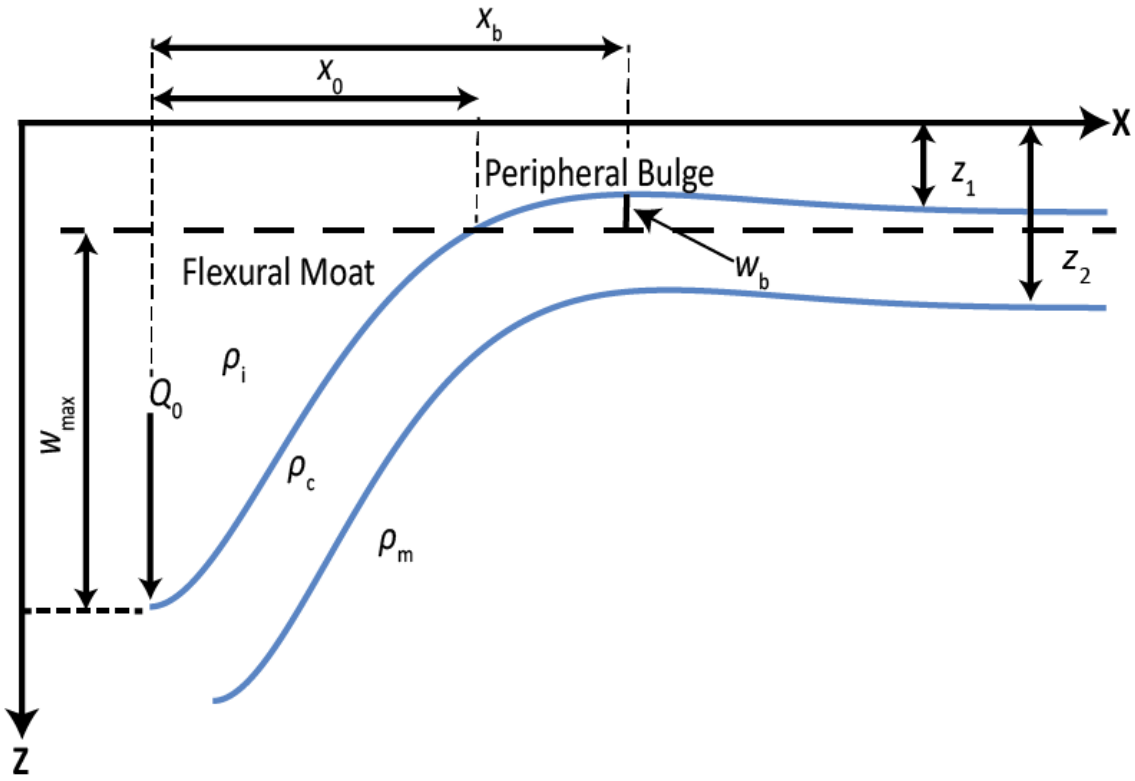

Figure 2.1. Flexure of an elastic plate under an applied line load Q_0. Variables characterizing the shape of the basin are the distance between the load position to the crest of the flexural bulge, x_b, the distance from the load to the point of zero deflection, x_0, the maximum deflection of the basin, w_{max}, and the amplitude of peripheral uplift, w_b. Density interfaces are present at the surface and base of the plate, at depths Z_1 and Z_2 prior to flexural bending, respectively. The density of the infill, crust, and mantle (are ρ_i, ρ_c and ρ_m respectively. Additional optional density interfaces within the plate (not shown) can be used when computing the gravitational response (see text). The position of load (x = 0) is at the position on x-axis, corresponding to the deepest part of the flexural moat.

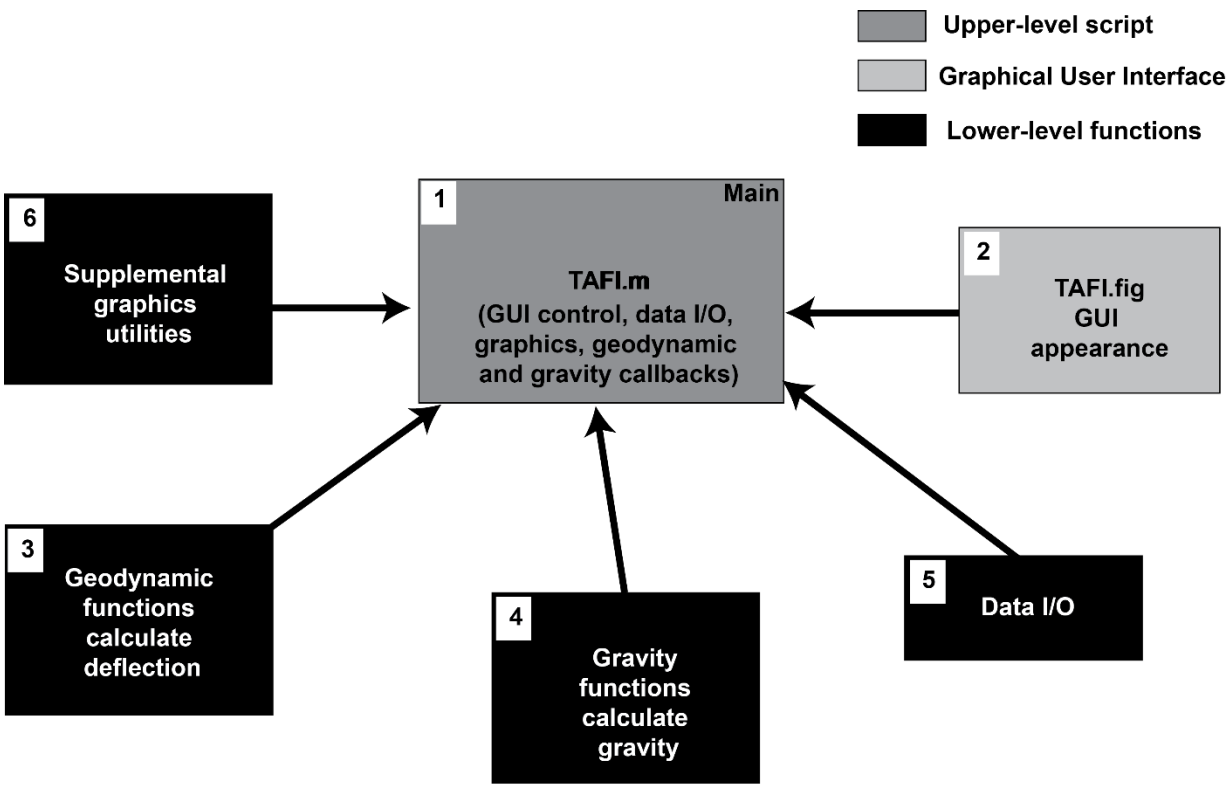

Figure 2.2. The hierarchical structure of TAFI. Upper-level script (TAFI.m) provides a graphical user interface (TAFI.fig) to lower-level functions that perform the geodynamic and gravity calculations and data and model input/output utilities. Supplemental graphic utilities are used to plot model results. Numbers correspond to TAFI's MATLAB functions (Table 2.2).

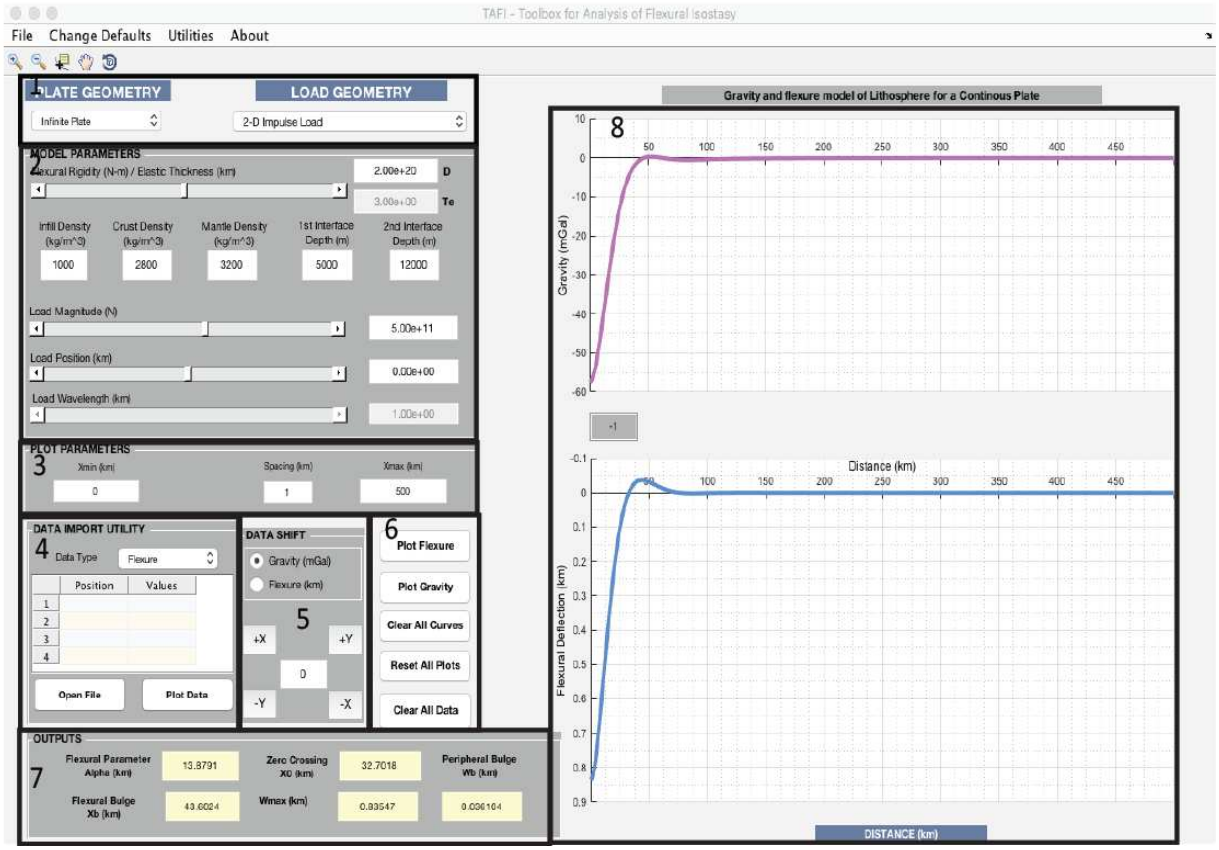

Figure 2.3. TAFI GUI. Clicking on green circles activates a dynamic figure demonstrating GUI features. These include i) available plate geometry (pull-down menu); ii) available load geometry (pull-down menu); iii) changing the flexural rigidity (slider); iv) changing the load magnitude (slider). Clicking on the red circle resets the figure to its initial display. Other model parameters controlled with sliders and text boxes are the load position, load wavelength for harmonic loads, and plate density structure (infill density, crust density, mantle density, and the respective interface depths). Plot appearance is controlled with "Xmin", "Xmax" and "Spacing" in the "Plot Parameters" panel. Flexure or gravity data can be imported using the "Data Import Utility", which prompts for an input file name. The data is plotted by clicking the "Plot Data" button. X, Y, Z buttons and edit box in the "Data Shift" panel allow data to be shifted horizontally and vertically to adjust the model fit. Buttons to interact with the imported data and plots are also provided. The flexural parameter (α), zero crossing distance (x_0), flexural bulge position (x_b), the maximum flexural depth (w_{max}) and the amplitude of peripheral bulge (w_b) are displayed in the Output panel. Flexure and gravity models and imported data are shown in the Plot panel.

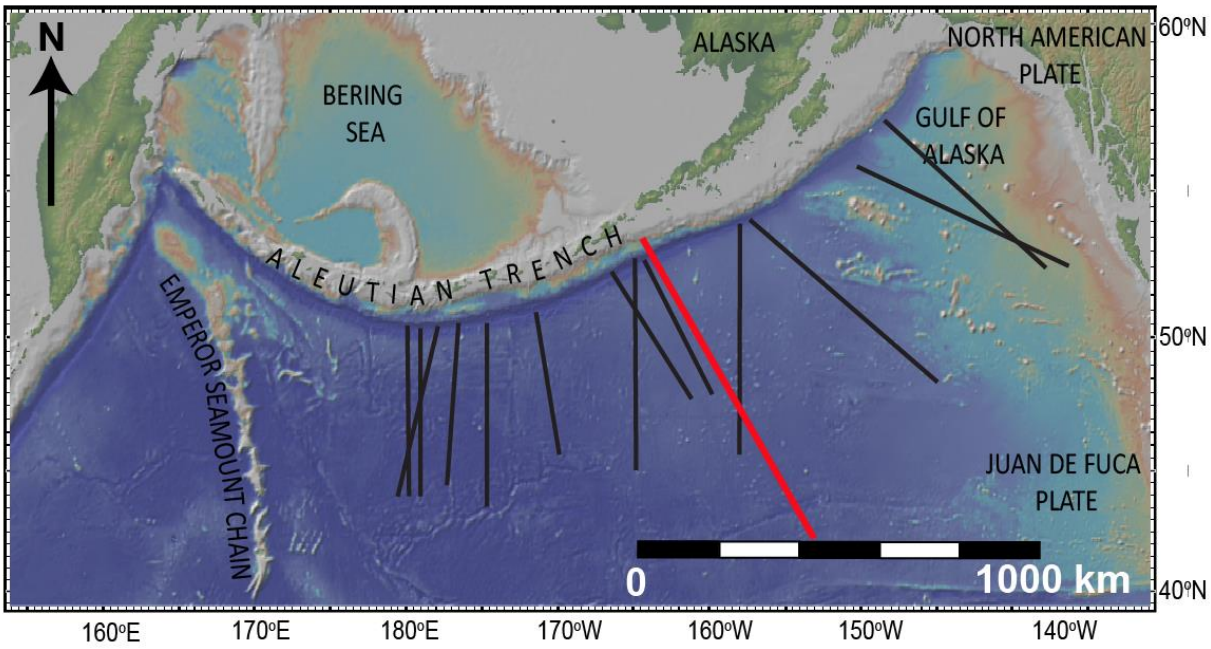

Figure 2.4. Location of Aleutian trench flexural profile (red line). Black lines are from Levitt and Sandwell (1995).

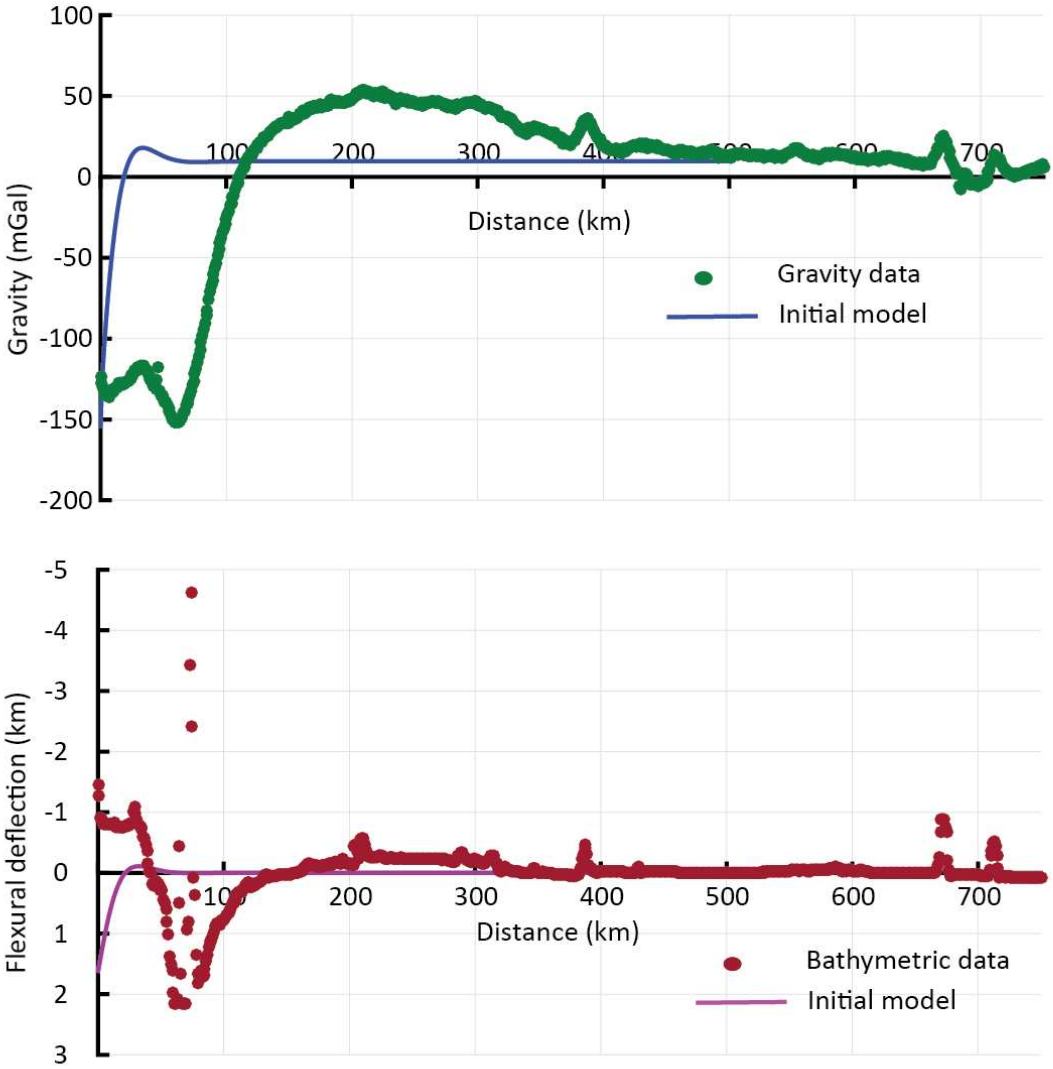

Figure 2.5. Gravity and flexure profiles for default semi-infinite line load model. Bathymetry and free air gravity along with the Aleutian trench profile (Figure 2.4) shown for comparison. The position of load (x = 0) is at the deepest part of the initial model.

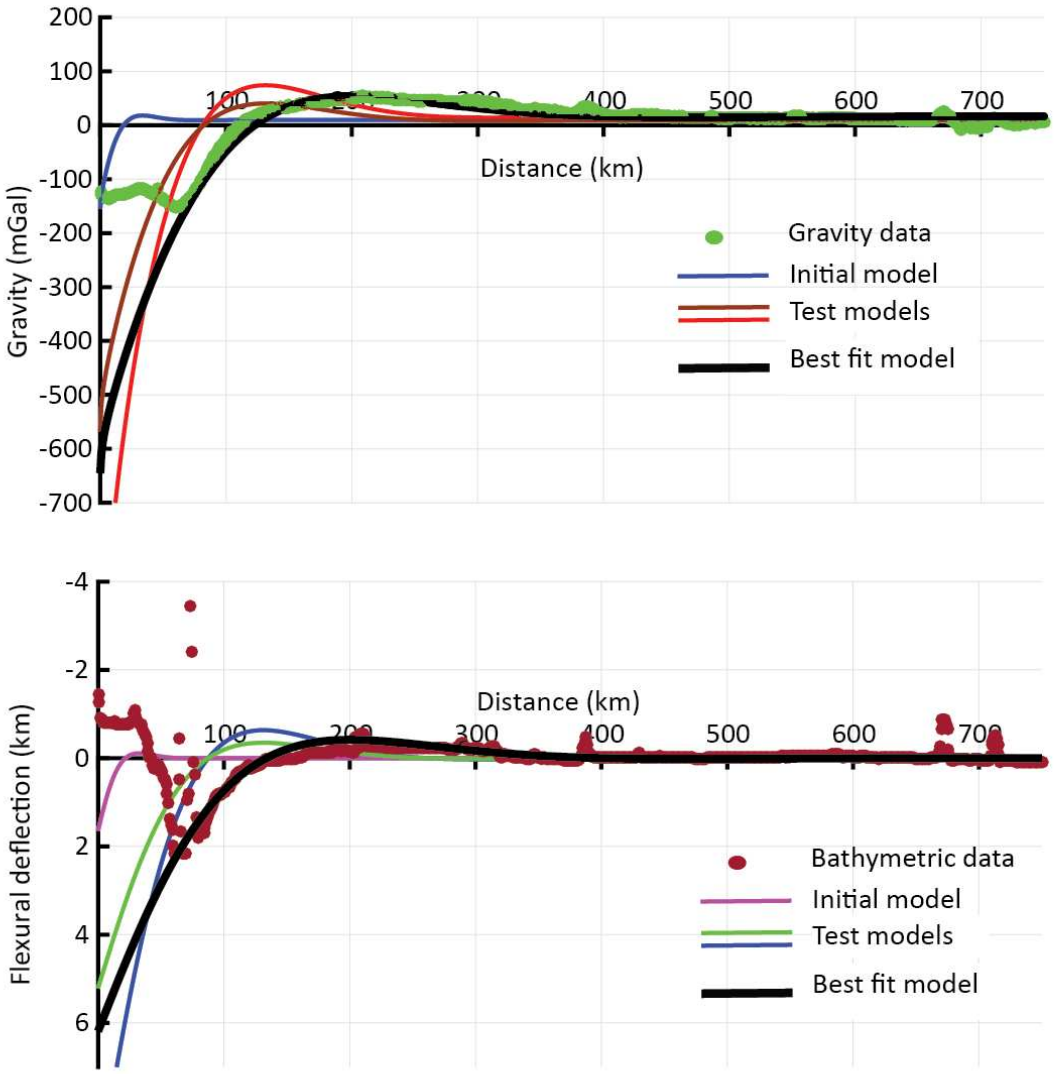

Figure 2.6. Curve fitting process of TAFI, showing initial gravity and flexure model, Aleutian trench gravity and bathymetry, and the gravity and flexure curves for the best fitting model (Table 2.1). The test curves were created by changing the rigidity and load sliders.

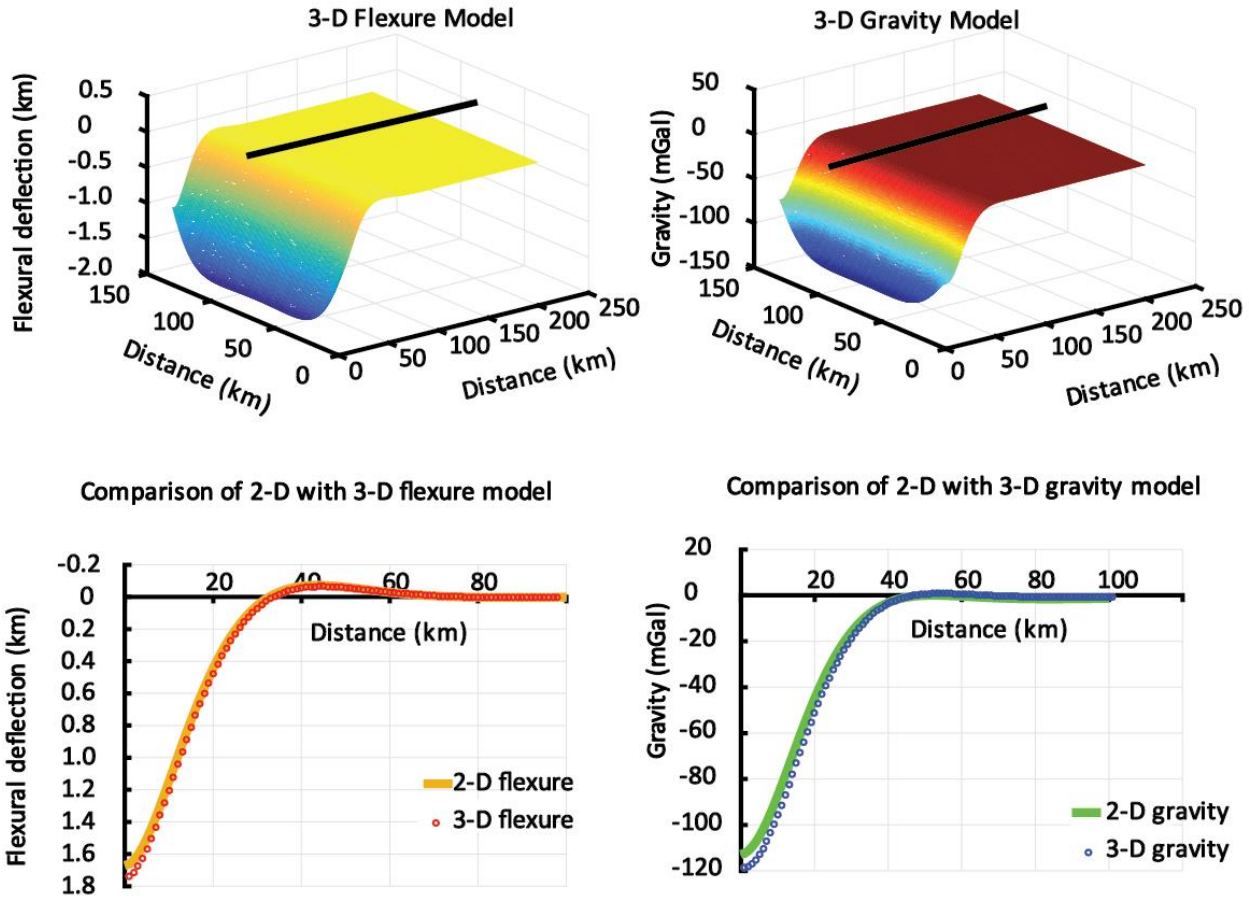

Figure 2.7. TAFI 3-D numerical model showing solution for a line load. The load is located along the left (y=0 km) edge of the model and has a magnitude of 10^9 N/m. Other model parameters are as in Figure 2.3. Top row: Deflection (left) and gravity field (right). Bottom row: Comparison of TAFI's analytical line load solution (solid lines) with a 3-D numerical solution (circles). The profile location is indicated by solid black lines in the figures in the top row. The mismatch between the analytical and numerical solutions near x = 0 is due to an approximation of Kelvin's function used in the axisymmetric Green's function. The Kelvin function returns "infinity" at radial coordinate, r = 0. To overcome this issue, r is assigned a small value (10^{-18}) instead of 0.

2.10 Tables for chapter 2

Table 2.1. Output parameters characterizing the flexural basin shape

Isostatic model	Zero crossing distance (x_0)	Flexural Bulge Position (x_b)	Flexural Parameter (α)	Peripheral Bulge Amplitude (w_b)
Elastic half-space, 2-D line load*	$\frac{\pi}{2}\alpha$	$\frac{3\pi}{4}\alpha$	$\left[\frac{4D}{(\rho_m-\rho_i)g}\right]^{1/4}$	$-0.067\frac{Q_0\alpha^3}{4D}$
Elastic continuous plate, 2-D line load*	$\frac{3\pi}{4}\alpha$	$\pi\alpha$	$\left[\frac{4D}{(\rho_m-\rho_i)g}\right]^{1/4}$	$-0.0432\frac{Q_0\alpha^3}{8D}$
Elastic continuous plate, point load#	-	-	$\left[\frac{D}{(\rho_m-\rho_i)+\frac{ET_e}{R^2}}\right]^{1/4}$ #	$Q_0\frac{\alpha^2}{2\pi D}kei\frac{r_b}{\alpha}$
Elastic continuous plate, 2-D sinusoidal load*	$\frac{\lambda}{2}$	$\frac{\lambda}{4}$	$\left[\frac{D}{\rho_i g}\right]^{1/4}$ *	$\frac{-Q_0}{(\rho_m-\rho_c)g+D\left(\frac{2\pi}{\lambda}\right)^4}$

Note: 2-D - two-dimensional; α-flexural parameter; D-flexural rigidity; Q_0-load magnitude; ρ_m-mantle density; ρ_i-infill density; r_b-radial position of flexural bulge; λ-sinusoidal load wavelength; E-Young's modulus; T_e-elastic thickness; R-Earth's radius; g-acceleration due to gravity; *kei*-zeroth order of Kelvin function. – (dash)-closed form solutions not known. Parameters are determined by search of solution vector w.
*Turcotte and Schubert (2002).
#Brotchie and Silvester (1969).

Table 2.2: Toolbox for Analysis of Flexural Isostasy (TAFI) directory structure

	Toolbox files	Description	
1	TAFI.m	Main TAFI file, which controls interaction with GUI objects,	
2	TAFI.fig	TAFI GUI file with sliders, edit boxes, buttons, dropdown menus, and plots. Accessed from TAFI.m.	
	Subdirectory	**Second-level subdirectory**	**Description**
5	Example Data (NGDC Aleutian trench data used for a case study in this paper)		Bathymetric data in kilometers. Free Air gravity data in mGal.
3	Geodynamic Functions (Functions to calculate the flexural response of elastic plate)	Geodynamic Utilities	Functions to define default constants and calculate the flexural wavelength (Eqn. 4-6).
		Green's Function	Continuous2D_flex.m, Continuous3D_flex.m, Halfspace2D_flex.m, Continous3Dgrid_flex.m
		Sinusoidal	Harmonic2D_flex.m
4	Gravity Functions (Functions to calculate the gravity anomaly caused by flexure)		gravity_callback.m - Interacts with GUI and parkg.m or parkg_3D.m to calculate gravity anomaly. parkg.m and parkg_3D.m - Uses Parker's (1973) method to calculate gravity anomaly.
6	GUI Functions (Functions to control GUI element behavior and appearance)	Default backups	Backup of TAFI default files.
		GUI Function Utilities	Functions to set slider default ranges and values and enable or disable GUI elements and set TAFI environment.
3	Load Functions (Functions to import, interpolate and convolve spatially distributed loads with Green's functions)	Convolution	Functions to convolve the imported load with Green's function.
		Import Load Import Grid	Load file import utility GUI widget and corresponding MATLAB file which imports distributed load vector (2-D) and grid (3-D).
		Load Function utilities	Utility functions to read, interpolate and remove the imported distributed load.
5	Output Parameters		Outputparam.m - Function to calculate output parameters α, x_b, x_0, w_{max} and w_b

Plot Function		TAFIPlot2D.m and TAFIPlot3D.m - Functions used to plot flexure and gravity response and data constraints.
Manual (Help file for TAFI)	Flexure Manual files	Toolbox for Analysis of Flexural Isostasy (TAFI) .doc and .pdf

Note: Numbers in the first column correspond to boxes in Figure 2.2. Abbreviations: NGDC-National Geophysical Data Center, 2-D – two dimensional, 3-D – three-dimensional, GUI – graphical user interface.
Parameters: α-flexural parameter, x_b – flexural bulge position, x_0 – zero crossing position, w_{max} – maximum flexural amplitude, w_b – peripheral bulge amplitude

Table 2.3. List of functions callable from MATLAB workspace.

Function	Arguments	Description
flexparam.m	D, γ, g, E, Te, R, load geometry, plate geometry	Function to calculate the flexural parameter for a given load and plate geometry.
Continuous2D_flex.m	α, D, x	Green's function for infinite plate and line impulse load.
Continuous3D_flex.m	α, D, x	Green's function for infinite plate and point impulse load.
Continuous3Dgrid_flex.m	α, D, x, y	Green's function for infinite plate and 3-D distributed load.
Halfspace2D_flex.m	α, D, x	Green's function for semi-infinite plate and line impulse load.
Harmonic2D_flex.m	x, λ, Q_0, g, γ, D	Function to calculate flexural response for infinite plate and 2-D sinusoidal load.
parkg.m	w, $\Delta\rho$, z, Δx	Function to calculate the gravity field due to the flexed elastic plate. $\Delta\rho$ and z can be vectors to define multiple interfaces.
parkg_3D.m	nx, ny, Δx, Δy, z, $\Delta\rho$, w	Function to calculate the gravity field due to the flexed elastic plate for a 3-D distributed load.
Loadconv2D.m	w, Q, load geometry, Δx, x	Function to convolve Green's function with a 2-D distributed load.
Loadconv3D.m	w, load scale, 3-D load matrix, nx, ny, Δx, Δy	Function to convolve Green's function with a 3-D distributed load.

Note: 2-D - two dimensional; 3-D - three dimensional; D - flexural rigidity; γ - density contrast between infill and mantle; g - acceleration due to gravity; E - Young's modulus; Te - elastic thickness; R - Earth's radius; x - an array of position along the x-axis; y - an array of position along the y-axis (for load grids); λ - sinusoidal load wavelength; Q_0 - vertical load magnitude; $\Delta\rho$ - an array containing density contrast between successive layers (infill – crust, crust-mantle); z - an array containing the depth of successive density interfaces along z-axis; w - array containing vertical flexural deflection values of plate; Δx - interval spacing along x-axis for a spatially distributed line and point loads as well as load grids; Δy - interval spacing along y-axis for spatially distributed load grids; nx, ny - number of grid nodes along x- and y-axis respectively for a spatially distributed load grid; Q – distributed load magnitude array; load scale - scaling parameter for distributed loads

Table 2.4. TAFI geodynamic functions for different plate and load geometry combinations

Plate geometry	**Load geometry**	**Geodynamic function**
Infinite	2-D impulse load	Continuous2D_flex.m
	3-D impulse load	Continuous3D_flex.m
	Periodic loading	Harmonic2D_flex.m
	2-D distributed load	Continuous2D_flex.m
	Distributed axisymmetric load	Continous3D_flex.m
	3-D distributed load	Continuous3Dgrid_flex.m
Semi-Infinite	2-D impulse load	Halfspace2D_flex.m
	2-D distributed load	Halfspace2D_flex.m

Table 2.5. Best fit model parameters for Aleutian trench

Input parameter	Value	Levitt and Sandwell (1995) *	Bry and White (2007) †
Flexural rigidity (D) (N-m)	2.89×10^{23}	$2.18\text{x}10^{22}$-$3.23\text{x}10^{24}$	$6.48\text{x}10^{20}$ - $4.55\text{x}10^{23}$
Infill density (ρ_i) (kg/m^3)	1000	1000§	1000§
Crustal density (ρ_c) (kg/m^3)	2750	-	-
Mantle density (ρ_m) (kg/m^3)	3200	3200	3300*
Depth to top of the plate (z_1) (m)#	7000	-	-
Crust-Mantle boundary depth (z_2) (m)#	12000	-	-
Load magnitude (Q_0) (N/m)	$1.16\text{x}10^{13}$	-	-

Output result	Value	Levitt and Sandwell (1995) *	Bry and White (2007) †
Flexural parameter (α) (km)	84.23	31.7 – 110.6	18.41 – 94.79
Flexural bulge position (x_b) (km)	198.46	-	-
Zero crossing (x_0) (km)	132.31	-	-
Maximum flexural amplitude (w_{max}) (km)	5.98	-	-
Elastic thickness (km)	33.91	24.3 – 51.9	4.5 – 40

Note: Results of Levitt and Sandwell (1995) and Bry and White (2007) Aleutian Trench models shown for comparison. Dashes indicate parameters/results not given in those papers.

* Flexural rigidity range for Aleutian trench is calculated based on the average density contrast (2200 kg/m^3) and minimum and maximum values of the flexural parameter from the Levitt and Sandwell (1995) paper.

†Infill density calculated from the average density contrast and mantle density.

§Flexural rigidity and flexural parameter range calculated based on the range of elastic thickness of the Aleutian plate and given Young's modulus ($8\text{x}10^{10}$ N/m^2) and Poisson's ratio (0.25) values.

#z_1 and z_2 indicate depths below sea level datum prior to flexural bending.

REFERNCES IN CHAPTER 2

Banks, R.J., Parker, R.L., & Huestis, S., (1977). Isostatic compensation on a continental scale. Local versus regional mechanisms. *Geophysical Journal of the Royal Astronomical Society, 51*, 545-550.

Bodine, J.H., Steckler, M.S., & Watts, A.B., (1981). Observations of flexure & the rheology of the oceanic lithosphere. *Journal of Geophysical Research, 86*, 3695-3707.

Brotchie, J.F., & Silvester, R., (1969). On crustal flexure. *Journal of Geophysical Research, 74*, 5240 – 5252.

Bry, M., & White, N., (2007). Reappraising elastic thickness variation at oceanic trenches. *Journal of Geophysical Research, 112*, B08414.

Caldwell, J.G., Haxby, W.F., Karig, D.E., & Turcotte, D.L., (1976). On the applicability of a universal elastic trench profile. *Earth & Planetary Science Letters, 31*, 239-246.

Chase, C.G., & Wallace, T.C., (1988). Flexural isostasy & uplift of Sierra Nevada of California. *Journal of Geophysical Research, 93*, 2795-2802.

Crosby, A.G., & McKenzie, D., (2009). An analysis of young ocean depth, gravity & global residual topography. *Geophysical Journal International, 178*, 1198-1219.

Dahlen, F.A., (1981). Isostasy & ambient state of stress in the oceanic lithosphere. *Journal of Geophysical Research, 86*, 7801-7807.

Djomani, Y.H., Nnange, J.M., Diament, M., Ebinger, C.J., & Fairhead, J.D., (1995). Effective Te & crustal thickness variations in west central Africa inferred from gravity data. *Journal of Geophysical Research, 100*, 22047–22070.

Flemings, B., & Jordan, T.E., (1989). A synthetic stratigraphic model of foreland basin development. *Journal of Geophysical Research, 94*, 3851-3866.

Flück, P., Hyndman, R.D., & Lowe, C., (2003). Effective elastic thickness Te of the lithosphere in western Canada. *Journal of Geophysical Research, 108*, 2430.

Forsyth, D.W., (1985). Subsurface loading & estimates of the flexural rigidity of continental lithosphere. *Journal of Geophysical Research, 90*, 12623-12632.

Henrys, S.A., Wilson, T.J., Fielding, C.R., Hall, J. & Naish, T.R. (2007). Tectonic history of mid-Miocene to present southern Victoria Land Basin, inferred from seismic stratigraphy in McMurdo Sound, Antarctica. In A.K. Cooper, P.J., Barrett, H. Stagg, B. Storey, E. Stump, W. Wise (Eds.), *Antarctica: A Keystone in a Changing World. Proceedings of the 10th*

International Symposium on Antarctic Earth Sciences. Washington, DC: The National Academies Press.

Hertz, H., (1884). On the equilibrium of floating elastic plates. *Wiedemann's Annals, 22*, 449–455.

Karner, G.D., & Watts, A.B., (1983). Gravity anomalies & flexure of lithosphere at the mountain ranges. *Journal of Geophysical Research, 88*, 10449-10477.

Levitt, D.A. & Sandwell, D.T., (1995). Lithospheric bending at subduction zones based on depth soundings & satellite gravity. *Journal of Geophysical Research, 100*, 379-400.

Lowry, A.R. & Smith, R.B., (1994). Flexural rigidity of the Basin & Range-Colorado Plateau-Rocky Mountain transition from coherence analysis of gravity & topography. *Journal of Geophysical Research, 99*, 120-123.

Macario, A., Malinverno, A., Haxby, W. F., (1995). On the robustness of elastic thickness estimates obtained using the coherence method. *Journal of Geophysical Research, 100*, 15163-115172.

McKenzie, D., (2003). Estimating Te in the presence of internal loads. *Journal of Geophysical Research, 108*, doi.10.1029/2002JB001766.

McKenzie, D., & Bowin, C.O., (1976). The relationship between bathymetry & gravity in the Atlantic Ocean. *Journal of Geophysical Research, 81*, 1903-1915.

McKenzie, D., & Fairhead, D., (1997). Estimates of the effective elastic thickness of the continental lithosphere from the bouguer & free air gravity anomalies. *Journal of Geophysical Research, 102*, 27523-27552.

McNutt, M.K., & Menard, H.W., (1982). Constraints on yield strength in the oceanic lithosphere derived from observations of flexure. *Geophysical Journal of Royal Astronomical Society, 71*, 363-394.

McNutt, M.K., Diament, M., & Kogan, M.G., (1988). Variations of elastic plate thickness at continental thrust belts. *Journal of Geophysical Research, 93*, 8825–8838.

Nadai, A., (1963). *Theory of flow & fracture of solids*, New York, McGraw-Hill.

Parker, R.L., (1973). The rapid calculation of potential anomalies. *Geophysical Journal of the Royal Astronomical Society, 31*, 447–455.

Petit, C., & Ebinger, C., (2000). Flexure & mechanical behavior of cratonic lithosphere: Gravity models of the East African & Baikal rifts. *Journal of Geophysical Research, 105*, 19151–19162.

Stern, T.A., & ten Brink, U.S., (1989). Flexural uplift of the Transantarctic Mountains. *Journal of*

Geophysical Research, 94, 10315–10330.

Stern, T.A., Baxter, A.K., & Baxter, J., (2005). Isostatic rebound due to glacial erosion within the Transantarctic Mountains. *Geology, 33*, 221-224.

ten Brink, U.S., Hackney, R.I., Bannister, S., Stern, T.A., & Makovsky, Y., (1997). Uplift of the Transantarctic Mountains & the bedrock under the East Antarctica. *Journal of Geophysical Research, 102*, 27603-27621.

Turcotte, D. L., (1979). Flexure. *Advances in Geophysics, 21*, 51-86.

Turcotte, D.L., & Schubert, G., (2002). *Geodynamics*, New York, Cambridge University Press.

Walcott, R.I., (1970). Flexural rigidity, thickness & viscosity of the lithosphere. *Journal of Geophysical Research, 75*, 3941-3953.

Watts, A.B., & Burov, E.B, (2003). Lithospheric strength & its relationship to the elastic & seismogenic thickness. *Earth & Planetary Science Letters, 213*, 113-131.

Watts, A. B., Bodine, J.H., & Steckler, M.S., (1980). Observation of flexure & the state of stress in oceanic lithosphere. *Journal of Geophysical Research, 85*, 6369-6376.

Watts, A.B., Karner, G.D., & Steckler, M.S., (1982). Lithospheric flexure & the evolution of sedimentary basins. In S. Kent, M.H. Bott, D. McKenzie, & C.A. Williams (Eds.), *The evolution of sedimentary basins. Philosophical Transactions of the Royal Society of London,* 305A, 249-281.

Watts, A.B., (1978). An analysis of isostasy in the world's oceans. Part 1. Hawaiian-Emperor sea mount chain. *Journal of Geophysical Research, 89*, 5989-6004.

Watts, A.B., (2001). *Isostasy & Flexure of the Lithosphere*, Cambridge University Press, Cambridge.

Wessel, J.K., & Karner, G.D., (1989). Flexural uplift of rift flanks due to mechanical unloading of the lithosphere during extension. *Journal of Geophysical Research, 94*, 13919-13950.

Wickert, A.D., (2016). Open-source modular solutions for flexural isostasy: gFlex v1.0. *Geoscientific Model Development, 9*, 997-1017.

CHAPTER 3
Flexural subsidence around Ross Island, West Antarctica[2]

3.1 Introduction

Ross Island is a Late Neogene volcanic complex located in the Ross Sea of West Antarctica (Figure 3.1). Ross Island is located near the modern seaward edge of the Ross Ice Shelf and is comprised of the active Mt. Erebus volcano and the surrounding older Mt. Terror, Mt. Bird and Hut Point Peninsula (HPP) eruptive centers. These four volcanoes have been erupting intermittently since ca. 4.6 Ma (Kyle, 1990). Volcanic loading of the lithosphere is estimated to have resulted in the formation of a ~1.8 km deep flexural moat and ~100 m high flexural bulge around the island (Stern et al., 1991). Seismic reflection data and cores obtained from drilling in the Victoria Land Basin (VLB), Ross Sea and on the northern Ross Ice Shelf show that the middle Miocene and younger sedimentary strata in the region surrounding the moat are comprised of volcaniclastic, glaciomarine and marine sediments and sedimentary rocks (Krissek et al., 2007; Naish et al., 2007a, 2007b; Wilson et al., 2007). Sedimentary units visible on seismic reflection data show several distinct episodes of flexural subsidence within the moat, which have been correlated to eruptive events on Ross Island (Horgan et al., 2005; Fielding et al, 2008; Wenman et al., in review).

In this paper, we use isopach maps of four intervals of middle Miocene and younger strata (Wenman et al., in review) to develop flexural models for subsidence associated with each of the four episodes of volcanism on Ross Island. These flexural models are used to 1) determine the flexural rigidity of the lithosphere beneath Ross Island and whether and how it varies spatially and

[2.] Manuscript in preparation for submission to Geochemistry, Geophysics, Geosystems.

with time over the past 4.6 Ma, and 2) to determine if and how the load responsible for development of the flexural basin is partitioned between the surface (relief) and subsurface (e.g., density anomalies in the crust and/or mantle).

3.2 Tectonic setting and volcanism in the Ross Island region

Ross Island is a part of the Erebus Volcanic Province (Kyle, 1990), and is located in the Ross Sea near the western edge of the West Antarctic rift system (WARS). The WARS is a low-lying region underlying most of the West Antarctic tectonic and geomorphic domain (Behrendt, 1999; Behrendt et al., 1991). The rift is bound on its west side by the Transantarctic Mountains and on its east by Marie Byrd Land (Figure 3.2). The WARS encompasses the Ross Sea, which is an approximately 1200 km wide embayment where roughly N-S striking sedimentary basins and basement highs provide a record of extension and crustal thinning during the Late Cretaceous and Paleogene (Cooper et al., 1987; Cooper et al., 1991; Davey & Brancolini, 1995; Decesari et al., 2007; Hinz & Block, 1983; Siddoway, 2007).

The width of the region affected by extension in the WARS ranges from 750 to 1000 km, which is comparable to the Basin and Range and the East African rift systems (Behrendt et al., 1991; Busetti et al., 1999; Cooper & Davey, 1985; Brancolini et al., 1995; Henrys et al., 2007; Naish et al., 2008). Rifting began in the Late Cretaceous Period and became progressively more focused toward the flanks of the rift during the Paleogene Period (Hinz & Block, 1983; Cooper et al., 1991; Davey & Brancolini, 1995; Siddoway et al., 2004; Decesari et al., 2007; Siddoway, 2007; Wilson & Luyendyk, 2009). By late Oligocene time, extension had ceased within the central Ross Sea and became concentrated in the VLB region on the western flank of the rift (Figure 3.2), and in the Bentley Subglacial Trough adjacent to Marie Byrd Land on the eastern flank (Chaput et al., 2014; Lloyd et al., 2015). Neogene extension in the VLB has continued, possibly intermittently,

since Oligocene time at least into the Quaternary Period (Cooper and Davey, 1985; Davey et al., 2006; Fielding, 2018; Fielding et al., 2008; Paulsen et al., 2014).

Extension on the western flank of the rift was accompanied by emplacement of the Cenozoic McMurdo Volcanic Group and the Meander Intrusive Group (Armstrong, 1978; Kyle, 1990; Kyle & Cole, 1974; Tonarini et al., 1997). These two groups consist of Eocene through Recent igneous rocks extending discontinuously from Cape Adare at the north end of Victoria Land to Black and White Islands, which lie about 30 km to the south of Ross Island. The McMurdo Volcanic group is subdivided into the Hallett, Melbourne and Erebus Volcanic provinces based on geographic location (Kyle, 1990; Kyle & Cole, 1974). The Erebus volcanic province includes Ross Island, which is comprised of the Mt. Erebus (1.31 Ma to present), Mt. Terror (1.75 Ma - 0.82 Ma), Mt. Bird (4.62 Ma - 3.08 Ma), and HPP eruptive centers (1.34 Ma- 0.44 Ma). South of Ross Island, and also part of the Erebus Volcanic Province, are Mt. Discovery (5.44 Ma - 1.87 Ma), Mt. Morning (18.7 Ma - 11.4 Ma), Black Island (10.19 Ma - 1.69 Ma), White Island (7.65 Ma - 0.17 Ma), Minna Bluff (12 Ma - 4 Ma) and Brown Peninsula (2.77 Ma - 2.16 Ma) (Armstrong, 1978; Cooper et al., 2007; Esser et al., 2004; Kyle, 1981a; b; 1990; Kyle & Cole, 1974; Wilch et al., 2011; Wright and Kyle, 1990a; b; c; d). North of Ross Island, the Erebus Volcanic Province encompasses Beaufort and Franklin Islands (6.80-1.94 Ma and 3.70-0.09 Ma, respectively) and several seamounts ranging from 3.96 to 0.12 Ma in age (Rilling et al., 2007; Rilling et al., 2009). The composition and morphology of these volcanoes include basaltic shields, composite central volcanoes of basanitic to phonolitic composition, and smaller volcanoes comprised of coalesced basaltic and silicic cones (Kyle, 1990).

Several causes for rift-related magmatism in Western Antarctica have been suggested, including small scale convection on the flanks of the WARS (Armienti and Perinelli, 2010),

decompression melting of rising mantle plumes (Behrendt et al., 1997; Esser et al., 2004; Hole & LeMasurier, 1994; LeMasurier & Landis, 1996; Storey et al., 1999), and decompression melting of metasomatized lithosphere or remnant enriched domains in the asthenosphere (e.g., fossil plumes, subducted slab pieces, hydrous domains, or mafic intrusions in the lithosphere) (Cooper et al., 2007; Finn et al., 2005; Molzahn et al., 1996; Nardini et al., 2009; Perinelli, 2006; Rocchi et al., 2005; Rocchi et al., 2002; Weaver et al., 1994; Worner, 1999). Surface wave and seismic tomography images show upper mantle low velocity features beneath Marie Byrd Land and Ross Island (Emry et al., 2015; Graw et al., 2016; Hansen et al., 2014; Heeszel et al., 2016; Shen et al., 2018; White-Gaynor et al., 2019) that are consistent with plume hypotheses and with the geochemical compositions of the rocks in these areas. But the tomography also reveals a heterogeneous mantle velocity structure throughout the WARS, which may be interpreted to support petrogenetic models invoking either a compositionally or thermally heterogeneous mantle source region rather than a plume (Hansen et al., 2014; White-Gaynor et al., 2019).

3.3 Seismic stratigraphy of the Ross Island flexural moat

The seismic stratigraphy of the area lying to the north, southeast, and west of Ross Island is well studied (e.g., Cooper et al., 1995; Horgan et al., 2005; Fielding et al., 2008; Fielding, 2018; Wenman et al., in review). Fielding et al. (2008) and Fielding (2018) identified several basin-wide unconformities in the VLB (with corresponding seismic reflectors named R_a through R_k, from deepest to shallowest) and used them to develop a multi-phase subsidence model of the basin since the Late Eocene Period. They identified Oligocene early and main rift phases (encompassing strata between unconformities R_a and R_e), a late Oligocene through middle Miocene passive thermal subsidence phase (between unconformities R_e and R_g), and a middle Miocene and younger Terror Rift phase of subsidence (strata above unconformity R_g). Fielding and co-authors correlated their

R_h horizon (~7.6 Ma) with the onset of volcanism around White Island, and their R_k horizon (~1.8 Ma) with the onset of volcanism on Ross Island. However, Wenman et al. (in review) noted that the onset of volcanism on Mt. Bird (4.6 Ma) predates the estimated age of unconformity R_k, and correlates more closely with the age of horizon R_i (4.0-4.6 Ma) (Table 3.1).

Wenman et al. (in review) mapped the strata within the Ross Island flexural moat in greater detail than previous studies, identifying three local unconformities (named RMU1, RMU2, and RMU3) that are confined to within the flexural basin around Ross Island (Figure 3.3, Table 3.1). Seismic reflection data show RMU1 and RMU2 to lie between unconformities R_i and R_k of Fielding et al. (2008), and RMU3 lies between R_k and the seafloor. The RMU series of unconformities, together with R_i, R_k, and the seafloor, bound stratigraphic packages that thicken toward Ross Island and thin below seismic resolution on the flank of the flexural bulge. Wenman et al. interpreted each of these packages to have been deposited during separate periods of flexural subsidence associated with distinct phases of volcanism on Ross Island. Based on the proximity of the thickest depocenters to Bird Peninsula on Ross Island, they interpreted the lowermost two intervals, R_i to RMU1 and RMU1 to RMU2, to contain strata deposited during flexural subsidence associated with volcanism on Mt. Bird between ~ 4.6 to 3.0 Ma and 3.0 to ~2.5 Ma, respectively (Table 3.1). The interval between horizons RMU2 and R_k was interpreted to correspond to a period when subsidence was dominated by flexure due to volcanism at Mt. Terror, and to range from 2.5 to ca. 1.8 Ma in age. The interval between horizons R_k and RMU3 shows the thickest depocenter west of HPP and a smaller depocenter west of Ross Island, adjacent to the Mt. Erebus coast. Wenman et al. interpreted subsidence in this interval to be dominated by volcanism at HPP and incipient volcanism at Mt. Erebus between ~1.8 to 0.5 Ma (Table 3.1). The final stratigraphic interval, from horizon RMU3 to the seafloor, is dominated by subsidence on the west side of Ross

Island, which is interpreted to be due to flexure associated with Mt. Erebus volcanism. Importantly, subsidence related to extension is superimposed upon flexural subsidence during each of these time intervals. Thus, although each interval is dominated by depocenters closest to the relevant active volcano, the deposition was occurring contemporaneously throughout other parts of the basin as a result of extensional subsidence.

3.4 Previous Flexure studies

Several quantitative and qualitative flexure models have been proposed that fit the observed regional seismic reflection, gravity, stratigraphic, and chronostratigraphic data. Stern et al. (1991) used a two-dimensional broken elastic plate model and found that a flexural rigidity of 10^{23} N-m and line load with magnitude 1.6 x 10^{12} N/m aligned through the center of Ross Island fits the seismic, free-air gravity and bathymetric data on the southeast side of the island. ten Brink et al. (1997) inferred a much lower flexural rigidity (10^{21} N-m) using the interpolated depth to the 450 °C isotherm as a proxy for the elastic plate thickness. Their model suggested a maximum flexural subsidence underneath Ross Island of 4 km and a flexural moat extending approximately 50-70 km to the west, north, and east of the island. Neither of these studies considered time-progressive loading of the lithosphere, instead of treating the entire Ross Island volcanic load as a composite load emplaced during a single event. Aitken et al. (2012) considered progressive development of accommodation space through time (resulting from age-progressive volcanism on Ross Island) using a 3-D continuous elastic plate model constrained by seismic and gravity data, obtaining an elastic thickness of the lithosphere in the range of 2-5 km. This corresponds to a flexural rigidity D = 6 x 10^{19} to 9 x 10^{20} N-m, assuming Young's modulus of 10^{11} N/m^2 and Poisson's Ratio of 0.25). Chen (2015) also used a 3-D elastic plate model, constrained by seismic reflection geometries, estimating the elastic thickness beneath Ross Island to be 4-5 km (D = 4 x

10^{20} to 8 x 10^{20} N-m). Ji et al., (2017) modeled the elastic thickness of the western Ross Sea and along the TAM front using gravity and topographic data and a 3-D continuous elastic plate with a spatially distributed topographic load, finding an elastic thickness in the region of <5-7 km (D = 0.8 to 2.2 x 10^{21} N-m).

3.5 Method

3.5.1 Flexural model

The seismic stratigraphic studies (section 3.3, Figure 3.3) show that, in composite, the depocenters on the west, north, and southeast sides of Ross Island form a discontinuous semi-circular sedimentary moat surrounding the island. Accordingly, we model subsidence around the island using an axisymmetric solution to the elastic plate equation:

$$D\left(\frac{d^2}{dr^2}+\frac{1}{r}\frac{d}{dr}\right)^2 w(r)+\Delta\rho g w(r)=Q(r) \tag{3.1}$$

where r is radial distance, w is the magnitude of the flexural deflection, $\Delta\rho$ is the density contrast between the mantle and sedimentary strata filling the basin, g is gravity, Q is the load magnitude and D is flexural rigidity (Turcotte, 1979; Turcotte & Schubert, 2014). The model assumes that the lithosphere behaves as a continuous (unbroken) elastic plate supported by buoyant isostatic forces at its base and subjected to a vertical load $Q(r)$. In this study, we approximate the vertical load for each volcanic center as a point load of magnitude Q_0 located at position $r = R_Q$. The solution to Equation 3.1 for a point load is

$$w\left(r-R_Q\right)=Q_0\frac{\alpha^2}{2\pi D}kei\frac{r-R_Q}{\alpha} \tag{3.2}$$

where α is the flexural parameter:

$$\alpha=\left[\frac{D}{\Delta\rho+\frac{ET_e}{R^2}}\right]^{1/4} \tag{3.3}$$

Here,

$$T_e = \sqrt[3]{\frac{12D(1-\upsilon^2)}{E}} \quad (3.4)$$

and E is young's modulus, R is Earth's radius, v is Poisson's ratio, and T_e is the elastic thickness (Brotchie & Sylvester, 1969). Flexural rigidity (D) controls the wavelength of flexural deformation, and load magnitude (Q_0) and rigidity together control the depth of the flexural basin (Figure 3.4).

The likelihood of the presence of hot lithosphere under Ross Island led Aitken et al. (2012) to assume a somewhat lower density (3260 kg/m^3) than typical values for mantle (ρ_{mantle}), which has been used in this study. The density of infill material (ρ_{infill}) in the southern VLB varies from 1709 kg/m^3 to 2357 kg/m^3 in the AND-1B core, and 2107 kg/m^3 to 2415 kg/m^3 in the AND-2A core (Niessen et al., 2013; Dunbar et al., 2009). Consequently, the average density of the infill was taken to be 2200 kg/m^3, leading to a density contrast (Equations 3.1 and 3.3) of $\Delta\rho$ = 1060 kg/m^3. We used the software TAFI (Jha et al., 2017) to create the flexure models. TAFI allows users to interactively adjust the modeled flexure curves to fit constraining data (in this study, decompacted isopach thickness derived from seismic reflection data) by revising the model parameters D and Q_0. Experimentation showed that the isopach data used in this study provide poor constraints on the load location R_Q. Consequently, the load position was assumed to coincide with the volcano position in all models (R_Q=0 in Equation 3.2).

3.5.2 Isopach Decompaction

The isopach thicknesses determined by Wenman et al. (in review) for strata above reflector R_i were decompacted to correct for burial to determine the shape of the basin at the time each stratigraphic interval was deposited. A linear porosity vs. depth function was used based on the downhole porosity data obtained from the AND-1B and AND-2A boreholes (Figure 3.5):

$$\varphi_c = \varphi_0 + mZ \tag{3.5}$$

where φ_c is the compacted porosity at depth Z, and φ_0 is the porosity at the seafloor. The mean of the values obtained from the AND-1B and AND-2A borehole data were used for m (-0.0002286) and φ_0 (0.4549). Assuming that porosity loss with depth is due only to compaction, the uncompacted layer thickness (T_u) can be determined from the compacted layer thickness (T_c) and the average porosity of the compacted layer (φ_c) (Appendix A2):

$$T_u(x,y) = \frac{1}{m}\left[(\varphi_0 - 1) + \sqrt{(1-\varphi_0)^2 + 2m((1-\varphi_c(x,y))\,T_c(x,y)}\right] \tag{3.6}$$

The average porosity of the compacted layer at a given position x and y is equal to the porosity at the layer's average depth at that position (a result of the linear porosity-depth function) and is calculated from Equation 3.5. Using the above method, the R_i-RMU2 strata was decompacted on average by ~33%, RMU2-R_k by 15.5% and R_k-RMU3 by 6.4%.

3.5.3 Modeling Strategy

We use the decompacted isopach maps discussed above to constrain the pattern of flexural subsidence around Ross Island during the periods when each of the major volcanic centers on the island was active. Isopach thicknesses for the R_i to RMU1 and RMU1 to RMU2 intervals were combined because both intervals were interpreted by Wenman et al. (in review) to represent subsidence due primarily to loading on Mt. Bird (Figure 3.6a). Following Wenman et al., we use the interval between RMU2 and R_k to constrain flexural subsidence associated with volcanism on Mt. Terror (Figure 3.6b), the interval between R_k and RMU3 to constrain flexure due to volcanism on HPP (Figure 3.6c), and the interval RMU3 to the seafloor to constrain flexure due to loading on Mt. Erebus (Figure 3.6d).

Flexure models were developed independently for each of the four volcanic episodes on Ross Island (Mt. Bird, Mt. Terror, HPP, and Mt. Erebus) by fitting subsidence curves to the decompacted thickness of the corresponding isopach interval (R_i-RMU2, RMU2-R_k, R_k-RMU3, RMU3-Seafloor, respectively). For each volcanic center, the decompacted isopach thickness was extracted from the appropriate isopach grid along a set of profiles extending radially outward from each volcanic center and trending as perpendicular as possible to the nearby isopach contours. The profiles the volcano were aligned along what was visually deemed to be the inflection point of the basin outer slope and averaged to produce a single stacked profile for each volcanic center, with the origin (r=0) chosen to coincide with the volcano position. Flexural models were developed to fit the stacked profiles to determine the best fit for each volcanic center. Models were also developed to bound the range of isopach thicknesses along each profile (the un-stacked isopach data) to ascertain the uncertainty of the model parameters. Additionally, the thickness of the entire flexural package (R_i to the seafloor) was modeled along each profile to compare the flexural rigidity and load magnitude obtained from models of net subsidence with those obtained from the incremental loading and episodic subsidence models. Wenman et al. (in review) did not construct an isopach for the R_i to seafloor (R_i-SF) interval, so this grid was created by subtracting the seafloor depth grid of Wenman et al. from their R_i horizon depth grid (Figure 3.7). We do not model the flexural deflection to the southeast and east of Ross Island due to the sparsity of seismic reflection data in that region.

3.6 Results

The elastic plate flexure model provides a reasonable fit to the long-wavelength changes in isopach thickness along each of the profiles (Figure 3.8; Table 3.2). Exceptions are the portions of the Mt. Bird and Mt. Terror profiles that are nearest to Ross Island, where the models overestimate the

isopach thickness. On the Mt. Bird profile, seismic data show that the strata in this area thins onto the flanks of Ross Island (interpreted to indicate uplift on the island coincident with deposition). This is not captured in the flexural model, and no attempt was made to fit this part of the profile. The Mt. Terror profile is interpreted similarly, although this profile is less constrained by seismic data than the Mt. Bird profile. Given the variance in the isopach thickness and excepting the portions of the Mt. Bird and Mt. Terror profiles closest to Ross Island, reasonable fits can be obtained with a range of model parameters. The uncertainties in model parameters were determined by separately and iteratively varying D and Q_0 from the best-fit model parameter values to find flexural models that bound the data along each profile (indicated by the shaded area in Figure 3.8).

3.6.1 Flexural rigidity (D)

The models show that the flexural rigidity of the lithosphere to the north of Mt. Bird was in the range of 33.2 – 63.9 x 10^{18} N-m during the time that volcano was active (during the R_i-RMU2 stratigraphic interval) (Figure 3.8a). Flexural rigidity during loading on Mt. Terror (RMU2-R_k interval) ranges from 152.9 – 457.0 x 10^{18} N-m (Figure 3.8b). We note, however, that the shape of the Mt. Terror flexural basin is not well constrained by seismic data on its eastern side (Wenman et al., in review). As Wenman et al. noted, the Mt. Terror basin may be narrower than shown on their maps, and thus the flexural rigidity for this profile may be over-estimated. Flexural rigidities to the southeast of HPP (constrained by the R_k-RMU3 isopach) and west of Mt. Erebus (constrained by RMU3-SF isopach) are lower than at either Mt. Bird or Mt. Terror, ranging from 2.7 – 7.6 x 10^{18} N-m at HPP (Figure 3.8c) and 3.7 – 20.3 x 10^{18} N-m at Mt. Erebus (Figure 3.8d). The flexural rigidity estimates above were obtained by modeling subsidence around Ross Island at different times and positions, according to when the different volcanic centers were active and

where the associated flexural depocenter was located. The total subsidence around the island that has occurred since the onset of magmatism at about 4.6 Ma is represented by the entire R_i-SF stratigraphic interval. The flexural rigidity estimated by modeling the R_i-SF isopach along the profile to the north of Mt. Bird is 747.8 x 10^{18} N-m. The flexural rigidities estimated from the same stratigraphic interval along the profiles to the north of Mt. Terror, to the southeast of HPP, and west of Mt. Erebus are 1503.8 x 10^{18} N-m, 3.6 x 10^{18} N-m, and 76.9 x 10^{18} N-m, respectively (Figure 3.9).

3.6.2 Flexural Load (Q_0)

The net load magnitude calculated by summing the loads from the best fit flexure models of the individual isopach intervals (R_i-RMU2, RMU2-R_k, R_k-RMU3 and RMU3-SF) is 7.2 x 10^{16} N, with a range (obtained by summing the respective minimum and maximum load estimates) of 2.3 - 10.8 x 10^{16} N (Table 3.2). The average load determined from the flexure models of the composite stratigraphic interval (R_i-SF) is 9.4 x 10^{16} N, with a range of 6.7 - 15.3 x 10^{16} N (Table 3.3).

For comparison, the load created by the Ross Island volcanic edifice is estimated by multiplying its volume by the average density of the rocks comprising the island (corrected for the density of the surrounding seawater or sedimentary rock for the subsea and subseafloor portions of the edifice, respectively). As noted previously, the density of the basin infill was taken to be 2200 kg/m^3. The density of rocks comprising Ross Island is taken to be 2650 kg/m^3, which is typical of basanitic and phonolitic rocks that are dominant on the island (Kyle, 1997, 1981a, 1981b; Wright & Kyle, 1990 a; b; c; d). The volume of Ross Island above the seafloor was estimated to be 4.2 x 10^{12} m^3 (1.9 x 10^{12} m^3 above sea level and 2.3 x 10^{12} m^3 below sea level) by integrating the Bedmap2 (Fretwell et al., 2013) relief grids inside the area defined by the 900 m isobath. The

900 m isobath is the deepest isobath encircling the island (with exception of the southwest side near the southern Victoria Land coast). The volume of the buried portion of Ross Island was estimated to be 7.4 x 10^{12} m^3 by assuming the island has a roughly conical shape below the seafloor. The radius of the upper face of the cone was taken to be the average radius of Ross Island at the seafloor (bound by the 900 m isobath), about 30 km. The radius of the lower face of the cone is 39 km, determined by projecting the subsea slope of the island's flanks downward to the depth of horizon R_i (which immediately predates the oldest Ross Island volcanic rocks). The height of the cone (2000 m) is taken as the mean of maximum modeled thickness (W_{max}) of the R_i to seafloor isopach interval, which ranges from 972 m to 2908 m (Table 3.3). Using these thickness ranges, the load placed on the lithosphere by Ross Island is estimated to be between 8.6 x 10^{16} N – 21.2 x 10^{16} N, with a nominal value of 14 x 10^{16} N.

3.7 Discussion

3.7.1 Impact of extension on flexural models

The flexural rigidity and load magnitude estimates obtained from the flexural models of the R_i to seafloor interval are consistently larger than those estimated by considering only the isopach interval during which each volcanic center was active (Tables 3.2 and 3.3). This suggests a bias in the models toward a deeper and wider flexural basin when the entire isopach interval is considered. The southern VLB was undergoing extension during the time when flexural subsidence around Ross Island was taking place. The R_i to seafloor interval thus includes strata deposited during periods in which subsidence was dominated by regional extension, in addition to strata deposited more locally during the periods when each flexural sub-basin was active. The flexural models fitting the entire isopach interval overestimate the flexural rigidity and load magnitude because the superposition of extensional subsidence and flexural subsidence creates a

wider and deeper basin than a basin produced primarily by volcanically induced flexure alone. We consider the flexural parameters estimated from the individual isopach intervals to be more accurate, as they represent subsidence only during the time and area in which each volcanic center was active. Although extension likely also contributed to subsidence in these areas, it is a relatively small component during the time of active volcanic loading in each sub-basin, and thus produces less bias in the models during those times.

3.7.2 Variations of lithospheric strength around Ross Island

The flexure models indicate that the strength of the lithosphere associated with Mt. Bird loading (between 4.6 to 3.1 Ma) was lower than the strength of lithosphere associated with volcanism at Mt. Terror (1.8 – 0.8 Ma), although we consider the rigidity estimate for the lithosphere north of Mt. Terror to be a maximal estimate (as discussed previously). The strength of the lithosphere near HPP and Mt. Erebus was similar when these areas were erupting (1.34 – 0.44 Ma and 1.31 Ma – present, respectively) but was weaker than to the north of either Mt Bird or Mt Terror.

Based on the above, the lithospheric strength to the north and northeast of Ross Island was higher than to its south and southwest during the times in which the various volcanoes were active. However, the flexural basins to the north and northeast are older than those to south and southeast of Ross Island. Thus, the difference between relatively high flexural rigidity north and northeast of Ross Island and lower rigidity south and southwest of the island may result from changes in rigidity either with time or position.

A spatial change in rigidity may be a result of regional temperature variations in the upper mantle. Tomography studies show relatively high upper mantle seismic velocities (interpreted to indicate relatively low temperatures) on the eastern side of the southern VLB in comparison to the

west (Lawrence et al., 2006; Watson et al., 2006; Heeszel et al., 2016; An et al, 2015; Brenn et al., 2017; Shen et al., 2018). These studies also show that the relatively low velocities in the western Victoria Land Basin extend eastward beneath Ross Island and westward toward East Antarctica and then north along the trend of the TAMS. The inferred elevated upper mantle temperatures have been attributed to post-Miocene focusing of extension along the western margin of the VLB (Shen et al., 2018). Alternatively, the low upper mantle velocities beneath Ross Island have also been attributed to a rising mantle plume with the plume head deflected westward toward East Antarctica at the base of the lithosphere (Hansen et al., 2014; Heeszel et al., 2016; White-Gaynor et al., 2019). The presence of a plume is supported by the geochemistry of Ross Island basalts, which are similar in trace element and isotopic composition to Ocean Island Basalts (Hole & LeMasurier, 1994; Weaver et al., 1994). Alternatively, the lower flexural rigidity to the west and southwest of Ross Island as compared to the north and northeast can be explained by a ruptured lithosphere. The Terror Rift trends south-southeast beneath Ross Island, leading previous authors to hypothesize a zone of weakness beneath the island (Hall et al., 2007; Cooper et al., 1991; Stern et al., 1991). Alone, faults within the buried Terror Rift would weaken the lithosphere since broken plates are weaker than continuous plates, but this would not cause one side of the fault to be weaker than the other. However, combined with a higher temperature in the western basin, such segmentation could lead to a scenario in which Ross Island straddles two half-plates with distinctly different strengths.

As noted previously, the differences in flexural rigidity on either side of Ross Island may reflect changing flexural rigidity with time rather than position, as the lower rigidity estimates are associated with the younger volcanic centers. Successive heating of the lithosphere due to repeated intrusions over the 4.6 Ma volcanic history of the island may have led to progressive weakening

of lithosphere. Continued extension in the Terror rift since the end of the Miocene Period might also have caused progressive weakening of the lithosphere over time, either as a result of lithospheric thinning (e.g., Harry et al., 2018) or by faulting as previously discussed. Faulting in the Terror Rift has been ongoing since at least middle Miocene to the present (Fielding et al., 2008; Wenman et al., in review). This continued faulting may have progressively weakened the lithosphere beneath Ross Island, such that it behaved as a continuous plate prior to the end of the Pliocene Period (when Mt. Bird and Mt. Terror were active) and as a broken plate afterward (when Hut Point Peninsula and Mt. Erebus were active).

3.7.3 Load partitioning between surface and sub-surface

The mass of Ross Island is estimated to produce a vertical load on the lithosphere ranging from 8.6 x 10^{16} N – 21.2 x 10^{16} N, with a nominal value of 14 x 10^{16} N (section 3.6.2). This range of load estimates for Ross Island mostly exceeds the range estimated for the net flexural load (2.3 – 10.8 x 10^{16} N), which is calculated by summing the minimum and maximum loads obtained from the models for each sub-basin. The nominal value of the Ross Island load is almost twice the best fitting net flexural load (7.2 x 10^{16} N), which is obtained by summing the best fitting load for each sub-basin. The models thus imply that Ross Island is either near flexural isostatic balance (if the minimum estimate for the Ross Island load is accepted) or a buoyant load of up to 7-10 x 10^{16} N is required in addition to the flexural isostatic forces to balance the weight of Ross Island (assuming the nominal or maximal values for the Ross Island load). The need for a buoyant load can be partially mitigated by assuming a higher density contrast between the mantle and basin-fill than used in the flexural models, which would increase the vertical isostatic restoring force in the model. However, parameter testing of the models shows that raising the model regional mantle density to as much as 3400 kg/m^3 density (considered to be a ceiling for realistic mantle densities) allows the

modeled flexural load to be increased by only about 10%. A more plausible cause for a buoyant force is a localized low-density anomaly in the mantle, acting locally to counter the weight of Ross Island. Dividing the requisite buoyant force by assumed minimal and maximal anomalous density contrasts of 100 kg/m^3 and 250 kg/m^3 (corresponding to densities of 3160 kg/m^3 and 3010 kg/m^3, given the nominal 3260 kg/m^3 mantle density used in the flexural models) yields a volume of 1.4 x 10^{13} to 6.9 x 10^{13} m^3, approximately equaling 1 to 5 times the estimated volume of Ross Island. The requisite density anomaly thus fits within a relatively small volume in the upper mantle, corresponding to a sphere of radius 18-25 km, or a cylinder of height 6-14 km if we assume the cylinder radius to be the same as the base of Ross Island at the depth of horizon R_i (39 km). Such a mass anomaly can be accounted for by either a local thermal or compositional anomaly in the mantle beneath the island, consistent with the previously discussed seismic velocity models.

3.7.4 Comparison to previous flexural modeling studies

Excluding the relatively weakly constrained Mt. Terror model, the flexural rigidities estimated in this paper range from 3 x 10^{18} N-m to 4 x 10^{19} N-m, which is roughly four orders of magnitude lower than the 1 x 10^{23} N-m obtained by Stern et al. (1991) and two orders of magnitudes lower than the 1 x 10^{21} N- m obtained by ten Brink et al. (1997). Stern et al. used a broken plate model, whereas a continuous plate model was used here. A broken plate is inherently weaker than an unbroken plate, thus an unbroken plate requires a smaller flexural rigidity to produce a basin of a similar wavelength to a broken plate model. ten Brink et al (1997) did not examine models with elastic thickness less than 5 km (D ~ 10^{21} N-m) and did not attempt to model the stratigraphic thickness of the Ross Moat basin. The rigidity estimates obtained here are more similar to but still lower than those obtained from the previous unbroken plate models of Aitken et al. (2012) and Chen (2015), who estimated flexural rigidities between 6 x 10^{19} N-m to 9 x 10^{20}

N-m and 4 x 10^{20} N-m to 9 x 10^{20} N-m, respectively. Both the Aitken et al. and Chen models considered time progressive loading of the lithosphere, as in this study, but they used three-dimensional loading models in order to construct a regional fit to the basin shape around Ross Island. As noted previously, this would include areas subsiding primarily as a result of extension rather than volcanic loading and would thus produce a bias toward higher flexural rigidity in comparison to the models shown here (which focus specifically on areas subsiding as a result of volcanic loading). Nonetheless, our results support the interpretation of relatively low strength lithosphere ($D < 10^{21}$ N-m) in the southern McMurdo Sound.

3.8 Summary

The sedimentary moat surrounding Ross Island is a composite of four smaller flexural sub-basins that formed at different times and positions, according to when and where each of the four main volcanic features on the island was active. Flexural models were developed to describe subsidence in the composite flexural moat since volcanism began on Ross Island ca. 4.6 Ma, and in each of the four sub-basins during the period in which the sub-basin (and corresponding volcano) was active. The models use decompacted isopach thicknesses as a proxy for subsidence during each of the time intervals of interest and treat the lithosphere as an unbroken thin elastic plate subjected to vertical point loads representing each of the volcanic centers. The models based only on incremental subsidence that occurred in each sub-basin during the time in which the corresponding volcano was active yield best fitting flexural rigidities ranging from 2.7-33.2 x 10^{18} N-m (excluding the poorly constrained Mt. Terror sub-basin). Models of the cumulative subsidence that has occurred in each sub-basin since the onset of volcanism yield generally higher flexural rigidities (except for Hut Point Peninsula), ranging from 1.5-357.6 x 10^{18} N-m. We conclude that the cumulative subsidence models are biased by inclusion of strata in each sub-basin that were

deposited during periods when the corresponding volcanic center was quiescent, and subsidence was dominated by regional extension. We thus consider the models based on the incremental subsidence that occurred during the period in which the corresponding volcano was active to be the better estimates of the strength of the lithosphere. The models show the lithosphere on the north and northeast sides of Ross Island to have been stronger than the lithosphere the south and southwest sides of the island at the time the respective volcanic centers were active. However, given that the younger volcanoes lie on the south and southeast sides of the island, it is not possible to distinguish whether this reflects spatial variations in the strength of the lithosphere or progressive weakening of the lithosphere through time.

The cumulative vertical force of the best fitting point loads (obtained by summing the modeled loads from each of the volcanic centers) is estimated to be about 7×10^{16} N. The load produced by the weight of the rocks comprising Ross Island is estimated to be approximately twice the cumulative modeled flexural load. This suggests the presence of a buoyant force in the mantle beneath the island, roughly equal to half the vertical load produced by the weight of the Ross Island volcanic edifice. The requisite buoyant force can be accounted for by a lower density anomaly (density = 3160 kg/m^3) in a small region in the upper mantle having roughly 1-5 times the volume of Ross Island.

3.9 Acknowledgments

We thank Terry Wilson for suggesting that we examine flexural subsidence around Ross Island. We also thank undergraduate students Derek Witt for his help with the initial Ross Island volume estimates and Jace Kroger for his initial findings of the density of sediments in AND-1B. This research was supported by National Science Foundation Grants ANT-1043700 and ANT-1169553 to DLH.

3.10 Figures in chapter 3

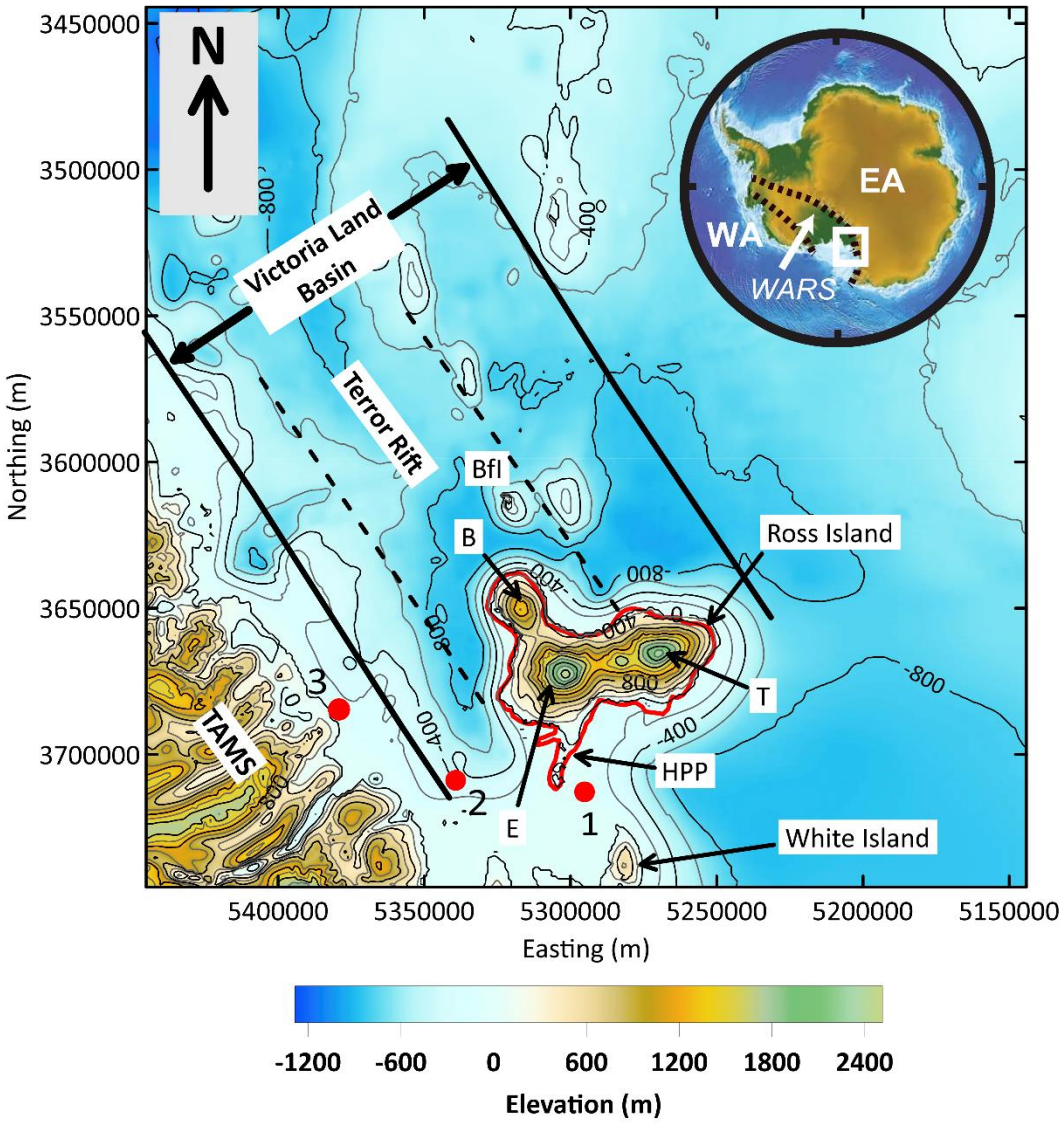

Figure 3.1. Location map of the study area. Ross Island straddles the Terror Rift in the southern Victoria Land Basin and is dominated by four volcanic centers: Mt. Erebus (E), Hut Point Peninsula (H), Mt. Terror (T) and Mt. Bird (B). Red dots denote drill holes in the region - AND-1B (1), AND-2A (2) and CIROS-1 (3). TAMS – Transantarctic Mountains; BfI - Beaufort Island. Relief from Bedmap2 [*Fretwell et al.*, 2013]. Elevations are in meters relative to sea level.

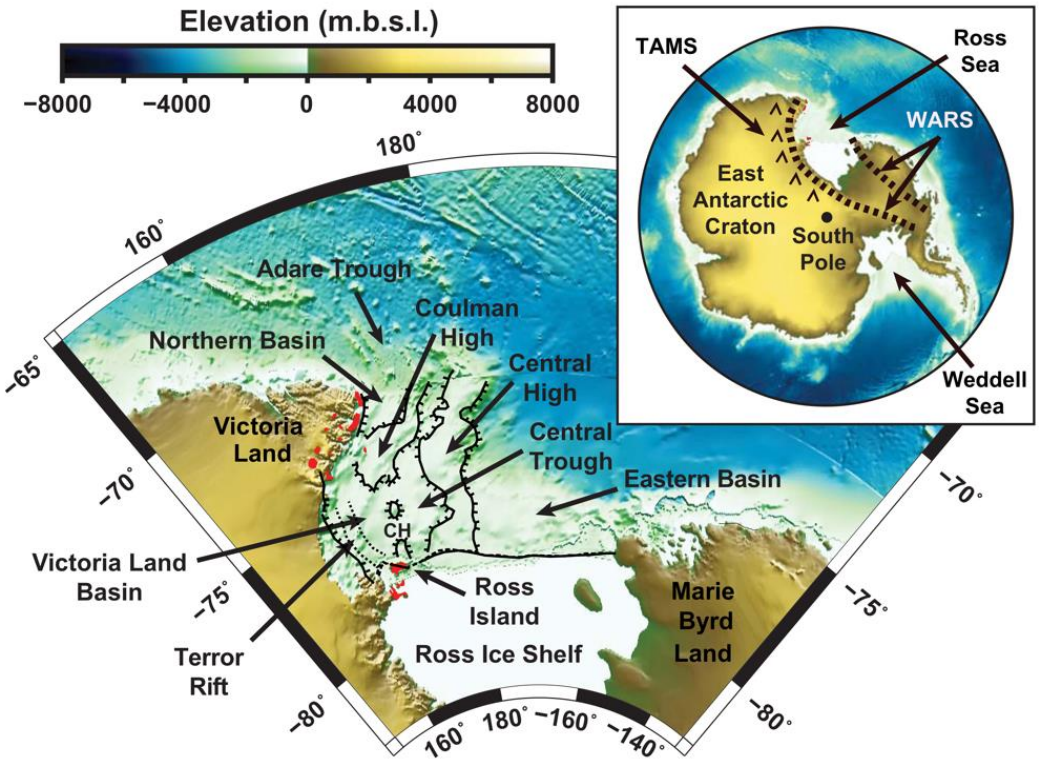

Figure 3.2. Location map of the West Antarctic Rift System (WARS) and major tectonic features north of Ross Island. Thick hatched lines – rift basin and uplift boundaries; dotted lines - boundaries of Terror Rift). Cenozoic alkaline rocks are denoted by red shading. Relief from ETOPO2 dataset (National Geodetic Data Center, 2006).

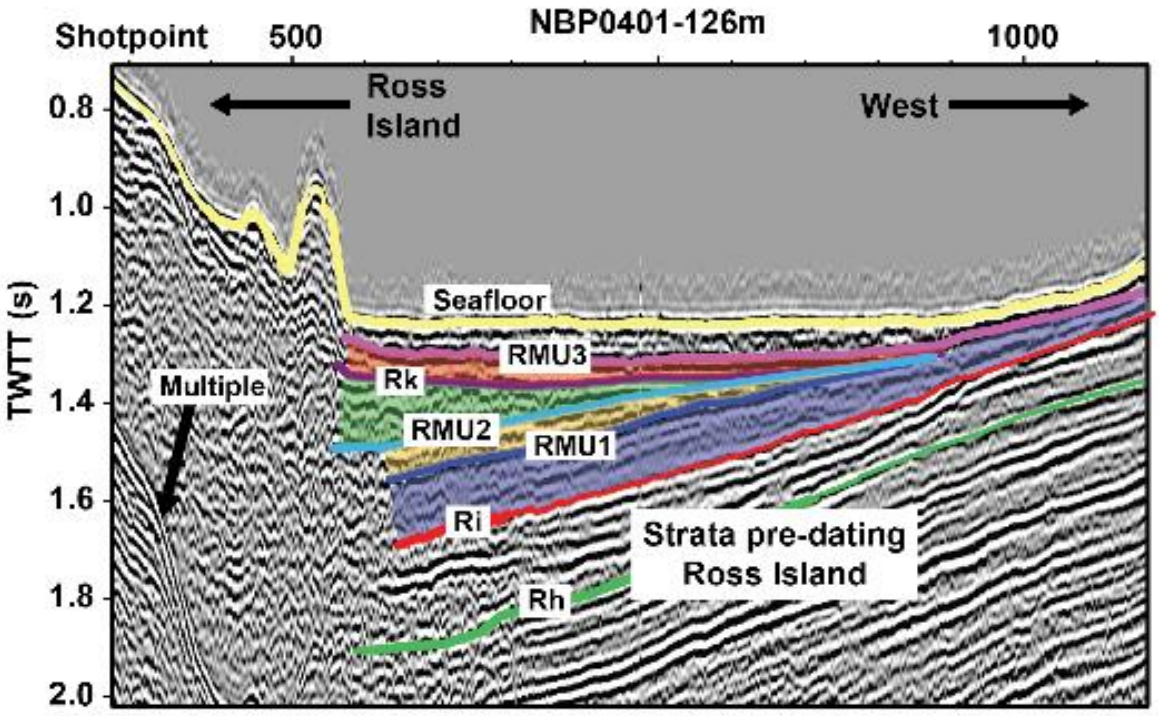

Figure 3.3. Seismic profile NBP0401-126m (source: Antarctic Seismic Data Library System), located west of Ross Island, showing unconformities discussed in the text. See Table 3.1 for unconformity ages. Unconformities bound wedge-shaped stratal packages indicated by color fill. In this paper, we have grouped the R_i-RMU1 and RMU1-RMU2 intervals into one package deposited during flexural subsidence associated with the eruption of Mt. Bird. The RMU2-R_k interval represents strata deposited during loading at Mt. Terror. The R_k-RMU3 interval corresponds with the HPP eruption phase, and the RMU3- SF interval to the period during which Mt. Erebus has been active.

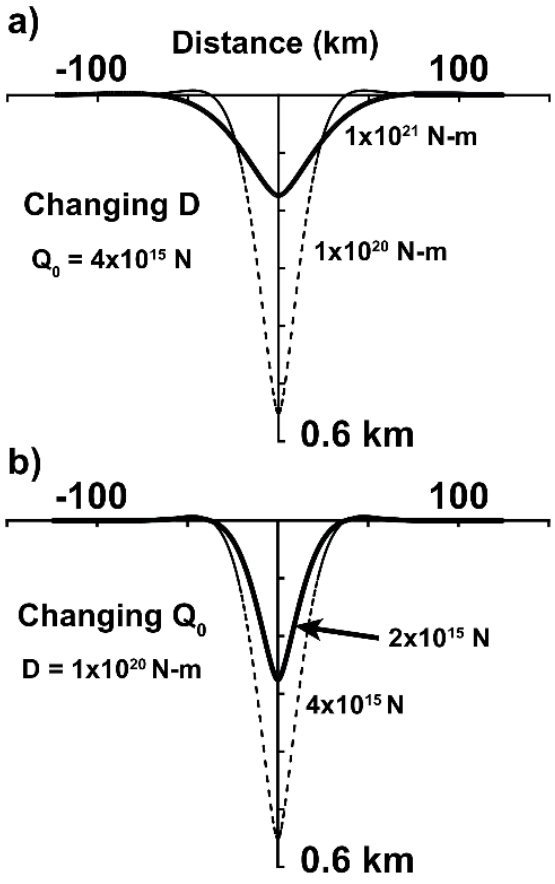

Figure 3.4. Effect of changes in model parameters on basin shape. a) Increasing flexural rigidity (D) while keeping all other parameters unchanged leads to a wider and shallower basin, b) higher load magnitude (Q_0) leads to a deeper basin when all other parameters are unchanged.

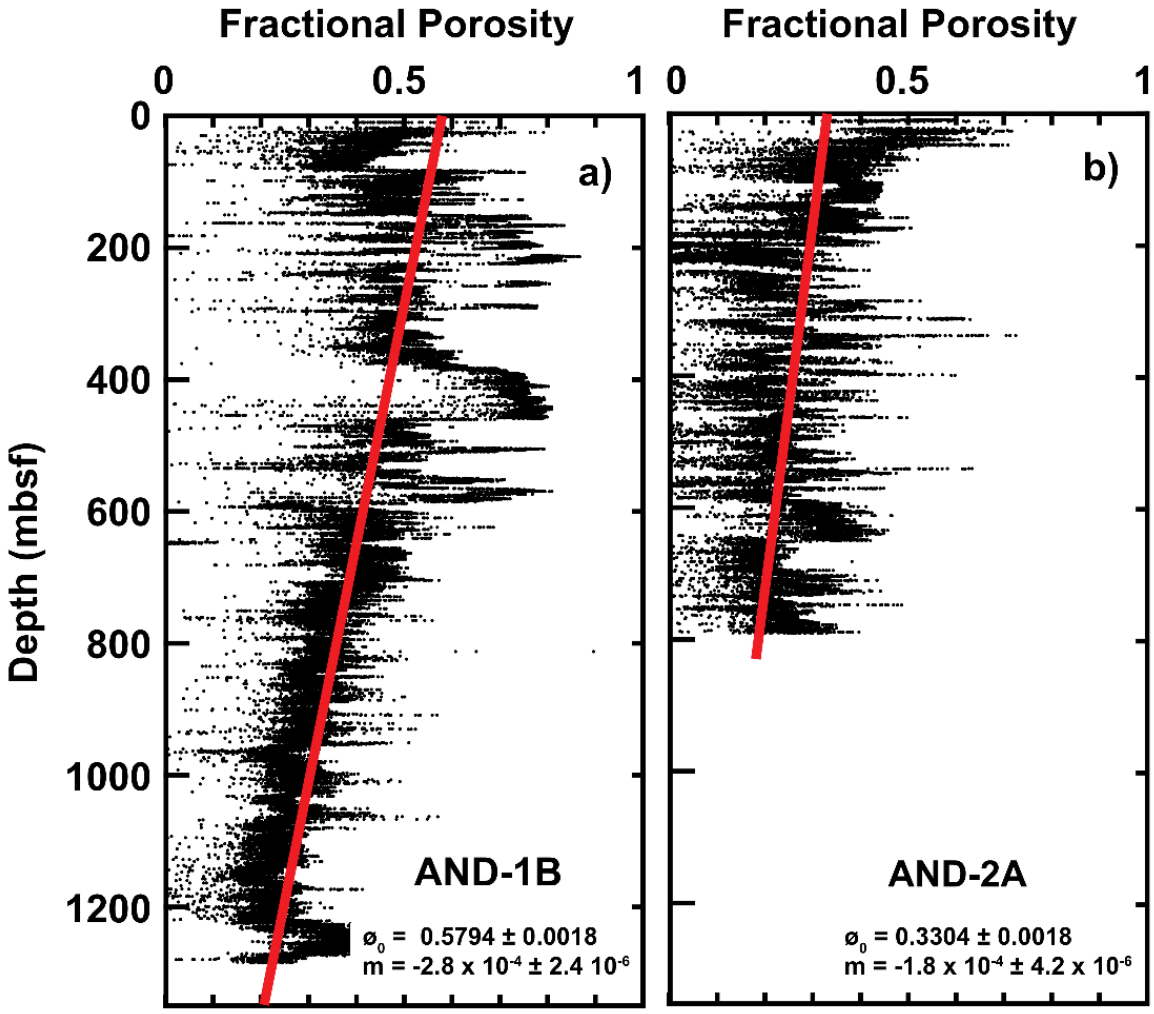

Figure 3.5. Porosity – depth data from (a) AND-1B and (b) AND-2A boreholes (Niessen et al. (2013) Dunbar et al. (2009). Red line shows the best-fitting linear trend, with curve parameters indicated in the lower right of each figure.

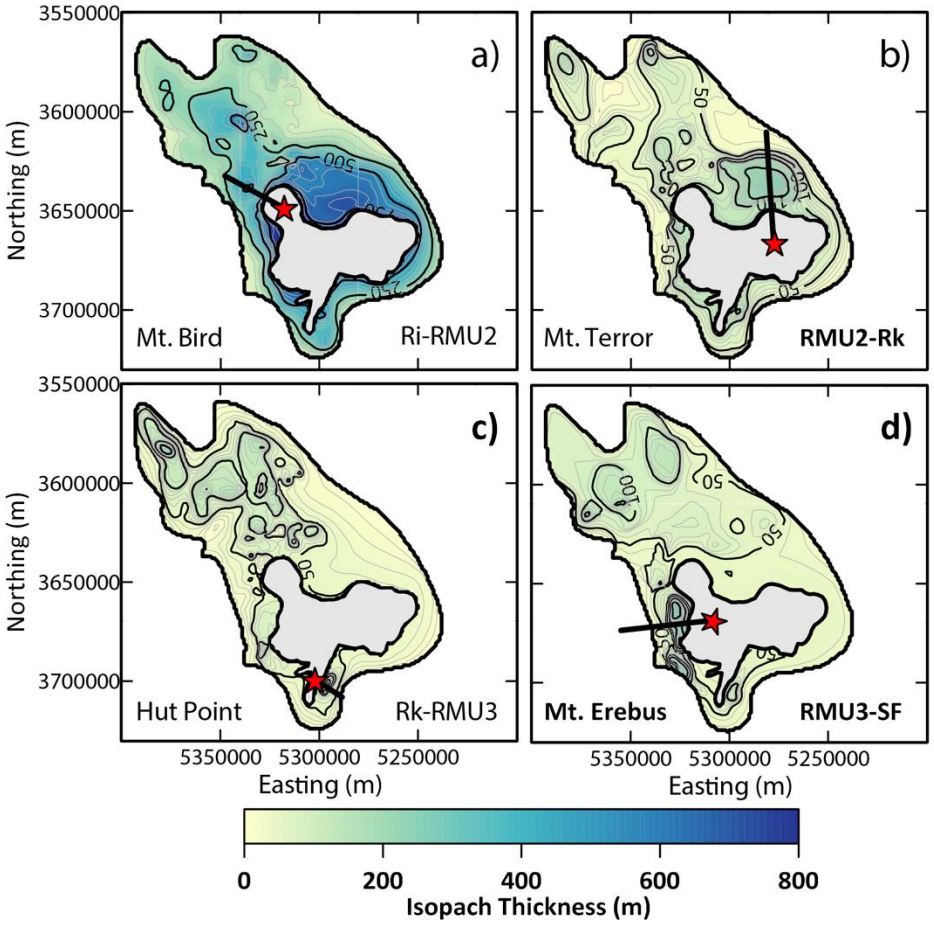

Figure 3.6. Decompacted isopach maps for stratigraphic intervals used in flexural models. a) R_i-RMU2, b) RMU2-R_k, c) R_k-RMU3 and d) RMU3-SF. Isopach thicknesses are projected onto profiles and averaged to produce a singled stacked profile (thick black lines) at times during which each of the respective volcanic centers (stars) were active - Mt. Bird (B) for R_i-RMU2, Mt. Terror (T) for RMU2-R_k, HPP (H) for R_k-RMU3, and Mt. Erebus (E) for RMU3-SF.

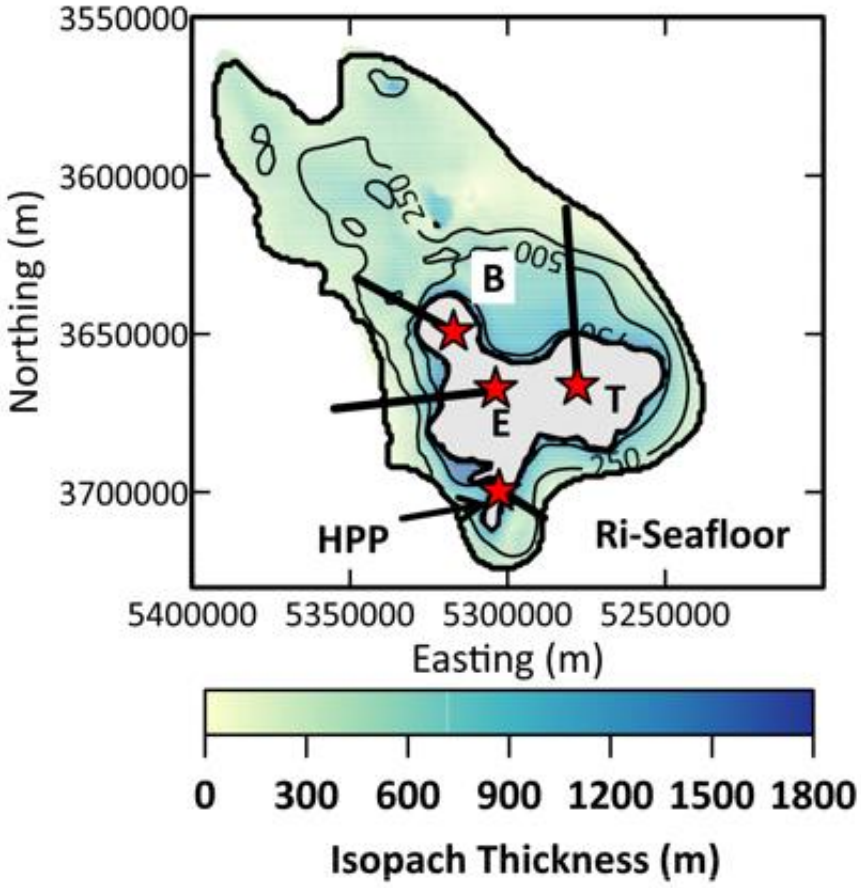

Figure 3.7. Isopach map for R_i-SF interval, representing the cumulative subsidence around Ross Island during the period of active volcanism from 4.6 Ma to present. Profiles used to model flexure of the cumulative isopach interval (black lines) are at the same as in Figure 3.6.

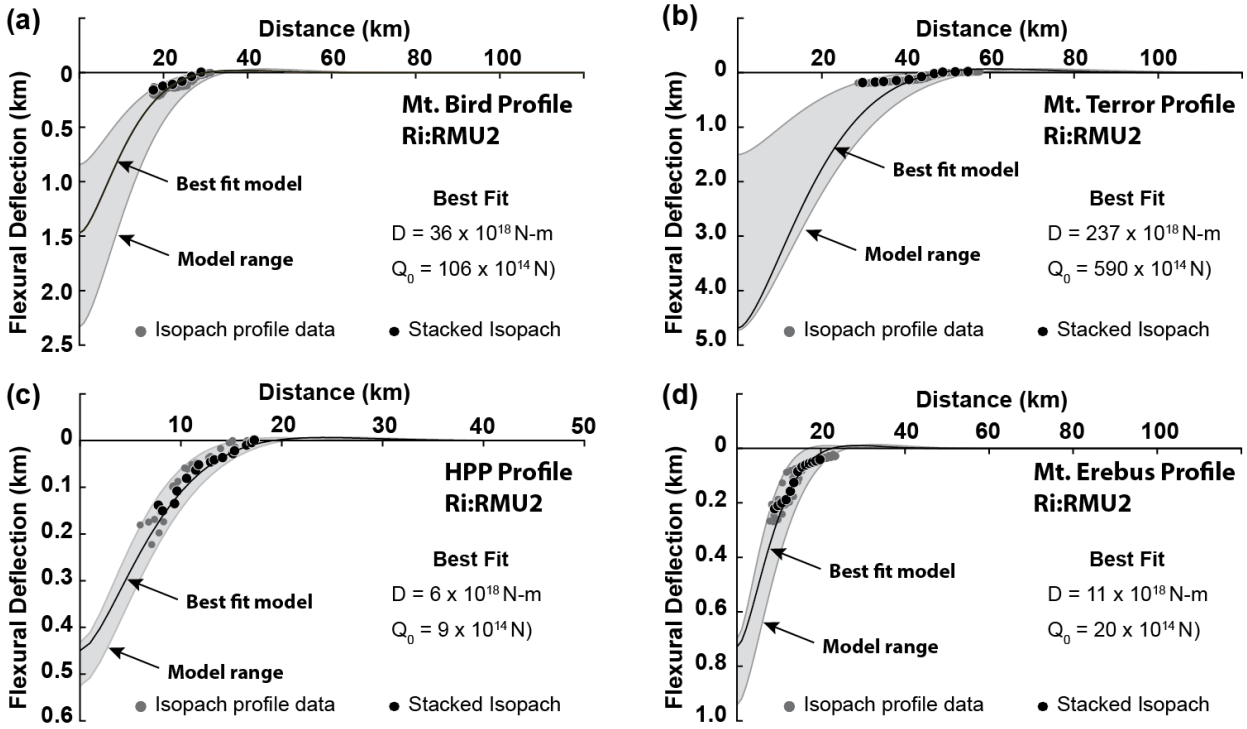

Figure 3.8. Flexural models for a) Mt. Bird, b) Mt. Terror, c) HPP and, d) Mt. Erebus. Solid line – best fit model; gray area – a region encompassing models produced with the range of parameters shown in the boxes; gray dots - isopach data projected onto profiles shown in Figure 3.6; black dots with a white outline – average (stacked) isopach profiles. D = flexural rigidity; Q_0 = point load magnitude; R_Q = load position (profile origin is at volcano location shown in Figure 3.6).

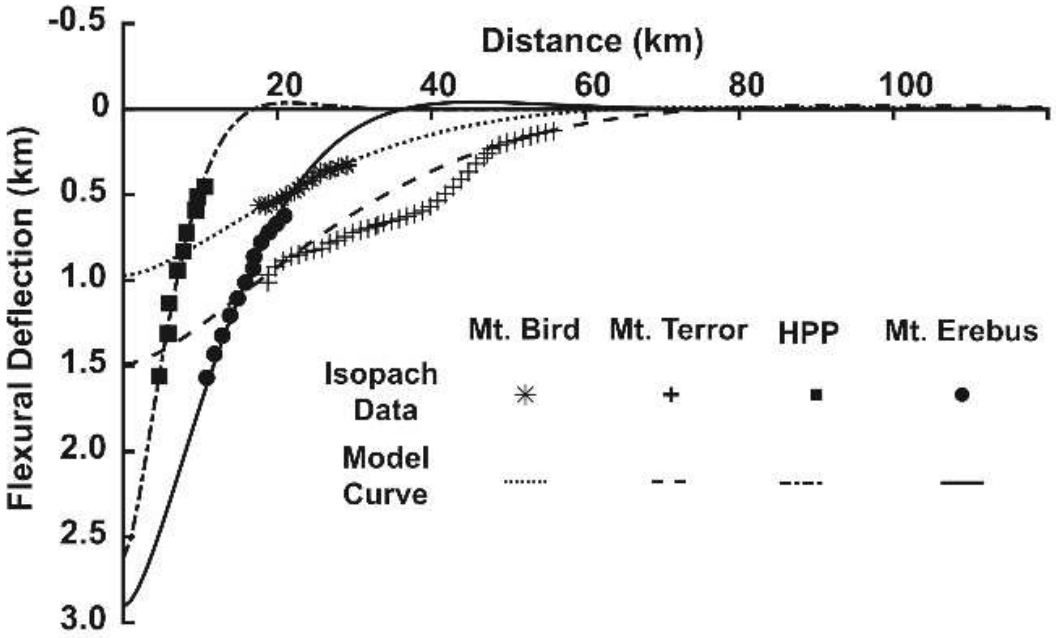

Figure 3.9. Flexural models for R_i-SF interval showing profiles for Mt. Bird, Mt. Terror, HPP and Mt. Erebus sub-basins. Symbols indicate average isopach thickness along stacked profiles shown in Figure 3.7.

3.11 Tables in chapter 3

Table 3.1: Age range for unconformities and volcanoes [a]

Feature	Age (Ma)[b]
Unconformity	
RMU3	~1
Rk	1.7 to >2.1 (1.8)
RMU2	~2.5
RMU1	~3
Ri	4.0 to 4.6 (4.3)
Volcanoes	
Mt. Bird	4.6 to 3.1
Mt. Terror	1.8 to 0.8
Hut Point Peninsula	1.34 to 0.44
Mt. Erebus	1.31 to present

[a] From Wenman et al. (in review). [b] Nominal age in parentheses.

Table 3.2: Best fit model parameters and range for individual isopach intervals

Isopach (volcano)	Flexural rigidity (D)			Load magnitude (Q_0)			Load position (R_Q)	Maximum deflection (Wmax)
	Best	Min	Max	Best	Min	Max		
	[x 10^{18} N-m]			[x 10^{14} N]			[km]	[km]
Ri-RMU2 (Mt. Bird)	36.0	33.2	63.9	105.7	61.2	209.3	0	0.9
RMU2-Rk (Mt. Terror)	237.4	151.8	457.0	589.5	151.8	825.4	0	1.5
Rk-RMU3 (HPP)	5.9	2.7	7.6	8.9	5.7	11.8	0	2.6
RMU3-SF (Mt. Erebus)	11.4	3.7	20.3	19.9	10.9	34.5	0	2.9
Cumulative Load				724.0	229.6	1080.9		

Table 3.3: Best fit model parameters and range for Ri to seafloor isopach interval

Volcano	Flexural rigidity (D)			Load magnitude (Q_0)			Load position (R_Q)	Maximum deflection (Wmax)
	Best	Min	Max	Best	Min	Max		
	[x 10^{18} N-m]			[x 10^{14} N]			[km]	[km]
Mt. Bird	747.81	357.59	1440.72	217.5	182.8	304.0	0	0.9
Mt. Terror	1503.77	881.04	3270.11	470.7	356.1	815.1	0	1.5
Hut Point	3.63	1.47	25.95	40.8	21.9	112.7	0	2.6
Mt. Erebus	76.88	14.62	218.67	208.3	112.7	295.2	0	2.9
Cumulative Load				937.2	673.4	1526.9		

REFERENCES IN CHAPTER 3

Aitken, A.R.A., Wilson, G.S., Jordan, T., Tinto, K., & Blakemore, H. (2012). Flexural controls on late Neogene basin evolution in southern McMurdo Sound, Antarctica. *Global and Planetary Change, 80-81*, 99-112, https://doi.org/10.1016/j.gloplacha.2012.02.004.

An, M., Wiens, D.A., Zhao, Y., Feng, M., Nyblade, A.A., Kanao, M., Li, Y., Maggi, A. & Lévêque, J.J. (2015). S- velocity model and inferred Moho topography beneath the Antarctic Plate from Rayleigh waves. *Journal of Geophysical Research, 120(1),* 359-383.

Armienti, P., & Perinelli, C. (2010). Cenozoic thermal evolution of lithospheric mantle in northern Victoria Land (Antarctica): Evidences from mantle xenoliths. *Tectonophysics, 486,* 28-35.

Armstrong, R.L. (1978). K-Ar dating: Late Cenozoic McMurdo Volcanic Group and dry valley glacial history, Victoria Land, Antarctica. *New Zealand Journal of Geology and Geophysics, 21(6),* 685-698.

Behrendt, J.C. (1999). Crustal and lithospheric structure of the West Antarctic Rift System from geophysical investigations – a review. *Global and Planetary Change, 23*, 25-44.

Behrendt, J.C., Blankenship, D.D., Damaske, D., Cooper, A.K., Finn, C., & Bell, R.E. (1997). Geophysical evidence for late Cenozoic subglacial volcanism beneath the West Antarctic Ice Sheet and additional speculation as to its origin. In C. A. Ricci (Eds.), *The Antarctic Region: Geological Evolution and Processes*, (pp. 539-546). Terra Antarctica, Siena.

Behrendt, J.C., LeMasurier, W.E., Cooper, A.K., Tessensohn, F., Tréhu, A., & Damaske, D. (1991). Geophysical Studies of the West Antarctic Rift System. *Tectonics, 10(6)*, 1257-1273.

Brancolini, G., Cooper, A.K., & Coren, F. (1995). Seismic facies and glacial history in the Western Ross Sea (Antarctica). In A.K. Cooper, P.F. Barker, G. Brancolini (Eds.), *Geology and Seismic Stratigraphy of the Antarctic Margin, Antarctic Research Series* (Vol. 68, pp. 209-233). Washington, DC: American Geophysical Union.

Brenn, G.R., Hansen, S.E. & Park, Y. (2017). Variable thermal loading and flexural uplift along Transantarctic Mountains, Antarctica. *Geology, 45*, 463-466.

Brotchie, J.F., & Silvester, R. (1969). On crustal flexure. *Journal of Geophysical Research, 74*, 5240-5252.

Busetti, M., Spadini, G., Van der Wateren, F.M, Cloetingh, S. & Zanolla, C. (1999). Kinematic modelling of the West Antarctic Rift System, Ross Sea, Antarctica. *Global and Planetary Change, 23 (1–4)*, 79-103. https://doi.org/10.1016/S0921-8181(99)00052-1.

Chaput, J., Aster, R.C., Huerta, A., Sun, X., Lloyd, A., Wiens, D., Nyblade, A., Anandakrishnan,

S., Winberry, J.P., & Wilson, T. (2014). The crustal thickness of West Antarctica. *Journal of Geophysical Research, 119,* 378-395.

Chen, J. (2015). The Influence of Lithospheric Flexure Induced by Volcano Loading on Neogene Basin Evolution in McMurdo Sound, West Antarctica. (Master's thesis). *Retrieved from https://etd.ohiolink.edu/. (osu1448967436)*. Columbus, Ohio: Ohio State University.

Cooper, A.K., Barker, P.F., & Brancolini, G. (Eds.). (1995). Geology and Seismic stratigraphy of Antarctic Margin. *Antarctic Research Series (Vol. 68).* Washington, D.C.: American Geophysical Union.

Cooper A.K. & Davey F.J. (1985). Episodic Rifting of the Phanerozoic Rocks of the Victoria Land basin, Western Ross Sea, Antarctica. *Science, 229*, 1085-1087.

Cooper, A.F., Adam, L.J., Coulter, R.F., Eby, G.N., & McIntosh, W.C. (2007). Geology, geochronology and geochemistry of a basanitic volcano, White Island, Ross Sea, Antarctica. *Journal of Volcanology and Goethermal Research, 165*, 189-216.

Cooper, A. K., Davey, F.J., & Cochrane, G.R. (1987). Structure of extensionally rifted crust beneath the western Ross Sea and Iselin Bank, Antarctica, from sonobuoy seismic data. In A.K. Cooper & F.J. Davey (Eds.). *The Antarctic Continental Margin; Geology and Geophysics of the Western Ross Sea* (pp. 93-118). Circum-Pacific Council for Energy and Mineral Resources, Houston, TX.

Cooper, A.K., Davey, F.J., & Hinz, K. (1991). Crustal extension and origin of sedimentary basins beneath the Ross Sea and the Ross Ice Shelf, Antarctica. *Geological Evolution of Antarctica, 5,* 285-291.

Davey, F.J. & Brancolini, G. (1995). The Late Mesozoic and Cenozoic Structural Setting of the Ross Sea Region. In A. K. Cooper, P. F. Barker, G. Brancolini (Eds.), *Geology and Seismic Stratigraphy of the Antarctic Margin*. https://doi.org/10.1029/AR068p0167.

Davey, F.J., Cande, S.C., & Stock, J.M. (2006). Extension in the western Ross Sea region-links between Adare Basin and Victoria Land Basin. *Geophysical Research Letters, 33*.

Decesari, R.C., Sorlien, C.C., Luyendyk, B.P., Wilson, D.S., Bartek, L., Diebold, J., & Hopkins, S.E. (2007). Regional seismic stratigraphic correlations of the Ross Sea: Implications for the tectonic history of the West Antarctic Rift System. *USGS Open File Report 2007-1047,* Short Research Paper 052, 4 p.

Dunbar, G.B., Atkins, C., Magens, D., Niessen, F., & ANDRILL-SMS Science team (2009). Physical Properties of the AND-2A core, ANDRILL Southern McMurdo Sound Project, Antarctica. *Terra Antarctica, 15(1),* 49-56.

Emry, E.L., Nyblade, A. A., Julià, J., Anandakrishnan, S., Aster, R.C., Wiens, D.A., Huerta, A.D., & Wilson, T.J. (2015). The mantle transition zone beneath West Antarctica: Seismic evidence

for hydration and thermal upwellings. *Geochemistry, Geophysics, Geosystems, 16(1)*, 40-58.

Esser, R.P., Kyle, P.R., & McIntosh, W.C. (2004). 40Ar/39Ar dating of the eruptive history of Mount Erebus, Antarctica: volcano evolution. *Bulletin of Volcanology, 66*, 671-686.

Fielding, C.R. (2018). Stratigraphic architecture of Cenozoic succession in the McMurdo Sound region, Antarctica: An archive of polar paleoenvironmental change in failed rift setting. *Sedimentology, 65,* 1-61.

Fielding, C.R., Whittaker, J., Henrys, S.A., Wilson, T.J., & Naish, T.R. (2008). Seismic facies and stratigraphy of the Cenozoic succession in McMurdo Sound, Antarctica: Implications for tectonic, climatic, and glacial history. *Palaeogeography, Palaeoclimatology, Palaeoecology, 260*, 8-29.

Finn, C.A., Muller, R.D., & Panter, K.S. (2005). A Cenozoic diffuse alkaline magmatic province (DAMP) in the southwest Pacific without rift or plume origin. *Geochemistry, Geophysics, Geosystems, 6(1)*, Q02005. https://doi.org/10.1029/2004GC000723.

Fretwell, P., Pritchard, H.D., Vaughan, D.G., Bamber, J.L., Barrand, N.E., Bell, R., et al. (2013). Bedmap2: Improved ice bed, surface and thickness datasets for Antarctica. *Cryosphere, 7(1)*, 375-393. https://doi.org/10.5194/tc-7-375-2013.

Graw, J.H., Adams, A.N., Hansen, S.E., Wiens, D.A., Hackworth, L., & Park, Y. (2016). Upper mantle shear wave velocity structure beneath northern Victoria Land, Antarctica: Volcanism and uplift in the northern Transantarctic Mountains. *Earth and Planetary Science Letters, 449*, 48-60.

Harry, D.L., Jourdan L.A., & Jha, S. (2018). Geodynamic models of the West Antarctic Rift System: Implications for the mantle thermal state. *Geosphere, 14 (6)*, 2407-2429.

Hall, J.M., Wilson, T.J. & Henrys, S.A. (2007). Structure of Central Terror Rift, Western Ross Sea, Antarctica. In Cooper, et al. (Eds.) *Antarctica: A Keystone in a Changing World – Online Proceedings of the 10th ISAES*. USGS Open-File Report 2007.

Hansen, S.E., Graw, J.H., Kenyon, L.M., Nyblade, A.A., Wiens, D.A., Aster, R.C., et al. (2014). Imaging the Antarctic mantle using adaptively parameterized P-wave tomography: Evidence for heterogeneous structure beneath West Antarctica. *Earth and Planetary Science Letters, 408*, 66-78. https://doi.org/10.1016/j.epsl.2014.09.043.

Heeszel, D.S., Wiens, D.A., Anandakrishnan, S., Aster, R.C., Dalziel, I.W.D., Huerta, A.D., et al. (2016). Upper mantle structure of central and West Antarctica from array analysis of Rayleigh wave phase velocities. *Journal of Geophysical Research Solid Earth, 121*, 1758-1775. https://doi.org/10.1002/2015JB012616.

Henrys, S.A., Wilson, T.J., Fielding, C.R., Hall, J. & Naish, T.R. (2007). Tectonic history of mid-Miocene to present southern Victoria Land Basin, inferred from seismic stratigraphy in

McMurdo Sound, Antarctica. In A.K. Cooper, P.J., Barrett, H. Stagg, B. Storey, E. Stump, W. Wise (Eds.), *Antarctica: A Keystone in a Changing World. Proceedings of the 10th International Symposium on Antarctic Earth Sciences*. Washington, DC: The National Academies Press.

Hertz, H. (1884). On the equilibrium of floating elastic plates. *Wiedemann's Annals, 22*, 449-455.

Hinz, K. & Block, M. (1983). Results of Geophysical Investigations in the Weddell Sea and in the Ross Sea, Antarctica. *World Petroleum Congress.*

Hole, M.J., & LeMasurier, W.E. (1994). Tectonic controls on the geochemical composition of Cenozoic, mafic alkaline volcanic rocks from West Antarctica. *Contributions to Mineralogy and Petrology, 117*, 187-202.

Horgan, H., Naish, T., Bannister, S., Balfour, N., & Wilson, G. (2005). Seismic stratigraphy of the Plio-Pleistocene Ross Island flexural moat-fill: a prognosis for ANDRILL Program drilling beneath McMurdo-Ross Ice Shelf. *Global and Planetary Change, 45(1-3)*, 83-97.

Jha, S., Harry, D.L., & Schutt, D.L. (2017). Toolbox for Analysis of Flexural Isostasy (TAFI)—A MATLAB toolbox for modeling flexural deformation of the lithosphere. *Geosphere*, *13(5)*, 1555–1565. https://doi.org/10.1130/GES01421.1.

Ji, F., Gao, J., Li, F., Shen, Z., Zhang, Q., & Li, Y. (2017). Variation of effective elastic thickness over the Ross Sea and Transantarctic Mountains and implication for their structure and tectonics. *Tectonophysics, 717,* 127-138.

Krissek, L., Browne, G., Carter, L., Cowan, E., Dunbar, G., McKay, R., et al. (2007). Sedimentology and Stratigraphy of the AND-1B Core, ANDRILL McMurdo Ice Shelf Project, Antarctica. *ANDRILL Research and Publications*, *Paper 22*, 185-222.

Kyle, P.R. (1981a). Glacial history of the McMurdo Sound area as indicated by the distribution and nature of McMurdo Volcanic Group rocks. *Antarctic Research Series, 33*, 403-412.

Kyle, P.R. (1981b). Mineralogy and geochemistry of a basanite to phonolite sequence at Hut Point Peninsula, Antarctica, based on core from Dry Valley Drilling Project Drillholes 1, 2 and 3. *Journal of Petrology, 22*, 451-500.

Kyle, P.R. (1977). Mineralogy and glass chemistry of recent volcanic ejecta from Mt. Erebus, Ross Island, Antarctica. *New Zealand Journal of Geology and Geophysics, 20 (6),* 1123-1146.

Kyle, P.R. (1990). McMurdo Volcanic Group, western Ross Sea: Introduction. In W.E. LeMasurier & J.W. Thompson (Eds.). *Volcanoes of the Antarctic Plate and Southern Ocean (pp. 19-25).* American Geophysical Union, Washington, D. C.

Kyle, P.R., & Cole, J.W. (1974). Structural Control of Volcanism in the McMurdo Volcanic Group, Antarctica. *Bulletin of Volcanology, 38 (1),* 16-35.

Lawrence, J.F., Wiens, D.A., Nyblade, A.A., Anandakrishnan, S., Shore, P.J., & Voigt, D. (2006). Crust and upper mantle structure of the Transantarctic Mountains and surrounding regions from receiver functions, surface waves, and gravity: Implications for uplift models. *Geochemistry Geophysics Geosystems, 7*, Q10011. https://doi.org/10.1029/2006GC001282.

LeMasurier, W.E. & Landis, C.A. (1996). Mantle-plume activity recorded by low-relief erosion surfaces in West Antarctica and New Zealand. *Geological Society of America Bulletin, 108*, 1450-1466.

Lloyd, A.J., Weins, D.A., Nyblade, A.A., Anandakrishnan, A., Aster, R.C., Huerta, A.D., et al. (2015). A seismic transect across West Antarctica: Evidence for mantle thermal anomalies beneath the Bentley Subglacial Trench and the Marie Byrd Land Dome. *Journal of Geophysical Research, 120*, 8349-8460.

Molzahn, M., Reisberg, L. & Worner, G. (1996). Os, Sr, Nd, Pb, O isotope and trace element data from the Ferrar flood basalts, Antarctica: Evidence for an enriched subcontinental lithospheric source. *Earth and Planetary Science Letters, 144*, 529-546.

Nadai, A. (1963). *Theory of flow and fracture of solids*. New York, McGraw-Hill, 705 pp.

Naish, T., Powell, R., Levy, R., & ANDRILL-MIS Science Team (2007a). Background to the ANDRILL McMurdo Ice Shelf Project (Antarctica) and Initial Science Volume. *Terra Antarctica, 14(3)*, 121-130.

Naish, T., Powell, R., Levy, R., Henrys, S., Krissek, L., Niessen, F., & ANDRILL-MIS Science Team (2007b). Synthesis of the Initial Scientific Results of the MIS Project (AND-1B Core), Victoria Land Basin, Antarctica. *Terra Antarctica, 14(3)*, 317-327.

Naish, T.R., Powell, R.D., Barrett, P.J., Levy, R.H., Henry, S., Wilson, G.S., & the ANDRILL-MIS Science Team (2008). Late Neogene climate history of the Ross Embayment from the AND-1B drill core: Culmination of three decades of Antarctic margin drilling. In A.K. Cooper (Ed.) *Antarctica: A keystone in a changing world, Proceedings of the 10th International Symposium on Antarctic Earth Sciences* (pp. 71-82). Washington, DC: The National Academies Press.

Nardini, I., Armienti, P., Rocchi, S., Dallai, L., & Harrison, D. (2009). Sr-Nd-Pb-He-O isotope and geochemical constraints on the genesis of Cenozoic magmas from the West Antarctic Rift. *Journal of Petrology, 50*, 1359-1375.

Niessen, F., Gebhardt, A.C., Kuhn, G., Magens, D., & Monien, D. (2013). Porosity and density of the AND-1B sediment core, McMurdo Sound Region, Antarctica: Field consolidation enhanced by grounded ice. *Geosphere, 9(3)*, p. 489-509. https://doi.org/ 10.1130/GES00704.1

Paulsen, T., Wilson, T.J., Demosthenous, C., Millan, C., Jarrard, R., & Laufer, A.L. (2014). Kinematics of the Neogene Terror Rift: Constraints from calcite twinning strains in the ANDRILL McMurdo Ice Shelf (AND-1B) core, Victoria Land Basin, Antarctica. *Geosphere,*

10, 828-841.

Perinelli, C., Armienti, P., & Dallai, L. (2006). Geochemical and O-isotope constraints on the evolution of lithospheric mantle in the Ross Sea rift area (Antarctica). *Contributions to Mineralogy and Petrology, 151*, 245-256.

Rilling, S.E., Mukasa, S.B., Wilson, T.J., & Lawver, L.A. (2007). 40Ar-39Ar Age constraints on volcanism and tectonism in the Terror Rift of the Ross Sea, Antarctica. In A.K. Cooper et al., (Eds.). *Antarctica: A Keystone in a Changing World - Online Proceedings of the 10th ISAES Conference*. U.S. Geological Survey and The National Academy Press.

Rilling, S.E., Mukasa, S.B., Wilson, T., Lawver, L., & Hall, C. (2009). New determinations of 40Ar/39Ar isotopic ages and flow volumes for Cenozoic volcanism in the Terror Rift, Ross Sea, Antarctica. *Journal of Geophysical Research, 114*.

Rocchi, S., Armienti, P., & Vincenzo, G.D. (2005). No plume, no rift magmatism in the West Antarctic Rift, in Plates, Plumes, and Paradigms. *Geological Society of America Special Paper 388.*

Rocchi, S., Armienti, P., D'Orazio, M., Tonarini, S., Wijbrans, J.R., & Vincenzo, G.D. (2002). Cenozoic magmatism in the western Ross Embayment Role of mantle plume versus plate dynamics in the development of the West Antarctic Rift System. *Journal of Geophysical Research, 107(B9)*, 2195. https://doi.org/10.1029/2001JB000515

Shen, W., Wiens, D.A., Anandakrishnan, S., Aster, R.C., Gerstoft, P., Bromirski, P.D., et al. (2018). The crust and upper mantle structure of central and West Antarctica from Bayesian inversion of Rayleigh wave and receiver functions. *Journal of Geophysical Research: Solid Earth, 123,* 7824-7849.

Siddoway, C.S., Suzanne, L.B., Fitzgerald, P.G., Fanning, C.M., & Luyendyk, B.P. (2004). Ross Sea mylonites and the timing of intracontinental extension within the West Antarctic rift system. *Geology*, *32 (1)*, 57-60.

Siddoway, C.S. (2007). Tectonics of the West Antarctic rift system: new light on the history and dynamics of distributed intracontinental extension. In A.K. Cooper, P. J., Barrett, H. Stagg, B. Storey, E. Stump, W. Wise (Eds.), *Antarctica: a Keystone in a Changing World – Proceedings of the 10th International Symposium on Antarctic Earth Sciences* (pp. 91-114). Washington, DC: The National Academies Press.

Stern, T.A., Davey, F.J., & DeLisle, G. (1991). Lithospheric flexure induced by the load of Ross Archipelago, southern Victoria Land, Antarctica. In M.R.A. Thomson, J.A. Crame, J.W. Thomson, (Eds.), *Geological Evolution of Antarctica* (pp. 323-328). New York, Cambridge University Press.

Storey, B.C., Leat, P.T., Weaver, S.D., Pankhurst, R.J., Bradshaw, J.D., & Kelley, S. (1999). Mantle plumes and Antarctica-New Zealand rifting: evidence from mid-Cretaceous mafic

dykes. *Journal of the Geological Society, 156(4)*, 659-671.

ten Brink, U.S., Hackney, R.I., Bannister, S., Stern, T.A., & Makovsky, Y. (1997). Uplift of the Transantarctic Mountains and the bedrock beneath the East Antarctic ice sheet. *Journal of Geophysical Research, 102(B12)*, 27603-27621. https://doi.org/10.1029/97JB02483.

Tonarini, S., Rocchi, S., Aremienti, P., & Innocenti, F. (1997). Constraints on timing of Ross Sea rifting inferred from Cainozoic intrustions from northern Victoria Land, Antarctica. In C. A. Ricci (Eds.), *The Antarctic Region: Geological Evolution and Processes*, (pp. 511-521). Terra Antarctica, Siena.

Turcotte, D.L., & Schubert, G. (2014). *Geodynamics*. New York, Cambridge University Press.

Watson, T., Nyblade, A., Wiens, D. A., Anandakrishnan, S., Benoit, M., Shore, P. J., Voigt, D., & VanDecar, J., (2006). P and S velocity structure of the upper mantle beneath the Transantarctic Mountains, East Antarctic craton, and Ross Sea from travel time tomography. *Geochemistry, Geophysics, Geosystems 7(7)*. DOI:10.1029/2005GC001238.

Weaver, S.D., Storey, B.C., Pankhurst, R.J., Mukasa, S.B., DiVenere, V.J., & Bradshaw, J.D. (1994). Antarctica–New Zealand rifting and Marie Byrd Land lithospheric magmatism linked to ridge subduction and mantle plume activity. *Geology, 22*, 811-814.

Wenman, C.P., Harry, D.L., & Jha, S. (in review). Tectonic and Stratigraphic Evolution of the Victoria Land Basin and Ross Island. *Geochemistry, Geophysics, Geosystems*.

White-Gaynor, A.L., Nyblade, A.A., Aster, R.C., Wiens, D.A., Bromirski, P.A., Gerstoft, P., Stephen, R.A., Hansen, S.E., Wilson, T., Dalziel, I.W., Huerta, A.D., Winberry, J.P., & Anandakrishnan, S. (2019). Heterogeneous upper mantle structure beneath the Ross Sea Embayment and Marie Byrd Land, West Antarctica, revealed by P-wave tomography. *Earth and Planetary Science Letters, 513*, 40-50.

Wilch, T.I., McIntosh, W.C., Panter, K.S., Dunbar, N.W., Smellie, J.L., Fargo, A.J., Ross, J.I., Antibus, J.V., & Scanlan, M.K. (2011). Two-stage growth of the Late Miocene Minna Bluff Volcanic Complex, Ross Embayment, Antarctica: implications for ice-sheet and volcanic histories, paper presented at AGU Fall Meeting, Dec. 5-9, San Francisco, CA.

Wilson, D.S., & Luyendyk, B.P. (2009). West Antarctic paleotopography estimated at the Eocene-Oligocene climate transition. *Geophysical Research Letters*, *36*, L16302.

Wilson, G.S., Levy, R.H., Browne, G., Cody, R., Dunbar, N., Florindo, F., & ANDRILL-MIS Science Team (2007). Preliminary Integrated Chronostratigraphy of the AND-1B Core, ANDRILL McMurdo Ice Shelf Project, Antarctica. *ANDRILL Research and Publications, Paper 46*, 297-316.

Worner, G. (1999). Lithospheric dynamics and mantle sources of alkaline magmatism of the Cenozoic West Antarctic Rift System. *Global and Planetary Change, 23,* 61-77.

Wright, A.C., & Kyle, P.R. (1990a). A. 21 Mount Discovery. In LeMasurier, W.E. & Thompson, J.W. (Eds.), *Volcanoes of the Antarctic Plate and Southern Oceans* (pp. 120-123). American Geophysical Union, Washington D.C.

Wright, A.C., & Kyle, P.R. (1990b). A.16 Mount Terror. In W.E. LeMasurier & J.W. Thompson, (Eds.), *Volcanoes of the Antarctic Plate and Southern Oceans* (pp. 99-102). American Geophysical Union, Washington D.C.

Wright, A.C., & Kyle, P.R. (1990c). A. 20 Minna Bluff. In W.E. LeMasurier & J.W. Thompson, (Eds.), *Volcanoes of the Antarctic Plate and Southern Oceans* (pp. 117-119). American Geophysical Union, Washington D.C.

Wright, A.C., & Kyle, P.R. (1990d). A.15 Mount Bird. In W.E. LeMasurier & J.W. Thompson, (Eds.), *Volcanoes of the Antarctic Plate and Southern Oceans* (pp. 97-98). American Geophysical Union, Washington D.C.

CHAPTER 4
Time varying flexural rigidity around Ross Island, Antarctica[3]

4.1 Introduction

Ross Island is a late Miocene to recent volcanic island that straddles the active Terror Rift, which is located along the axis of the Victoria Land Basin (VLB) in the western Ross Sea of West Antarctica (Figure 4.1). The VLB lies along the western edge of the Late Cretaceous through Quaternary West Antarctic Rift System (WARS). The Terror Rift has been the most tectonically and magmatically active portion of the VLB since middle Miocene time. Volcanism constructed Ross Island at the southern end of the Terror Rift in four distinct phases since ca. 4.6 Ma, creating several flexural sub-basins that in composite form a semi-continuous sedimentary moat around Ross Island.

Recent two-dimensional (2-D) elastic plate flexural models (Chapter 3) show that the shape of the younger sub-basins located on the southwest side of the island requires a lower flexural rigidity than the older basins on the north and northeast side of the island. These models thus show that the flexural rigidity of the lithosphere under Ross Island varies either with time or with location. Both explanations for varying lithospheric strength around Ross Island are plausible. The weakening of the lithosphere with time may result from thinning of the lithosphere caused by an ongoing extension or by heating of the lithosphere as a result of repeated intrusions of magma. Alternatively, a spatial difference in the strength of the lithosphere has been suggested to result from the presence of hotter mantle on the west side of the island (Hansen et al., 2014; Brenn et al., 2017), possibly enhanced by faulting within the Terror Rift beneath the island (Hall et al., 2007).

The 2-D models constrain the flexural rigidity of the lithosphere locally during the time

[3] Manuscript in preparation for submission to Geophysical Research Letters

each sub-basin formed. They do not distinguish whether variations in rigidity are due to spatial or temporal changes in the lithosphere's strength. In this paper, we present three-dimensional (3-D) flexural models of regional subsidence around Ross Island to test the hypothesis that the strength of the lithosphere around the island varied with time as the rift evolved.

4.2 Geological Background

Ross Island is a volcanic island containing four major volcanic centers – Mt. Bird (4.6 Ma - 3.1 Ma), Mt. Terror (1.7 Ma - 0.8 Ma), Hut Point Peninsula (HPP, 1.3 Ma - 0.4 Ma) and active volcano, Mt. Erebus (1.3 Ma - present) (Armstrong, 1978; Wright and Kyle, 1990a; b; c; d; Esser et al., 2004). These volcanic centers are part of the McMurdo Volcanic Group, which consists of middle Eocene to recent extrusive alkaline magmatic rocks emplaced along the western flank of the WARS (Weaver et al., 1994; Hole & LeMasurier, 1994; Tonarini et al., 1997; Mukasa and Dalziel, 2000; Rocchi et al., 2002; Nardini et al., 2009; Armienti and Perinelli, 2010). Ross Island lies at the southern end of the Terror Rift, which is a zone of Neogene volcanism and recent tectonism lying along the axis of the VLB (Cooper et al., 1987; Bannister et al., 2000; Hall et al., 2007). The VLB is the westernmost of four major rift basins (from the east: Eastern Basin, Central Basin, Northern Basin, Victoria Land Basins) in the WARS (Figure 4.1). Together, the rift basins comprise a broad late Cretaceous to Quaternary continental extensional province underlying the Ross Sea and the Ross Ice Shelf, extending from the Transantarctic Mountains in the west to Marie Byrd Land in the east (Behrendt et al., 1991).

Volcanism on Ross Island led to flexural subsidence of the lithosphere and formation of a well-developed flexural moat around the island (Figure 4.2). The sedimentary strata filling the moat has been imaged in seismic reflection data on the west side of the island and on the southeast

side of the island near Hut Point Peninsula (e.g. Cooper et al., 1991; Brancolini et al., 1995; Davey et al., 2000; Horgan et al., 2005; Decesari et al., 2007; Fielding et al., 2008; Fielding, 2018; Wenman et al., in review). Fielding et al. (2008) and Fielding (2018) identified basin-wide regional unconformities, which have been named R_a through R_k (from deepest upwards). Fielding and co-workers used these unconformities to develop a multiphase subsidence model for the VLB since late Eocene. Strata bound by unconformities R_a through R_e encompass the Oligocene early and main rift subsidence phases. The strata bound by unconformities R_e to R_g represent a late Oligocene through middle Miocene passive thermal subsidence phase (Fielding, 2018; Fielding et al., 2008). The middle Miocene and younger Terror Rift phase of subsidence is represented by strata lying above unconformity R_g. The onset of volcanism on Mt. Bird (the oldest of the Ross Island volcanic centers) approximately coincides with the age of unconformity R_i (4.0 Ma - 4.6 Ma) (Wenman et al., in review). Wenman et al. identified three additional local unconformities, named RMU1, RMU2, and RMU3, within the flexural moat around Ross Island. They correlated each of the RMU-series unconformities with the onset of volcanism at the other major volcanic centers on Ross Island. The strata lying between unconformities R_i and RMU2 is interpreted to have been deposited during the period Mt. Bird was active. The strata between RMU2 and R_k correspond to the period when Mt. Terror was active, and the intervals between R_k and RMU3 and RMU3 and the seafloor (SF) correspond to the main periods of volcanism at HPP and Mt. Erebus, respectively. Hence, the strata between unconformity R_i (4.6 Ma) and the seafloor encompasses multiple episodes of subsidence. The sedimentary moat around Ross Island is a composite of smaller flexural sub-basins formed at different times and different positions, according to when each of the various volcanic centers was active.

4.3 Method, data, and modeling description

Three-dimensional elastic plate flexural models were used to simulate subsidence around Ross Island during the last 4.6 Ma, since the onset of volcanic loading and formation of seismic horizon R_i. The isopach thickness of strata between R_i and the seafloor was used as a proxy for subsidence. The R_i-SF isopach thickness was taken from the 1 km x 1 km grid as discussed in chapter 3.

Flexural subsidence was modeled with the program TAFI (Jha et al., 2017). Subsidence (w) is modeled as the deflection of an infinite elastic plate subjected to a vertical point load:

$$w(r) = Q_0 \frac{\alpha^2}{2\pi D} kei \frac{r}{\alpha} \tag{4.1}$$

where r is the distance from the load, Q_0 is the load magnitude, kei is zeroth-order kelvin function, D is the flexural rigidity of the lithosphere and α is the flexural parameter (Hertz, 1884; Nadai, 1963; Brotchie and Sylvester, 1968; Turcotte, 1979). The flexural parameter α is given by:

$$\alpha = \left[\frac{D}{\Delta\rho + \frac{ET_e}{R^2}}\right]^{1/4} \tag{4.2}$$

where E is Young's modulus (8.35 x 10^{10} N/m^2), T_e is the elastic plate thickness, R is the radius of the Earth (6.37 x 10^6 m), and $\Delta\rho$ is the density contrast between the mantle and the material filling the basin. In this study, we follow Aitken et al. (2012) and use a mantle density of 3260 kg/m^3, which is consistent with tomographic evidence of a warm mantle beneath the western WARS (Hansen et al., 2014; Heeszel et al., 2016; Shen et al., 2018). The density of material filling the basin was taken to be 2200 kg/m^{3,} which is the average density of sedimentary rocks encountered in AND-1B and AND-2A drill holes (Dunbar et al., 2009; Niessen et al., 2013).

The point load solution discussed above in Equation 4.1 is convolved with a load function, to generate flexure models presented in this study. The load function consists of 1 km x 1 km

prismatic loads located at each of the volcanic centers on Ross Island. For HPP, an elongated 1 km x 2 km load aligned along the southwest trend of HPP was used.

The model parameters that most strongly control the shape of the flexural basins are flexural rigidity (D) and the load magnitude (Q_0). Flexural rigidity controls the wavelength of flexural deformation, and the load magnitude (together with D) controls the basin depth. The three-dimensional flexural models were initially generated using the flexural rigidity and load magnitudes and positions determined by 2-D flexural modeling study in chapter 3. The models were then iteratively refined, adjusting the load magnitude and flexural rigidity as needed to obtain a good fit between modeled subsidence and the thickness of the R_i to seafloor isopach interval. The criteria for identifying a good fit are that the location of depocenters and approximate shapes of flexural sub-basins in the model match those on the R_i-SF isopach map.

Two classes of models were examined. In the first series, a single load function is used that includes all volcanic loads. The flexural rigidity and load magnitudes are varied to find a model that best fits the shape and depth of the composite flexural basin surrounding the island. This class of models is intended to provide an estimate of the best fitting time-invariant flexural rigidity. We examine two models in this class: one including only volcanic loads that comprise Ross Island and another that includes nearby volcanic loading on the Beaufort Island and a seamount to the north of the island. In the second class of models, subsidence is modeled separately (by varying D and the load magnitude) for each of the sub-basins surrounding the island. The modeled shape of the composite basin is obtained by summing the subsidence models for each individual sub-basin. This class of models allows for varying flexural rigidity through time. Misfits for all model were obtained by subtracting the flexure model from R_i-SF isopach map and are shown by contour lines.

4.4 Results

Model Class 1a: This model class used time-invariant flexural rigidity for loads limited to Ross Island. Model with a D of 3.6 x 10^{19} N-m and a load function with loads limited to Ross Island (Table 1) shows a continuous moat around Ross Island (Figure 4.3a). The misfit for this model, as shown by misfit contours (Figure 4.3b) around Mt. Bird ranges from approximately 0 m to 465 m, to the north of Mt. Terror from approximately 100 m to 731 m, -150 m to 191 m to the south of HPP and 140 m to 330 m to the west of Mt. Erebus. A negative misfit suggests that the model basins are shallower than those in the R_i-SF isopach. A positive misfit suggests that the flexure model basins are deeper than those in the R_i-SF isopach. The model with highest D tested in this class, with D = 2 x 10^{21} N-m (Figure 4.3c; Table 1) has a misfit to the north of Mt. Bird that is between -300 m to 150 m. The misfits to the southwest of HPP are between -500 m to -140 m; and to the north of Mt. Terror and west of Mt. Erebus is -700 m to -200 m and -400 m to 200 m, respectively (Figure 4.3d). The best fit model (Figure 4.3e; Table 1) for loads limited to Ross Island has a D of 2.2 x 10^{20} N-m. The misfit range for this model to the north of Mt. Bird is 0 m – 405 m, to the north of Mt. Terror is 0 m – 400 m, to the southwest of HPP is -150 m to 191 m and 140 m to 330 m to the west of Mt. Erebus (Figure 4.3f).

Model Class 1b: Depocenters around Beaufort Island, and around a seamount to the north of Ross Islands were not captured in any of the models of this class. To account for the missing depocenters and flexure sub-basins to the north of Ross Island in Model Class 1a, we added additional load prisms at Beaufort Island and a seamount to the northwest of Beaufort Island (Figure 4). A model with a flexural rigidity of D = 2.6 x 10^{20} N-m (Table 1) provides the best fit to the flexure sub-basin around Ross Island and an improved fit around Beaufort Island and seamount to its north (Figure 4.4a). Overlapping flexure moats around Ross Island extends to the

north and includes another circular flexure moat around the Beaufort Island and the seamount. The misfit between this model and R_i-SF isopach range from 200 m to 493 m to the north of Mt. Bird, -50 m to 364 m north of Mt. Terror, 0 m to 669 m southwest of HPP, 0 m to 778 m west of Mt. Erebus, -200 m to 655 m across the flexure moat around Beaufort Island and 100 m to 1181 m across the flexure moat around the seamount (Figure 4.4b). This model shows a wider flexure moat extending to the north into VLB. The model shows approximately 10 km wider flexure sub-basin to the north of Mt. Bird, and approximately 5 km wider flexure sub-basin to the north of Mt. Terror when compared with similar models of Class 1a.

Models of Class 1a and 1b were generated to fit the composite flexural subsidence around Ross Island with a single time-invariant flexural rigidity. Models in this class with D greater than 2×10^{20} N-m, in general provide poor fit for flexural subsidence around smaller volcanic features (e.g., Beaufort Island, HPP, seamount). Models with D lower than 3.6×10^{19} N-m, which capture the flexure basin around the smaller features but do not fit the shape of the basin near the larger loads (e.g. Mt. Terror, Mt. Erebus, and Mt. Bird). A time-invariant flexural rigidity model is unable to simultaneously fit all parts of the composite flexural basin in the R_i-SF isopach map.

Model Class 2: In Class 2 models, flexural subsidence due to loading from each volcanic center is modeled by varying the flexural rigidity and load distribution between each of the different volcanic loading episodes. The total subsidence due to loading since volcanism began is obtained by summing the flexural subsidence for each loading episode. The modeled total subsidence is compared to the R_i-SF isopach to determine the quality of the fit. This model class (Figure 4.5a, Table 1) shows an improved fit to the thickness of the R_i-SF isopach interval in comparison to Class 1 models. The model shows steeper slopes on the sides of the basin to the west of Mt. Erebus, an elongated flexure basin in the HPP area and a shallower arcuate flexure

sub-basin to the north of Mt. Terror and Mt. Bird. Loading at Beaufort Island and the seamount also resulted in the formation of smaller and shallower flexure sub-basins to the north of Ross Island. Average misfits (mean of misfit range) for this model (Figure 4.5b) for Mt. Bird, Mt. Terror, HPP, Mt. Erebus are 226 m, 345 m, 231 m, and 340 m, respectively. Average model misfit around Beaufort Island and the seamount are 96 m and 304 m, respectively. These misfit values suggest that this class of model approximates the shape of the flexure basin in the area of study and fits R_i-SF much better than the models of Class 1. A small flexure basin is observed to the south of Ross Island which is probably a result of flexural subsidence due to loading at White Island. The center of mass for White Island lies farther south than the area of investigation, and hence we did not make any attempt to fit that basin.

4.5 Discussion

The time-invariant flexural rigidity models (Class 1) are unable to simultaneously match the widths of each of the individual flexure sub-basins around Ross Island, as seen from the misfit models. The time-varying flexural rigidity models (Class 2) show improvement in the fit of each flexure sub-basins, as well as the overall fit of the composite flexural basin around the island. The better fit of the time-varying models suggests that flexural rigidity around Ross Island decreased from 3.0×10^{19} N-m at the onset of volcanism 4.6 Ma to 2.6×10^{19} N-m today.

The strata between R_i and seafloor, represented by R_i-SF isopach, contains subsidence in the southern VLB due to both flexure and rifting. In the misfit figures presented for each model class, we have removed the flexural subsidence signature due to loading on Ross Island and the volcanic features to north of Ross island. Removing the flexural subsidence signatures from the subsidence recorded in the R_i-SF isopach interval isolates the subsidence that is due to rifting. Prior to the flexural correction, the southern VLB is shown to be dominated by the semi-circular

sedimentary moat around Ross Island. After removal of the flexure signal, an approximately uniform width basin striking North-Northwest becomes evident, which we attribute to ongoing Neogene extension in the VLB.

4.6 Conclusions

Flexural rigidity around Ross Island was modeled using constant rigidity (time-invariant) elastic plate models as well as models with time-varying flexural rigidity. The constant flexural rigidity model (best fit - 2.2 x 10^{20} N-m for model class 1a; 2.6 x 10^{20} N-m for model class 1b) through time results in a relatively poor fit to subsidence around volcanic centers in the southern and central VLB over last 4.6 Ma. Time-variant models (class 2), where the flexural rigidity varied through time, show improved fit in each sub-basin (except poorly constrained models of Mt. Terror sub-basin) with best fit flexural rigidities of 3.0 x 10^{19} N-m, 1.2 x 10^{19} N-m, 26 x 10^{19} N-m when Mt. Bird, HPP and Mt. Erebus were active. The variations in magnitude of these flexural rigidities are not resolvable by models presented here.

4.7 Figures in chapter 4

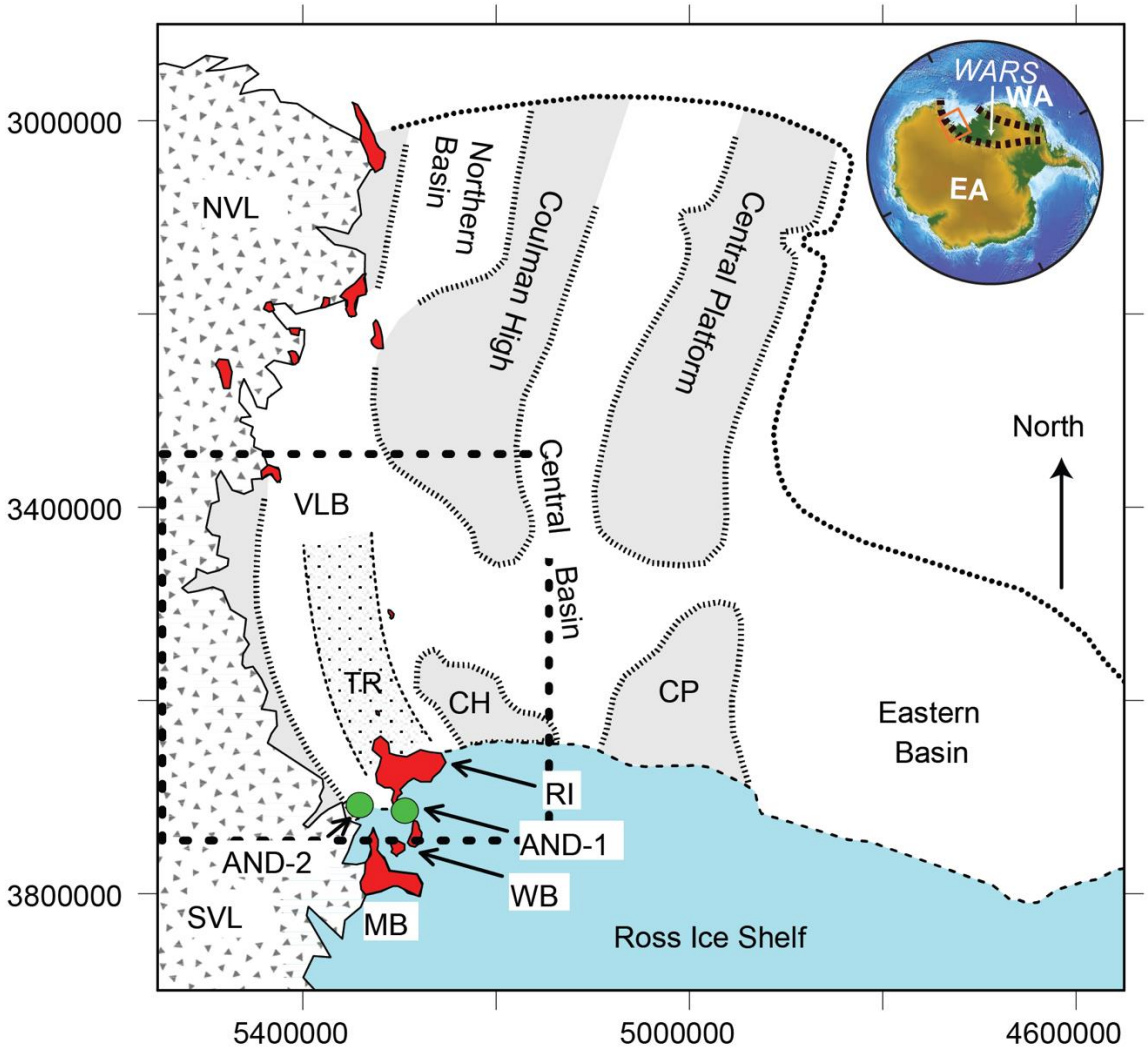

Figure 4.1. Major tectonic features in the Ross Sea (adapted from Wenman et al., in review). The area of the main figure is shown in the inset as a red box. Inset figure shows the location of West Antarctic Rift System (WARS) with respect to East Antarctica (EA) and West Antarctica (WA). In the main figure CH, CP – southern extension of Coulman High and Central Platform, respectively; WB – White and Black Island; MB – Minna Bluff; RI – Ross Island; TR (dotted pattern) – Terror rift; VLB – Victoria Land Basin; NVL and SVL (grey filled triangles) – North and South Victoria Land, respectively; Red – rocks of McMurdo Volcanic Province, including RI. Green circles – AND-1 and AND-2 drill holes. Ross Ice Shelf represented as a blue area. The dashed box in the main figure shows the area of study for this paper. Coordinates used in the paper are in Ross Sea Polar Stereographic RSPS 2000 reference frame (www.linz.govt.nz/data/geodetic-system/datums-projections-and-heights/projections/ross-sea-region-projections).

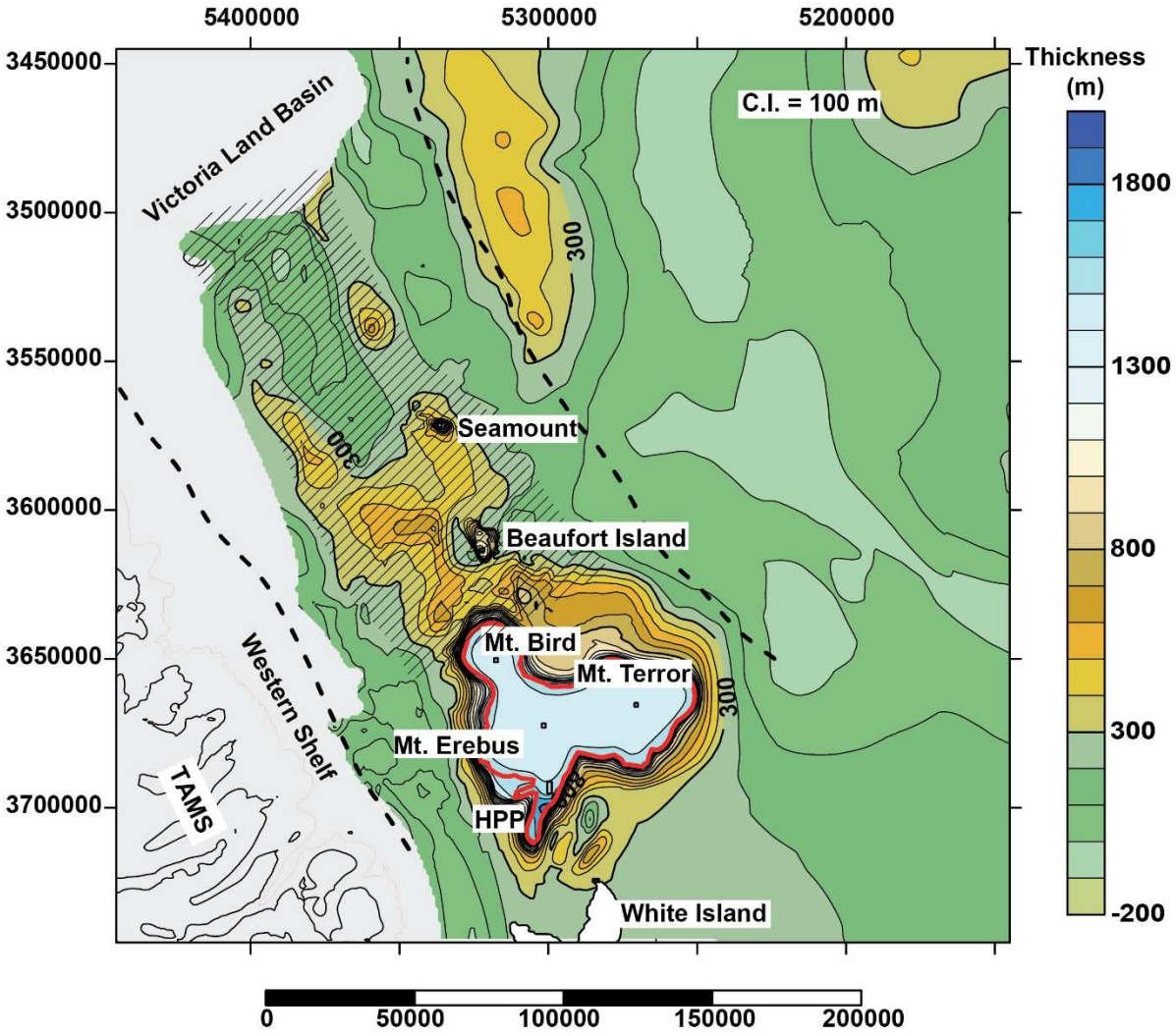

Figure 4.2. Isopach map of strata deposited around Ross Island over past 4.6 Ma bound by regional unconformity Ri and seafloor. Location of loading centers on and around Ross Island is shown. Victoria Land Basin is demarcated by dashed black lines, and the extent of Terror Rift is shown by grey diagonal lines. Transantarctic Mountains (TAMS) lie to the west of Ross Island. Grey area adjacent to TAMS is the Western Shelf.

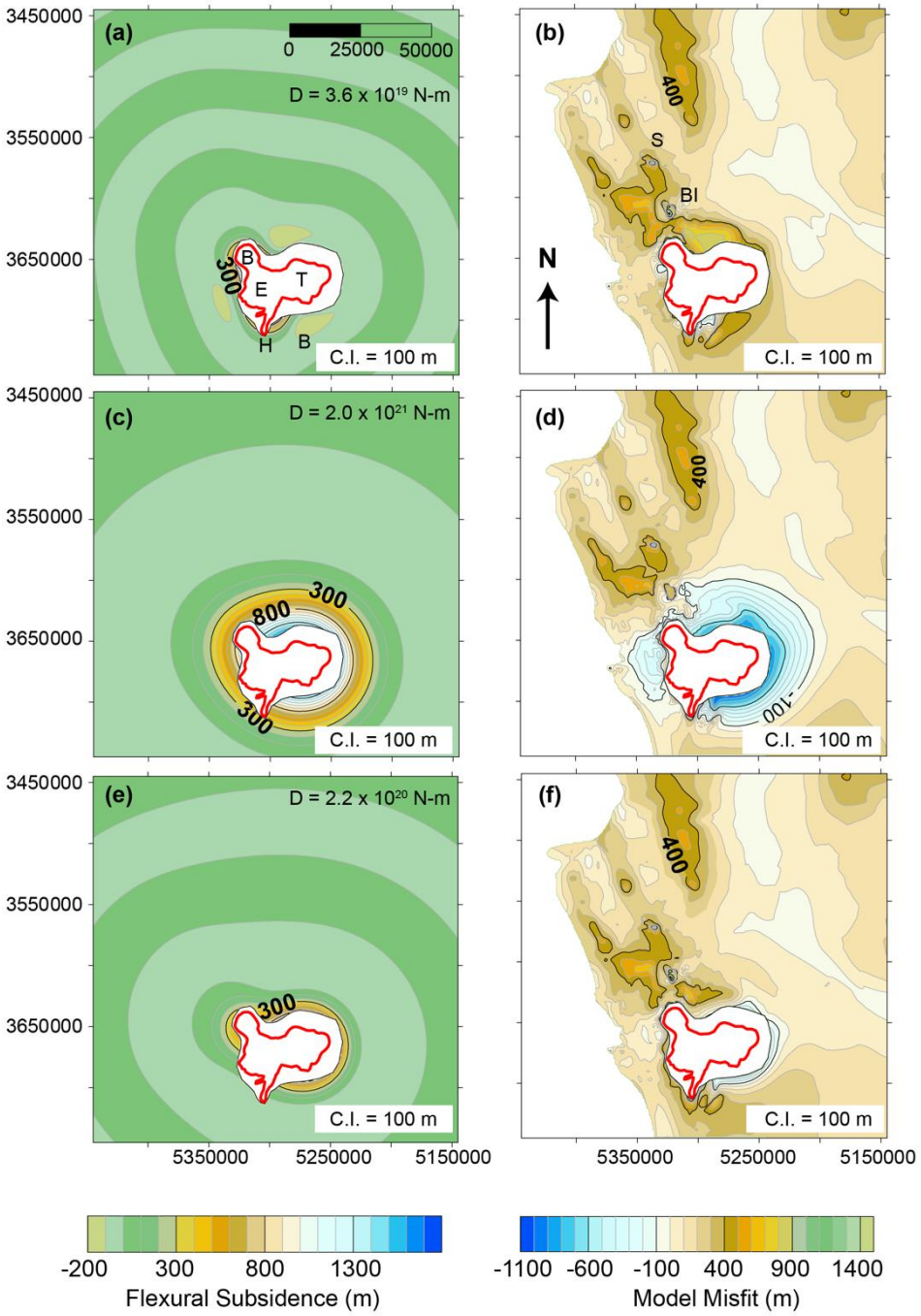

Figure 4.3. Model 1a. B – Mt. Bird; T – Mt. Terror; H – HPP; E – Mt. Erebus; BI – Beaufort Island; S – Seamount. Left: Flexural response of loads limited to Ross Island from Mt. Bird, Mt. Terror, HPP and Mt. Erebus, with a constant flexural rigidity of 3.6 x 10^{19} N-m (a), 2.0 x 10^{21} N-m (c) and 2.2 x 10^{20} N-m (e). Right: Misfit of 3-D flexure model with respect to Ri-SF isopach for corresponding models on left. White polygon around Ross Island represents the area where the data confidence is low. Hence, this area has been blanked out.

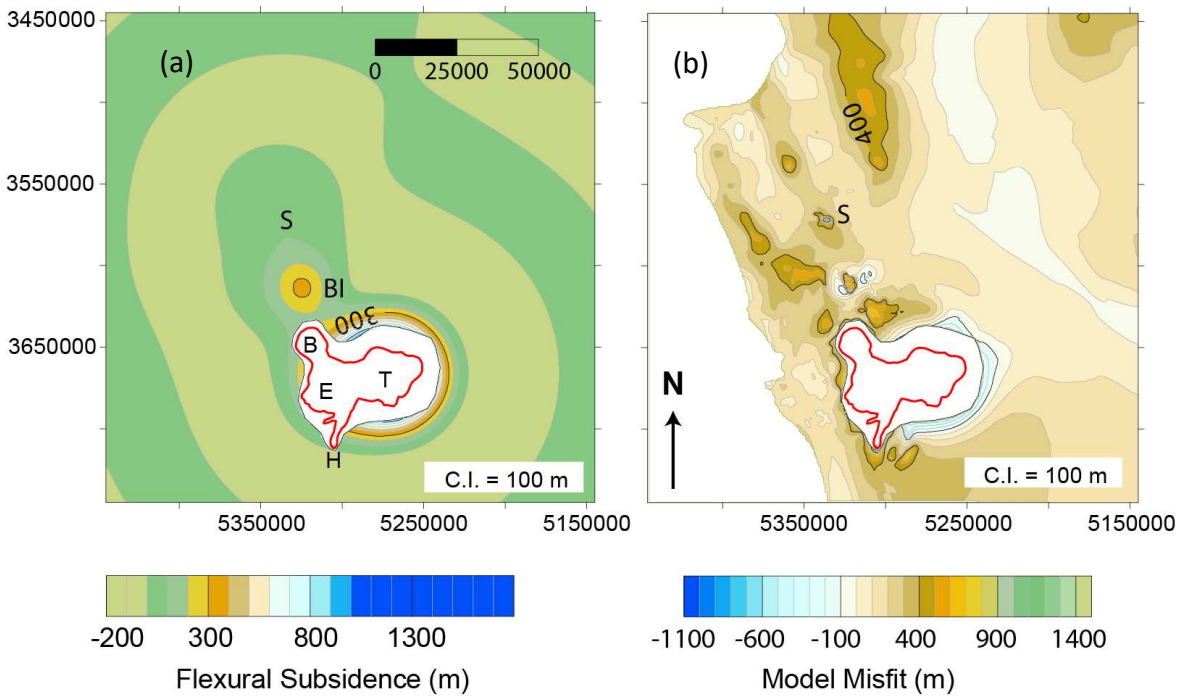

Figure 4.4. Model 1b. (a) flexural response from loading on Ross Island, at Beaufort Island and a seamount to the northwest of Beaufort Island. The best fit constant flexural rigidity for the model shown is 2.6 x 10^{20} N-m. (b) Misfit of 3-D flexure model with respect to Ri-SF isopach for corresponding models on left.

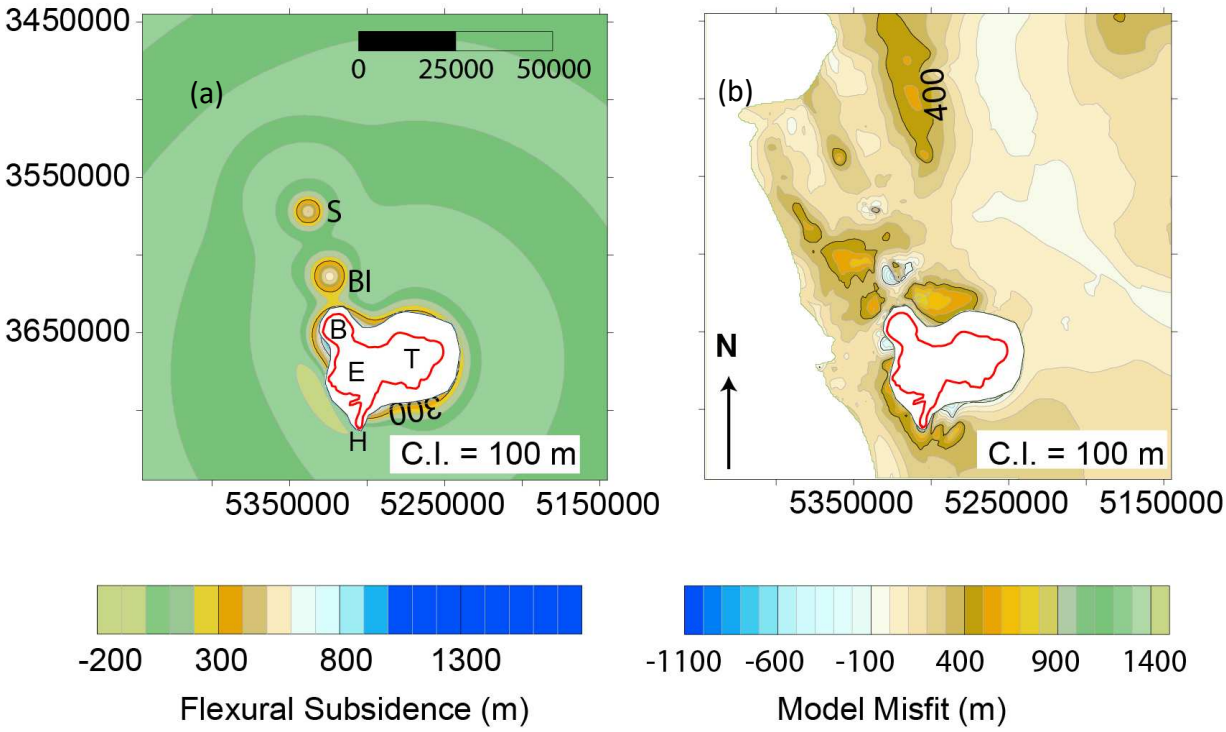

Figure 4.5. Model 2. (a) Flexural response of a variable flexural rigidity model with different D at Mt. Bird, Mt. Terror, HPP, Mt. Erebus, White Island, Beaufort Island, and seamount. (b) Misfit of flexure model with respect to Ri-SF isopach.

4.8 Tables in chapter 4

Table 4.1. Flexural rigidities, and load magnitudes of loading centers in southern VLB for models presented in this paper

Load Center	Constant D				Variable D	
	Model 1a			Model 1b	Model 2	
	D (x 10^{19} N-m)				D (x 10^{19} N-m)	Q (x 10^{15} N)
	3.6	200	22	26		
	Q (x 10^{15} N)					
Mt. Bird	18	20	1.8	1.8	3	1
Mt. Terror	88	100	56	56	22	35
HPP	9	1.8	0.88	0.88	1.2	4.5
Mt. Erebus	57	4	8.8	8.8	2.6	20
Beaufort Island	-	-	-	5	2.35	2.8
Seamount	-	-	-	0.1	0.8	1.4

Constant D models comprise of Model Classes 1a (Figure 4.3) and 1b (Figure 4.4). Variable D model is referred to as Model Class 2 (Figure 4.5) in the text.

REFERENCES IN CHAPTER 4

Aitken, A. R. A., Wilson, G. S., Jordan, T., Tinto, K., & Blakemore, H. (2012). Flexural controls on late Neogene basin evolution in southern McMurdo Sound, Antarctica. *Global and Planetary Change, 80-81*, 99-112, https://doi.org/10.1016/j.gloplacha.2012.02.004.

Armienti, P., & Perinelli, C. (2010). Cenozoic thermal evolution of lithospheric mantle in northern Victoria Land (Antarctica): Evidences from mantle xenoliths, *Tectonophysics, 486*, 28-35.

Armstrong, R.L. (1978). K-Ar dating: Late Cenozoic McMurdo Volcanic Group and dry valley glacial history, Victoria Land, Antarctica. *New Zealand Journal of Geology and Geophysics, 21(6)*, 685-698.

Bannister, S., Snieder, R. K., & Passier, M. L. (2000). Shear wave velocities under Transantarctic Mountains and Terror Rift from surface wave inversion. *Geophysical Research Letters, 27 (2),* 281-284.

Behrendt, J. C., LeMasurier, W. E., Cooper, A. K., Tessensohn, F., Tréhu, A., & Damaske, D. (1991). Geophysical Studies of the West Antarctic Rift System. *Tectonics, 10 (6)*, 1257-1273.

Brancolini, G., Cooper, A. K., & Coren, F. (1995). Seismic facies and glacial history in the Western Ross Sea (Antarctica). In A.K. Cooper, P.F. Barker, G. Brancolini (Eds.), *Geology and Seismic Stratigraphy of the Antarctic Margin, Antarctic Research Series (Vol. 68, pp. 209-233).* Washington, DC: American Geophysical Union.

Brenn, G. R., Hansen, S. E. & Park, Y. (2017). Variable thermal loading and flexural uplift along Transantarctic Mountains, Antarctica. *Geology, 45*, 463-466.

Brotchie, J. F. & Silvester, R. (1969). On crustal flexure. *Journal of Geophysical Research, 74*, 5240-5252.

Cooper, A. K., Davey, F.J., & Cochrane, G.R. (1987). Structure of extensionally rifted crust beneath the western Ross Sea and Iselin Bank, Antarctica, from sonobuoy seismic data. In A.K. Cooper & F.J. Davey (Eds.). *The Antarctic Continental Margin; Geology and Geophysics of the Western Ross Sea (pp. 93-118).* Circum-Pacific Council for Energy and Mineral Resources, Houston, TX.

Cooper, A. K., Davey, F. J., & Hinz, K. (1991). Crustal extension and origin of sedimentary basins beneath the Ross Sea and the Ross Ice Shelf, Antarctica. *Geological Evolution of Antarctica, 5*, 285-291.

Davey, F. J., Brancolini, G., Hamilton, R. J., Henrys, S. A., Sorlien, C. C., & Bartek, L. R. (2000). A revised correlation of the seismic stratigraphy at the Cape Roberts drill sites with the seismic stratigraphy of the Victoria Land Basin, Antarctica. *Terra Antarctica, 7 (3)*, 215-220.

Decesari, R. C., Sorlien, C. C., Luyendyk, B. P., Wilson, D. S., & Bartek, L.R. (2007). Regional seismic stratigraphic correlations of the Ross Sea: Implications for the tectonic history of the West Antarctic Rift System. In A. K. Cooper, et al. (Eds.), *Antarctica: A Keystone in a Changing World. Proceedings of the 10th International Symposium on Antarctic Earth Sciences.* U.S. Geological Survey and The National Academy Press, Washington, D. C., DOI:10.3133/of2007-1047.srp052.

Dunbar, G. B., Atkins, C., Magens, D., Niessen, F., & ANDRILL-SMS Science team (2009). Physical Properties of the AND-2A core, ANDRILL Southern McMurdo Sound Project, Antarctica. *Terra Antarctica, 15 (1)*, 49-56.

Esser, R.P., Kyle, P.R., & McIntosh, W.C. (2004). 40Ar/39Ar dating of the eruptive history of Mount Erebus, Antarctica: volcano evolution. *Bulletin of Volcanology, 66,* 671-686.

Fielding, C. R., Whittaker, J., Henrys, S. A., Wilson, T. J., & Naish, T. R. (2008). Seismic facies and stratigraphy of the Cenozoic succession in McMurdo Sound, Antarctica: Implications for tectonic, climatic, and glacial history. *Paleogeography, Palaeoclimatology, Palaeoecology, 260,* 8-29.

Fielding, C.R. (2018). Stratigraphic architecture of Cenozoic succession in the McMurdo Sound region, Antarctica: An archive of polar paleoenvironmental change in failed rift setting. *Sedimentology, 65*, 1-61.

Hall, J. M., Wilson, T. J. & Henrys, S. A. (2007). Structure of Central Terror Rift, Western Ross Sea, Antarctica. *In Cooper, et al. (Eds.) Antarctica: A Keystone in a Changing World - Online Proceedings of the 10th ISAES*. USGS Open-File Report 2007.

Hansen, S. E., Graw, J. H., Kenyon, L. M., Nyblade, A. A., Wiens, D. A., Aster, R. C., et al. (2014). Imaging the Antarctic mantle using adaptively parameterized P-wave tomography: Evidence for heterogeneous structure beneath West Antarctica. *Earth and Planetary Science Letters, 408,* 66-78. https://doi.org/10.1016/j.epsl.2014.09.043.

Heeszel, D.S., Wiens, D.A., Anandakrishnan, S., Aster, R.C., Dalziel, I.W.D., Huerta, A.D., et al. (2016). Upper mantle structure of central and West Antarctica from array analysis of Rayleigh wave phase velocities. *Journal of Geophysical Research Solid Earth, 121*, 1758-1775. https://doi.org/10.1002/2015JB012616

Hertz, H. (1884). On the equilibrium of floating elastic plates. *Wiedemann's Annals, 258*, 449–455. https://doi.org/10.1002/andp.18842580711.

Hole, M. J., & LeMasurier, W. E. (1994). Tectonic controls on the geochemical composition of Cenozoic alkali basalts from West Antarctica. *Contributions to Mineralogy and Petrology, 117*, 187-202.

Horgan, H., Naish, T., Bannister, S., Balfour, N., & Wilson, G. (2005). Seismic stratigraphy of the Plio-Pleistocene Ross Island flexural moat-fill: a prognosis for ANDRILL Program drilling beneath McMurdo-Ross Ice Shelf. *Global and Planetary Change, 45 (1-3)*, 83-97.

Jha, S., Harry, D. L., & Schutt, D. L. (2017). Toolbox for Analysis of Flexural Isostasy (TAFI)—A MATLAB toolbox for modeling flexural deformation of the lithosphere. *Geosphere, 13 (5),* 1555-1565. https://doi.org/10.1130/GES01421.1.

Mukasa, S. B., & Dalziel, I. W. D. (2000). Marie Byrd Land, West Antarctica: Evolution of Gondwana's Pacific margin constrained by zircon U-Pb geochronology and feldspar common-Pb isotopic compositions. *Geological Society of America Bulletin, 112 (4)*, 611- 627.

Nadai, A. (1963). *Theory of Flow and Fracture of Solids*. New York: McGraw-Hill.

Nardini I., Armienti P., Rocchi S., Dallai L. & Harrison D. (2009). Sr-Nd-Pb-He-O isotope and geochemical constraints on the genesis of Cenozoic magmas from the West Antarctic Rift. *Journal of Petrology, 50*, 1359-1375

Niessen, F., Gebhardt, A. C., Kuhn, G., Magens, D. & Monien, D. (2013). Porosity and density of the AND-1B sediment core, McMurdo Sound Region, Antarctica: Field consolidation enhanced by grounded ice. *Geosphere, 9 (3)*, 489-509. https://doi.org/ 10.1130/GES00704.1

Rocchi, S., Armienti, P., D'Orazio, M., Tonarini, S., Wijbrans, J. R., & Vincenzo, G. D. (2002). Cenozoic magmatism in the western Ross Embayment Role of mantle plume versus plate dynamics in the development of the West Antarctic Rift System. *Journal of Geophysical Research, 107 (B9)*, 2195. https://doi.org/10.1029/2001JB000515

Shen, W., Wiens, D.A., Anandakrishnan, S., Aster, R.C., Gerstoft, P., Bromirski, P.D., et al. (2018). The crust and upper mantle structure of central and West Antarctica from Bayesian inversion of Rayleigh wave and receiver functions. *Journal of Geophysical Research: Solid Earth, 123*, 7824-7849.

Tonarini, S., Rocchi, S., Armienti, P., & Innocenti, F. (1997). Constraints on timing of Ross Sea rifting inferred from Cainozoic intrusions from northern Victoria Land, Antarctica. In C. A. Ricci (Ed.), *The Antarctic Region: Geological Evolution and Processes, 511-521*, Univ. degli Studi di Siena, Siena, Italy.

Turcotte, D.L. (1979). Flexure. *Advances in Geophysics, 21*, 51-86.

Weaver, S.D., Storey, B.C., Pankhurst, R.J., Mukasa, S.B., DiVenere, V.J., & Bradshaw, J.D., (1994). Antarctica-New Zealand rifting and Marie Byrd Land lithospheric magmatism linked to ridge subduction and mantle plume activity. *Geology, 22,* 811-814,

Wenman, C. P., Harry, D. L., & Jha, S., (in review). Tectonic and Stratigraphic Evolution of the Victoria Land Basin and Ross Island Flexural Moat, West Antarctica. *Geochemistry, Geophysics, Geosystems.*

Wright, A.C., & Kyle, P.R. (1990 a). A. 15 Mount Bird. In LeMasurier, W.E. & Thompson, J.W. (Eds.), *Volcanoes of the Antarctic Plate and Southern Oceans*. American Geophysical Union, Washington D.C.

Wright, A.C., & Kyle, P.R. (1990 b), A.16 Mount Terror. In W.E. LeMasurier & J.W. Thompson, (Eds.), *Volcanoes of the Antarctic Plate and Southern Oceans*. American Geophysical Union, Washington D.C.

Wright, A.C., & Kyle, P.R. (1990 c), A. 17 Mount Erebus. In W.E. LeMasurier & J.W. Thompson, (Eds.), *Volcanoes of the Antarctic Plate and Southern Oceans*. American Geophysical Union, Washington D.C.

Wright, A.C., & Kyle, P.R. (1990 d), A. 18 Hut Point Peninsula. In W.E. LeMasurier & J.W. Thompson, (Eds.), *Volcanoes of the Antarctic Plate and Southern Oceans*. American Geophysical Union, Washington D.C.

APPENDIX A1

Supplementary file to Jha et al., 2017, Toolbox for Analysis of Flexural Isostasy (TAFI) – A MATLAB® toolbox for modeling flexural deformation of the lithosphere.

A 1.1 TAFI directory structure

TAFI is organized into the main directory, “TAFI”, which contains the files defining the GUI ("TAFI.fig" and "TAFI.m") and a README file describing TAFI’s installation and use (manuscript Figure 2.2, Table 2.2). The main TAFI directory also contains nine subdirectories. The subdirectory "GUI_Functions” contains files accessed by the GUI that define icons, the default parameter values that populate the GUI when it is opened (defined in the file GUI_Functions/Defaults/TAFI_Defaults.m), and functions needed to enable or disable GUI elements depending on the plate and load geometry combinations. The subdirectories “Geodynamic_Functions” and “Gravity_Functions” contain the functions used to calculate the flexure and gravity profiles (2-D) or fields (3-D). The “Load_Functions” subdirectory contains functions to read and re-sample the user-provided discretized load, and functions to convolve the uniformly sampled load function with the Green’s Function. The resampling and convolution functions can be called from the MATLAB command line, as well as from within TAFI’s GUI. The sub-directory “Plot_Function” contains functions to generate the flexural deformation and gravity plots located in the GUI “Plot panel”. The “Output_Parameters” sub-directory contains the TAFI functions used to find the maximum and minimum flexural deflections (w_{max} and w_b) and the locations of the crest of the peripheral uplift and zero-crossing between the flexural basin and peripheral uplift (x_b and x_o). Sample bathymetry and Free Air gravity data from the Aleutian trench that is used for the case study presented in Section 5 are included in the subdirectory

"Example_Data". A pdf help manual, which can be accessed from TAFI's GUI, is located in the subdirectory "TAFI_Manual".

A 1.2 GUI use

TAFI's GUI allows the flexure and gravity curves to be modified interactively by changing the model parameter values using TAFI's sliders and edit boxes. Parameter values entered in the edit boxes should be given in scientific notation (i.e., 1.2e+8, etc.). When edit boxes have corresponding sliders, values entered in the edit box must lie within the range of the sliders. The MATLAB tool used to create the sliders in TAFI changes the associated parameter value in discrete increments. TAFI sets the slider increment to be equal to 0.01% of the slider's range. Users can enter more precise parameter values in the edit boxes corresponding to each slider.

When TAFI is initialized, the model parameters and the ranges of the sliders are preset to default values based on existing literature that are intended to span realistic ranges for Earth models. The parameter value and range defaults can be modified from the "Change defaults – TAFI Defaults" contextual menu in the TAFI GUI or by editing the "TAFI_Defaults.m" file. The flexural rigidity of the Earth's lithosphere is estimated to range from a low of $7x10^{15}$ N-m near mid-ocean ridges to a high of $1.4x10^{25}$ N-m in continental interiors (Watts, 2001). Accordingly, the default range of the "Flexural Rigidity" slider is 10^{15} to 10^{26} N-m and the default value is $2x10^{20}$ N-m. The "Load Magnitude" slider ranges from 1 to a maximum of 10^{20} (units depend on the plate geometry chosen, and are N/m for a line load or N for a point load), with a default initial value of $5x10^{11}$N/m. The default maximum value of the loading slider is chosen to exceed the largest reasonable Earth topographic load (the Himalayan topographic load, for example, is approximately $3x10^{11}$ N/m, based on an average elevation of 5 km, average width of 2000 km, and an average density of $2.7x10^{3}$ kg/m^{3}). The default "Load Position" slider limits are -1000 km to

+1000 km (approximately 3 default model flexural wavelengths to either side of the origin), with a default value of 0 km. The “Load Magnitude” slider changes to “Load Scaling” slider with a range from 0 to 10 (with a default value of 1) when a spatially distributed load is chosen in the “Load Geometry” pulldown menu. When a spatially distributed load is chosen, the user is prompted for the location of a file containing a discretely sampled load function (the format of the file is described in in the next section). The imported load function is multiplied by the scaling factor selected from the “Load Scaling” slider or edit box before computing the modeled deflection. The “Load Wavelength” slider is active only when the “Periodic loading” option is selected from the "Load Geometry" dropdown menu, and ranges from 1 to 40,000 km (roughly the circumference of the Earth), with a default value of 1 km.

The flexure and gravity curves calculated by TAFI are plotted in the “Plot panel” on the right side of the TAFI GUI. The dimensions of the plots are specified in the "Xmin" and "Xmax" edit boxes. In the case of 3-D models, the plot dimensions are the same size as the input load grid. The user should be certain that the size of the input load grid spans the region of interest, not just the region encompassing the load. These plots are updated automatically when the model parameters are changed using the sliders, by adding new curves in 2-D plots and replacing the flexural and gravity surfaces in 3-D plots. If the parameters are changed using the edit boxes, the “Plot Flexure” and “Plot Gravity” buttons located below the "Model Parameters" panel must be used to add the new curves to the flexure and gravity plots.

The primary purpose of TAFI is to facilitate the fitting of the elastic flexural model to gravity and/or vertical displacement data provided by the user. The “Open File” and “Plot Data” buttons in the “Data Import Utility” panel allow input and plotting of gravity and vertical deformation data that can be used to constrain the flexural model. The type of data file being

imported is specified in the “Data Type” dropdown menu in the “Data Import Utility” panel. Free Air gravity should be used for marine flexural models and Bouguer gravity on land, as TAFI does not explicitly model the gravitational anomaly associated with surface topography. Constraints on vertical displacements are referred to in the TAFI “Data Type” menu as flexure constraints. Examples of flexure constraints include subsidence data from wells (generally in the form of horizon depth or isopach thicknesses), depth or isopach data digitized from maps, cross-sections, or seismic data, and bathymetry. Once the gravity and/or flexure constraints are loaded, the “Plot Data” button at the bottom of the “Data Import Utility” is selected to plot the constraining data. Changes in the model parameters, made either through the sliders or text boxes in the “Model Parameter” panel, produce changes in the modeled flexural and gravity curves that can be directly compared to the data in the graphs shown in the “Plot panel”. The flexural and gravity data can be shifted vertically or horizontally to better match the modeled curves using the edit box and X, Y or Z buttons in the “Data Shift” panel. This panel appears when the “Plot Data” button is selected.

The push buttons located below the “Model Parameters” panel control the plots shown in the “Plot panel”. As noted previously, the “Plot Flexure” and “Plot Gravity” buttons are needed to update the flexural and gravity curves when the text boxes, rather than sliders, are used to change the model parameters. “Clear All Curves” removes the flexural and gravity curves from the plot area, leaving only the imported data plotted. “Clear All Data” removes the imported data points from the plot, leaving only the modeled curves. “Clear All Data” also erases the constraining data from the data table. “Reset All Plots” clears all curves and data from the Plot panels. After “Reset All Plots” is selected, the curves for the most recent flexural and gravity model can be refreshed using the “Plot Flexure” and “Plot Gravity” buttons.

A 1.3 Input files

The input files containing the flexure and gravity constraints and load functions can be in either text or Excel format. The flexure and gravity constraints are read when the appropriate file type is selected from the dropdown menu in the "Data Import Utility" panel. The flexure and gravity data files for 2-D models should be formatted in two columns, the first providing the position (in km) of the data point relative to an origin chosen by the user, and the second column providing either the vertical deflection (in km) or gravity value (in mGal). In case of a 3-D model, the flexure and gravity data files have to be formatted in three columns, the first two columns providing the position (X and Y, in km) of the data point relative to an origin and third column providing the vertical deflection (in km) or gravity (in mGal). The file containing the discretized load function is accessed through the "Import 2-D Distributed Load", "Import Distributed Axisymmetric Load" or "Import 3-D Distributed Load" option in the "Load Geometry" menu. This opens a pop-up window prompting the user for the load file location. The load file for a 2-D or axisymmetric distributed load has the same format as the 2-D flexure and gravity constraint files, with the first column specifying the position (in km) and the second column specifying the magnitude of load at the sample points (in N/m^2). The sample positions in the load file should be relative to the same coordinate origin as in the flexural and gravity constraint files (although, as noted previously, the positions of all of these can be adjusted with sliders and edit boxes in the TAFI GUI). In the case of a 3-D load, the load file is formatted in one column. The first two rows provide the discretization interval (in km) in the load grid's X (grid row) and Y (grid column) directions. The next two rows of the load file specify the number of nodes in the X and Y directions. The remaining rows specify the load magnitude (in N/m^2) at each grid node. Load values are given

sequentially for each grid column (Y coordinates) in the first grid row (first X coordinate), and the sequence repeated for all grid rows.

A 1.4 Saving the TAFI model

The deflection and gravity profiles and surfaces can be saved as ASCII text files by selecting "Export Flexure" or "Export Gravity" from the "File-Export" menu at the top of the TAFI window. The exported files are saved in the same format as the load input files, described previously. The model parameters (flexural rigidity, elastic thickness, load position and magnitude/scaling, discretization interval, etc.) and key output parameters (manuscript Table 2.1) can be exported into text files using the "Export Parameter-Export Inputs" or, "Export Parameter–Export Outputs" options in the "File" menu. The flexure and gravity plots can be saved by using the MATLAB Figure Palette tool from the "Edit Figures-Edit Flexure" or "Edit Figures-Edit Gravity" options in TAFI's "File" menu. The figure palette can also be used to edit plot properties such as line thicknesses, and data point size, colors, text labels, etc.

APPENDIX A2
Decompaction formula derivation

Decompaction for:

1) Linear porosity (ϕ_z)
2) No cementation (compaction only)
3) Not interested in burial history – just the starting (uncompacted) bed thickness

Definitions and conditions:

T_u = uncompacted bed thickness (bed thickness when deposited with top of the bed at seafloor and bottom of bed at depth z=Tu).

T_c = compacted bed thickness (measured from isopachs).

ρ_g, ρ_g = density of sediment grains and water, respectively.

φ_u, φ_c = porosity at mid-depth of bed before (uncompacted) and after (compacted) burial to modern depth.

The porosity at depth "z" is obtained from the following equation:

$$\emptyset = \emptyset_0 - mz; \qquad z = 0\ at\ seafloor, +down \tag{A 2.1}$$

Conservation of solid volume requires:

$$\int_0^{T_u}(1-\emptyset_u)\,dz = \int_0^{T_c}(1-\emptyset_c)\,dz \tag{A 2.2}$$

Solving Equation A2.1, we get the familiar solution (Watts, 2001):

$$T_u = \frac{1-\emptyset_c}{1-\emptyset_u}T_c \tag{A 2.3}$$

The porosity at the mid-depth of the uncompacted bed is unknown because to know that we would need to know the mid-depth (and hence thickness) of the uncompacted bed. We could then use Equation A 2.1. But we don't know the mid-depth.

Going back to integrals, the left side of Equation A 2.2 is given as (using Equation A 2.1):

$$\int_0^{T_u}(1-\emptyset_0+mz)dz = T_u(1-\emptyset_0)+\frac{mT_u^2}{2} \quad \text{(A 2.4)}$$

So, using the solution to the integral on the right side, we have:

$$T_u(1-\emptyset_0)+\frac{mT_u^2}{2} = (1-\emptyset_c)T_c \quad \text{(A 2.5)}$$

Rearranging Equation A 2.5:

$$\frac{mT_u^2}{2}+T_u(1-\emptyset_0)-(1-\emptyset_c)T_c = 0 \quad \text{(A 2.6)}$$

The roots of the above equation are:

$$T_u = \frac{1}{m}\left[(\emptyset_0-1) \pm \sqrt{(1-\emptyset_0)^2+2m((1-\emptyset_c)T_c}\right] \quad \text{(A 2.7)}$$

Testing this equation against several values of the slope, porosities and compacted thicknesses, suggested that first root solution of Equation A 2.7 gives a reasonable uncompacted thickness of a layer.